A MULTIFUNCTIONAL APPROACH TO DEVELOPMENT, FABRICATION, AND CHARACTERIZATION OF Fe_3O_4 COMPOSITES

A Dissertation
Presented to
The Academic Faculty

by

Silvia Liong

In Partial Fulfillment
of the Requirements for the Degree
Doctor of Philosophy in the
School of Materials Science and Engineering

Georgia Institute of Technology
December 2005

A MULTIFUNCTIONAL APPROACH TO DEVELOPMENT, FABRICATION, AND CHARACTERIZATION OF Fe_3O_4 COMPOSITES

Approved by:

Dr. William S. Rees, Jr., Advisor
School of Materials Science and Engineering and School of Chemistry and Biochemistry
Georgia Institute of Technology

Dr. John D. Muzzy
School of Chemical and Biomolecular Engineering
Georgia Institute of Technology

Dr. Meilin Liu
School of Materials Science and Engineering
Georgia Institute of Technology

Dr. Rick L. Moore
Signatures Technology Laboratory
Georgia Tech Research Institute

Dr. David L. McDowell
School of Materials Science and Engineering and School of Mechanical Engineering
Georgia Institute of Technology

Date Approved: October 31, 2005

For Akong and Ama

ACKNOWLEDGEMENTS

I would like to thank my advisor, Professor Will Rees, for his support and his encouragement. He has always challenged me to become a better scientist and the experience has been rewarding. I would like to thank the committee members, Professor Meilin Liu, Professor David McDowell, Dr. Rick Moore, and Professor John Muzzy for their time and suggestions. I want to especially thank Dr. Moore for his continuous encouragement and guidance during this project. I truly appreciate his expansive knowledge of magnetic materials and his willingness to help me with this project.

I would like to thank past and present Rees group members, namely Qian Luo, Javier Concepcion, Xi Zeng, Oliver Just, Ebony Mays, Shalini Kandoor, and Jack Eichler. I am grateful to Joelle Szendel, whose organizational skills and friendship has always kept me in check.

The STL group in Georgia Tech Research Institute has been like a second group to me. I would like to thank Dr. Alexa Harter who provided me with the initial sample of magnetite nanoparticles (courtesy of Professor Y.K. Hong from University of Idaho) and encouraged me to investigate synthesis methods of magnetic nanoparticles. I want to thank Dr. John Schultz for his advice and his help with the permeameter measurements. I also want to thank David Maybury for his help with low impedance measurements.

The faculty and staff of the Materials Science and Engineering and Chemistry departments have been extremely helpful. I am grateful for the opportunity to learn from the faculty members and for their support, namely Professor Tom Sanders and Professor Rina Tannenbaum. I want to thank Susan Bowman for her advice and guidance. Richard

Shafer provided me with access to a VSM, which was essential in the characterization of magnetite nanoparticles. Dr. Kyoung-Sik Moon helped tremendously with the mechanical properties measurements.

I am grateful for the lifelong friends that I have made in graduate school. I want to thank Melissa Zubris, Curtis Neff, Raymond Oh, Jeffrey King, Benjamin Church, Tammy McCoy, and Zhuqing Zhang for their friendships.

The completion of this dissertation is a tribute to my family who never let me forget the importance of education. Through the years, my grandparents, parents, aunts, and uncles have always given me their unconditional love and support. I would like to especially thank my parents for their hard work and the sacrifices they have made so that my brother and I can have boundless opportunities in this country. Lastly, I would like to thank my husband for being my best friend and for his unwavering support.

TABLE OF CONTENTS

LIST OF TABLES

LIST OF FIGURES

SUMMARY

The development of multifunctional materials has gained a great deal of attention in recent years because they provide a way to reduce parasitic weight in vehicles, which reduces both fuel consumption and operational cost. Composite systems are used in the development of materials with multifunctional properties.

This project fabricated and characterized the electromagnetic and mechanical properties of particulate composite systems. The goal was to improve both sets of properties using Fe_3O_4 (magnetite) as the filler in a polymer matrix. Two particulate composite systems were studied. The first system used Fe_3O_4 nanoparticles of average diameter 7 nm, 12 nm, and 25 nm as fillers. In the second sytem, 5 micron polypyrrole-coated Fe_3O_4 particles were the fillers. Polypyrrole, a conductive polymer, was added as a way to incorporate electrical conductivity into the composite.

Since Fe_3O_4 nanoparticles with diameters smaller than 20 nm were not readily available, part of this project was devoted to the synthesis and characterization of magnetite nanoparticles using chemical coprecipitation. Process variables were found to have a strong effect on particle size, and they included the concentration of iron precursor, the ionic strength of solution, and the ratio of ferric to ferrous ions. Magnetite nanoparticles with average diameters of 5 to 12 nm were synthesized and they exhibited superparamagnetic behavior. Characterization of the particles' magnetic properties was conducted and showed a correlation with particle size. Magnetization of the particles decreased with their size; it was attributed to the presence of a magnetically dead layer on the surface. The thickness of the dead layer was calculated to be 0.94 nm, very close to the lattice constant of Fe_3O_4.

Analysis of the nanocomposites showed that both electromagnetic and mechanical properties are a function of filler size. The properties of nanocomposites were also compared with those of micron-sized composites. Magnetic nanoparticles exhibited reduced magnetization with decreasing particle size; therefore, the same trend was observed with the magnetic permeability of nanocomposites. Resonance frequencies of micron-sized composites were close to 25 nm composites, approximately 4 to 5 GHz. In contrast, 12 nm fillers displayed resonance at approximately 2.5 GHz. The mechanical properties of 25 nm composites also behaved similarly to micron-sized composites. 7 nm and 12 nm fillers showed improvements in fracture toughness, but at the expense of decreased modulus and strength.

In the second composite system, polypyrrole coating on Fe_3O_4 fillers offered advantages to both the mechanical and electromagnetic properties. Surface conductivity of Fe_3O_4 particles was improved by two orders of magnitude after they were coated with polypyrrole. The same effect translated to composites: at a volume fraction of 0.10, the composite with uncoated Fe_3O_4 fillers had a conductivity less than $1x10^{-9}$ S/cm; using polypyrrole coated fillers, the conductivity was ~1×10^{-6} S/cm. The fabricated samples were below the percolation threshold so it can be expected that conductivity improvements were minimal. Nevertheless, this method allowed for concurrent optimization of both magnetic and conductive properties. The flexural strength of composite with polypyrrole coating was also higher than the uncoated fillers at volume fraction of 0.10, and the modulus was comparable.

A multifunctional approach was used to develop, fabricate, and characterize two particulate composite systems. Two types of fillers were evaluated. Fe_3O_4 nanoparticles

improved fracture toughness, but they compromised other properties. Polypyrrole-coated Fe_3O_4 has more potential for multifunctional material applications because the coating allows for concurrent increase in magnetic permeability and electrical conductivity in a composite. The polypyrrole coating also improved the strength of the composite. Composites with a higher volume fraction of polypyrrole-coated fillers should be able to display these benefits more effectively. Polypyrrole-coating process is versatile enough to be applied to other materials.

CHAPTER 1

INTRODUCTION

The intent of this thesis is to lay groundwork for the development, fabrication, and characterization of lightweight multifunctional materials. This was accomplished by developing polymer-based composites and using fillers with multiple functionalities.

1.1 Composite Materials

Countless types of composites with wide variations of properties have been developed throughout engineering history but they all have similar challenges. The general goal in the design and fabrication of all composites has been to combine two or more different materials (or phases) to produce a single material that behaves as a homogenous entity and has predictable and reproducible properties. The composite material often has properties that are different from the individual components [1, 2]. With appropriate design, a composite combines the best qualities of each component, producing a material with properties that are superior to each component. The selection of the constituent materials is nontrivial. This research emphasizes two and three component composites. Examples include polymer-metal, polymer-ceramic, metal-ceramic, and polymer-metal-ceramic components, or mixtures of the same class of materials with distinct phases [1].

Common composite materials are light and have superior mechanical properties. Fiber-reinforced plastics and particulate-filled composites are two common examples of mechanical composites. There are two components in such composites: polymer-based

matrix and reinforcing fillers (fibers or particles) [1, 3]. The fibers provide strength and stiffness to the composite, while the polymer matrix acts as lightweight binder and distributes external load to the fibers [2]. In addition to increasing the rigidity of the polymer matrix, the particles are added to modify rheology to aid in processing [4, 5].

The history of composite materials spans several thousand years. Man-made composites can be traced to 5000 B.C. in the Middle East, where pitch was used as a binder for reeds to make boats [6]. This concept migrated from the Middle East to the Celts in Wales. Evidence of laminated woods dating to 1500 B.C. was found on the island of Thebes, Greece. Mongolian bows, which consisted of wood, animal tendon, and silk laminates are examples of composites with multi-components. Laminated woods using shellac resin have been used in India for at least 3000 years [2].

The use of nanotechnology in composites is also found in history. Roman architects and engineers were able to construct impressive buildings using limestone, gravel, and pozzolan, which is the naturally occurring version of fly ash [7]. This concrete formulation was the building block of bridges, coliseums, and aquaducts [7, 8]. The Roman concrete would "set" under water and thereby facilitated construction of wharves and docks. Nanoparticles provided color to glasses used in elaborate stemware and intricate stained glasses [9]. By incorporating metal nanoparticles in glass, light was absorbed but not scattered. The optical properties of these composites are a function of the particle size, thereby producing glasses of various colors. Some of the earliest evidences of this application are the formulations left by A. Cassius and A. Libavius from the 16^{th} century. Unbeknownst to them and the Romans, they were fabricating nanocomposites.

Mechanical composite materials continue to be an integral part of our daily lives. Composites have a wide range of applications, from sports equipment to transportation vehicles. Composites make it possible for tennis rackets, kayaks, boats, and many other recreational sports equipment to be both lightweight and strong [1, 2]. They are found in aircraft components, ranging from the seat frames to sections of the wings [10, 11]. The rotor blades of helicopters are made of composite because they have much greater tolerance for fatigue than metals . Automobile tires are made of rubber reinforced with steel thread to extend life and to increase performance at high speeds.

Historic and more contemporary examples of composite materials appear to favor mechanical properties for applications. However with the application of electrical, thermal, magnetic, and optical properties in our everyday lives, nonmechanical composites have also become important [12]. These materials are not as apparent to the everyday user since they may be encased in protective packaging, but they provide essential functions in many systems, such as personal computers. Several examples of composite materials with nonmechanical (transport) properties are listed in Table 1-1.

Table 1-1. Examples of composites with transport properties [12].

	Composites	Applications
Electronic composites	Carbon black/graphite/polybutadiene rubber LiI or AgI matrix dispersed with Al_2O_3 Metallic particles dispersed in paint	Chemical sensors Solid electrolyte for batteries Electromagnetic suppressors
Magnetic composites	P-Magnets (elastomer and magnetic particles)	Motor and actuator devices Magnetic memory
Thermal composites	Carbon black or V_2O_3 and polymer (e.g. epoxy) Clay (silicate), $Al_2O_3 \cdot 3H_2O$, or Na_2CO_3 and polymer	NTC and PTC thermistors Flame retardant material
Optical composites	J-sheet (polyvinyl alcohol and iodine ink) Nanoparticles dispersed in passive medium (e.g. polymer, mesoporous structure)	Polarizers Optoelectronics Optical fibers
Cross-coupled composites	Polymer matrix and piezoelectric powder	Transducers Hydrophones

There are three main challenges for successful fabrication of a composite. One challenge is to understand the amount of each constituent that is required to achieve a composite with the targeted properties. To meet that goal, models are derived from first principles and/or empirical data and are invoked to establish a relationship between filler volume fraction and the desired composite property. A well-characterized composite system will have a guideline such as that shown in Figure 1-2, where the properties of the composite, $P_{c,1}$ and $P_{c,2}$, are mapped out with the volume fraction of the matrix and filler, V_m and V_f, respectively. The second challenge involves fabrication and formulation, where the engineer must resolve bonding or wetting incompatibilities

between the surface of filler and matrix. This interface can be weak points and cause undesirable effects such as in the case of mechanical failure [3]. Additives such as stearic acids and coupling agents may be incorporated during formulation to improve dispersion of filler in a matrix and adhesion between matrix and filler, respectively [3]. The interfacial areas of different constituents plays an increasingly significant role as the size of the fillers approach the nanoscale [13, 14]. The third technical challenge is the development of a process that refines fabrication of the composite to achieve minimal defects. Defects such as voids and large agglomerates of fillers can negatively impact the mechanical and nonmechanical properties of the composites [13, 15]. Therefore, it is imperative that a process can fabricate composites with optimal microstructure.

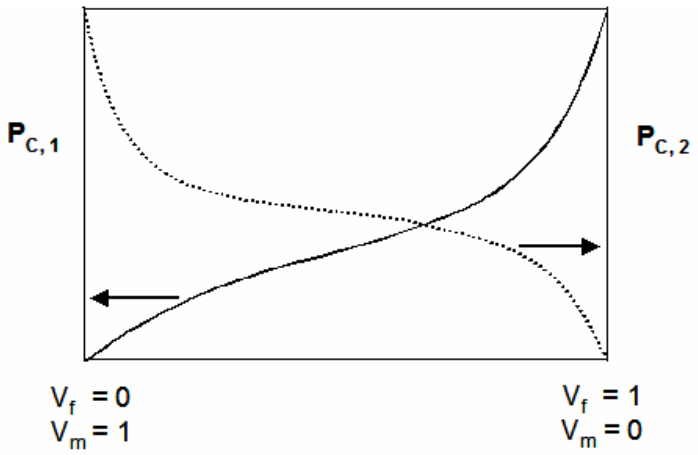

Figure 1-1. Schematic of relationship between composite properties, $P_{C,1}$ and $P_{C,2}$, with filler volume fraction, V_f.

1.2 Multifunctional Materials

The emerging fields of nanotechnology and nanoengineering provide a path to design and fabricate multifunctional composite materials. In most cases, the properties of a composite are optimized for a single property that is either structural or transport in nature, but not a combination of the two.

The discovery of carbon nanotubes by Iijima and coworkers [16] has influenced how material scientists think when developing composite materials. The modulus of carbon nanotubes was measured to be 1.25 TPa [17] and its strength is approximately 30 GPa [18], making them one of the strongest materials ever measured. Carbon nanotubes have large transport properties with electrical resistivity up to $1x10^{-4}$ Ω·cm [18] (comparable to 304 stainless steel with resistivity of $7.1x10^{-5}$ Ω·cm [19]) and thermal conductivity of 2000 W/mK is far superior to that of copper (400 W/mK) [18]. Using carbon nanotubes, material scientists can design a composite with a single filler material that reinforces the mechanical properties of the matrix and also is the source of transport properties. Table 1-2 was reproduced from Maruyama and Alam [18], and it gives a depiction of the potential of carbon nanotubes as the key component in multifunctional materials.

Table 1-2. Multifunctional applications of carbon nanotubes and nanofibers, reproduced from Maruyama and Alam [18].

			Mechanical			Electrical			Thermal		Thermo-Mechanical	
		Application System	Strength / Stiffness	Specific Strength	Through - thickness strength	Static Dissipation	Surface Conduction	EMI Shielding	Service Temperature	Conduction/ Dissipation	Dimensional Stability	CTE Reduction
Low Filler Vol. Fraction	Elastomers	Tires	•			•				•		
	Thermoplastics	Chip Package				•				•		
		Electronics/ Housing	•					•	•	•		
	Thermosets	Epoxy Products	•	•	•		•				•	•
		Composites			•						•	
High Filler Vol. Fraction	Structural Composites	Space / Aircraft Components		•	•							
	High Conduction Composites	Radiators	•							•	•	
		Heat Exchangers	•						•	•		•
		EMI Shield	•					•				

Multifunctional materials can be categorized into three different morphologies, represented schematically in Figure 1-2 [20]. In Type I, the distinct phases are mounted, coated, or laminated on top of another. The heterogeneity is most obvious in this construction since the scale of the components is large. In Type II, the phases are more integrated but the phases are still distinct. The goal is to achieve a multifunctional material of Type III, where the phases and functions are integrated from the molecular level and they are not distinct at the bulk level. Composites that consist of a matrix and reinforcing filler (e.g. fibers, fabrics, or particles) would be categorized under Type II.

Nanocomposites, such as those using carbon nanotubes as fillers, fall between Type II and Type III. Although they are composed of a separate matrix and filler, as in Type II materials, the fillers are small enough that heterogeneity is dependent on the length scale sensitivity of a characterization method. In some characterization methods, nanocomposites are viewed as a homogeneous material that is desired for Type III.

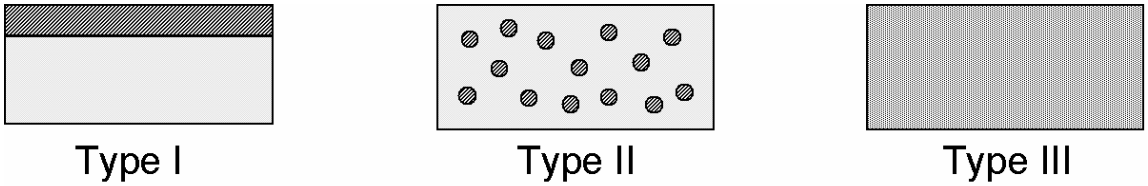

Figure 1-2. Cross section of the three types of multifunctional materials, reproduced from Momoda [20].

The development of multifunctional materials is also motivated by a need to reduce parasitic weight of a material system. This is especially important in aircraft and aerospace applications where weight reduction can have a huge impact in operational cost [11]. As an example, a simplistic view for making an aerospace vehicle invisible to radar is to apply a layer of paint over the outside of the body [21]. The additional layer of material on the plane causes the total weight of the plane to increase, and this results in increased fuel consumption and the requirement for a larger engine. Consider the effect of weight on fuel consumption for a DC-18. That plane would save 2900 liters of fuel per year for every kilogram of weight that is reduced [11]. Therefore, our invisible airplane might benefit from a structural material that can inherently shield itself from electromagnetic waves and eliminate that extra layer of paint. If the functionalities

could be integrated on a molecular level (Type III multifunctional material), problems due to incompatibility between phases (e.g. adhesion) may be circumvented altogether.

Efforts to integrate multifunctional materials into systems have been advanced by Christodolou and coworkers of the Defense Advanced Research Projects Agency (DARPA) [22]. One of the projects within this comprehensive program is to use carbon nanotubes as actuators and supercapacitors that can be woven into fabric [22]. Another material system that has already demonstrated some success is to integrate structural properties into the battery of an unmanned air vehicle (UAV) [20, 23]. The multifunctional battery would be considered a Type I, but even at this level of integration and using existing battery technology, the weight of the UAV was reduced and its flight time was increased by 10% [23], which is a significant improvement. In summary, the benefits of integrating different functions within a single material are just beginning to be realized.

1.3 Scope of Research and Objectives

The paradigm of multifunctional material was adopted here to develop a lightweight multifunctional material (LMM) with specified mechanical, electrical, and magnetic properties. Particulate-filled polymer composites are the subject of this study. Magnetite (Fe_3O_4) particles were used as the reinforcing phase embedded inside the polymer matrix, e.g. epoxy resin. Among iron oxides, magnetite is unique because it has the highest saturation magnetization (92-100 emu/g) [24] and an unusually low bulk resistivity (1.068×10^{-2} Ω·cm) [25]. Magnetite has the potential to provide the desired magnetic, electrical, and mechanical properties to the final composite. It is expected that

the reinforcing effect of nano-sized fillers will be noticeable at lower volume fractions than their micron-sized counterparts [13] . Several publications have reported that the electrical and magnetic properties of nanoparticles are dependent on their size [26-30]. This size dependence can be leveraged to adjust the electrical, magnetic, and mechanical properties of the composite without changing the filler content and/or type. There is great potential in using magnetite (nano)particles as fillers in a composite – not only from the multifunctional aspect but also from the ability to adjust the magnetic, electrical, and mechanical properties of a composite by changing the filler size. Filler content modification further expands the design space.

Coating Fe_3O_4 and other inorganic particles with a conductive polymer, such as polypyrrole (PPy), has been reported in literature [31-35]. Magnetite is relatively stable in atmospheric conditions, but the surface of the particles is susceptible to oxidation. This process forms maghemite (γ-Fe_2O_3), which has a higher resistivity than magnetite [24]. Conductive polymers are not known for their mechanical properties, so they are often supported on a substrate, e.g. particles [36]. With this method, conductivity of the composite may be increased without having to change the volume fraction of Fe_3O_4 fillers and consequently the weight penalty will be minimal. It is also a way to decouple magnetic and electrical properties and allows for a wider range and flexibility in controlling those properties.

We have discussed using three components to fabricate a multifunctional material and different means of controlling the properties of composites. Epoxy resin was used as the matrix material, Fe_3O_4 particles and polypyrrole as the fillers. Table 1-3 lists how each component contributes to the multifunctionality of the final composite

and its attributes. Figure 1-3 illustrates the cross section of the two composite systems that were investigated in this work: 1) nanocomposites with mechanical and magnetic properties and 2) composite with mechanical, magnetic, and conductive properties. For each composite system, the mechanical and transport properties were characterized at different filler levels. Most work on composites usually concentrates on either mechanical or transport properties, but the study here evaluated both sets.

Table 1-3. List of components in the proposed multifunctional composites and their contributing properties.

	Mechanical	**Magnetic Permeability**	**Electrical and Thermal conductivity**	**Attributes**
Polymer matrix	•			Lightweight
Fe_3O_4 filler	•	•	•	High M_s and low resistivity M_s = f (nanoparticle size)
PPy coating			•	Lightweight σ = f (coating thickness, dopant) Environmentally stable

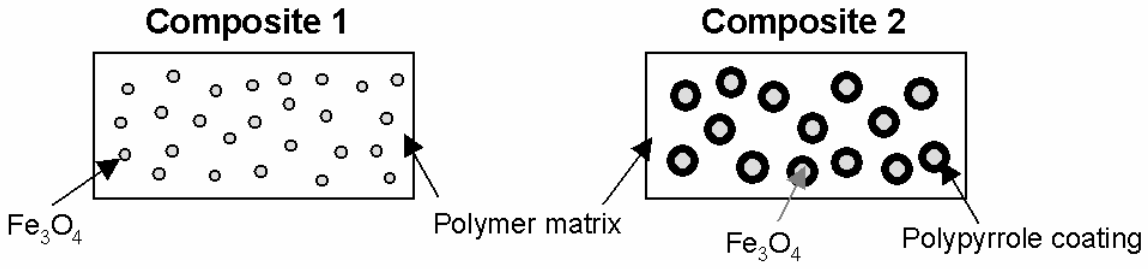

Figure 1-3. Proposed multifunctional composites.

Micron- and nanoscale Fe_3O_4 particles were used as fillers in Composite 1. In this system, the magnetic property was contributed by the Fe_3O_4 particles and the mechanical property was provided by the polymer matrix and was further reinforced by the particles. The first objective was to fabricate composite samples at different particle loadings and using particles of different sizes (5 μm, 25 nm, 12 nm, and 7 nm). Nanoparticles have a tendency to agglomerate together, so a secondary objective was to stabilize the surface of the nanoparticles using a surfactant and to maximize their dispersion in epoxy. The magnetic and mechanical properties of the composites were measured and then the effects of filler level and size on the properties were evaluated.

In Composite 2, micron-sized Fe_3O_4 particles were the filler that provides both mechanical and magnetic properties. Polypyrrole coating on the particles tuned the surface conductivity of Fe_3O_4 particles. The first objective was to coat Fe_3O_4 particles with polypyrrole making them both magnetic and conductive. The next objective was to fabricate composite samples using Fe_3O_4/PPy as fillers at different volume fractions and then measure their mechanical and transport properties as described for Composite 1.

In summary, this research work explored different means of controlling the properties of a multifunctional composite. One way was to take advantage of the property differences between micron- and nano-sized materials. Another way was to augment the properties of the fillers with a coating, allowing for increased functionality but without the weight increase that is normally associated with additional fillers. The study of these two composite systems may lead to further development of multifunctional (nano)composites for applications that require some combination of magnetic, conductive, and mechanical properties. Some of these applications include

electromagnetic interference (EMI) shields [37], radio frequency (RF) isolating material and possibly a medium for targeted drug delivery [38].

1.4 Overview of Upcoming Chapters

Before presenting the results and analysis of the experimental data, a background on magnetite and superparamagnetism will be presented in Chapter 2. Fe_3O_4 nanoparticles with diameter less than 20 nm are not readily available, and therefore they must be synthesized in-house, thus Chapter 3 will present the results of the method used to synthesis and characterize magnetite nanoparticles. A discussion on the relationship between particle size and magnetic properties will be included in that section. In Chapter 4, the fabrication of nanocomposites using the particles synthesized in Chapter 3 will be discussed, as will their characteristics. The properties of nanocomposites with average filler sizes of 25 nm, 12 nm, and 7 nm were measured and compared with composites reinforced with micron-sized fillers. Fabrication and characterization of composites with magnetic, conductive, and mechanical properties will be reported in Chapter 5. A portion of this chapter will cover the process for coating Fe_3O_4 particles with polypyrrole. In Chapter 6, the results of the research work will be summarized and recommendations for future work will be presented.

1.5 References

[1] A. Kelly, "An Introduction to Composite Materials," in *A Concise Encyclopedia of Composite Materials*, A. Kelly, Ed. Oxford: Elsevier, 1994, pp. xvii-xxix.

[2] F. P. Gerstle, Jr., "Composites," in *Encyclopedia of Polymer Science and Technology*, vol. 3, J. I. Kroschwitz, H. F. Mark, N. M. Bikales, C. G. Overberger, and G. Menges, Eds. New York: John Wiley and Sons, 1985.

[3] R. N. Rothon and M. Hancock, "General Principles Guiding Selection and Use of Particulate Materials," in *Particulate-Filled Polymer Composites*, R. N. Rothon, Ed. Essex: Longman Scientific and Technical, 1995, pp. 1-45.

[4] G. V. Jackson and M. L. Orton, "Filled Thermosets," in *Particulate-Filled Polymer Composites*, R. N. Rothon, Ed. Essex: Longman Scientific and Technical, 1995, pp. 317-370.

[5] H. S. Katz, "Particulate Fillers," in *Handbook of Composites*, S. T. Peters, Ed., Second ed. London: Chapman Hall, 1998, pp. 242-253.

[6] R. P. Sheldon, *Composite Polymeric Materials*. London: Applied Science Publishers, 1982.

[7] B. Herring and S. Miller, "The Secrets of Roman Concrete," *Constructor*, vol. September 2002, pp. 13-16, 2002.

[8] T. Kuennen, "Small Science Will Bring Big Changes to Roads," *Road Science*, vol. July 2004, pp. 20-30, 2004.

[9] W. Caseri, "Nanocomposites of Polymers and Metals or Semiconductors: Historical Background and Optical Properties," *Macromolecular Rapid Communications*, vol. 21, pp. 705-722, 2000.

[10] D. H. Bowen, "Application of Composites: An Overview," in *A Concise Encyclopedia of Composite Materials*, A. Kelly, Ed. Oxford: Elsevier, 1994, pp. 7-15.

[11] R. F. Haresceugh, "Aircraft and Aerospace Applications of Composites," in *Concise Encyclopedia of Composite Materials*, A. Kelly, Ed. Oxford: Elsevier, 1994, pp. 1-7.

[12] R. E. Newnham and J. R. Giniewicz, "Nonmechanical Properties of Composites," in *Comprehensive Composite Materials*, vol. 1, A. Kelly and C. Zweben, Eds. Amsterdam: Elsevier, 2000, pp. 431-463.

[13] C.-M. Chan, J. Wu, J.-X. Li, and Y.-K. Cheung, "Polypropylene/Calcium Carbonate Nanocomposites," *Polymer*, vol. 43, pp. 2981-2992, 2002.

[14] B. J. Ash, R. W. Siegel, and L. S. Schadler, "Mechanical Behavior of Alumina/Poly(methyl methacrylate) Nanocomposites," *Macromolecules*, vol. 37, pp. 1358-1369, 2004.

[15] M. Z. Rong, M. Q. Zhang, Y. X. Zheng, H. M. Zeng, and K. Friedrich, "Improvement of Tensile Properties of Nano-SiO2/PP Composites in Relation to Percolation Mechanism," *Polymer*, vol. 42, pp. 3301-3304, 2001.

[16] S. Iijima, "Carbon Nanotubes: Past, Present, and Future," *Physica B*, vol. 323, pp. 1-5, 2002.

[17] J.-P. Salvetat-Delmotte and A. Rubio, "Mechanical Properties of Carbon Nanotubes: a Fiber Digest for Beginners," *Carbon*, vol. 40, pp. 1729-1734, 2002.

[18] B. Maruyama and K. Alam, "Carbon Nanotubes and Nanofibers in Composite Materials," *SAMPE Journal*, vol. 38, pp. 59-70, 2002.

[19] J. P. Schaffer, A. Saxena, S. D. Antolovich, J. Thomas H. Sanders, and S. B. Warner, *The Science and Design of Engineering Materials*, Second ed. Boston: McGraw-Hill, 1999.

[20] L. A. Momoda, "The Future of Engineering Materials: Multifunction for Performance-Tailored Structures," presented at Tenth Annual Symposium on Frontiers of Engineering, Irvine, CA, 2004.

[21] V.-T. Truong, B. D. Turner, R. F. Muscat, and M. S. Russo, "Conducting Polymer Based Radar Absorbing Materials," presented at SPIE - The International Society for Optical Engineering, 1997.

[22] L. Christodoulou and J. D. Venables, "Multifunctional Material Systems: the First Generation," *Journal of Materials*, vol. 55, pp. 39-45, 2003.

[23] J. P. Thomas and M. A. Qidwai, "The Design and Application of Multifunctional Structure-Battery Materials Systems," *Journal of Materials*, vol. 57, pp. 18-25, 2005.

[24] R. M. Cornell and U. Schwertmann, *The Iron Oxides*, 2nd ed. Weinheim: Wiley-VCH Verlag GmbH & Co., 2003.

[25] J. Smit and H. P. J. Wijn, *Ferrites*. Eindhoven: John Wiley and Sons, 1959.

[26] G. F. Goya, T. S. Berquo, F. C. Fonseaca, and M. P. Morales, "Static and Dynamic Magnetic Properties of Spherical Magnetite Nanoparticles," *Journal of Applied Physics*, vol. 94, pp. 3520-3528, 2003.

[27] A. E. Berkowitz, W. J. Schuele, and P. J. Flanders, "Influence of Crystallite Size on Magnetic Properties of Acicular γ-Fe_2O_3," *Journal of Applied Physics*, vol. 39, pp. 1261-1263, 1968.

[28] A. T. Ngo, P. Bonville, and M. P. Pileni, "Spin Canting and Size Effects in Nanoparticles of Nonstoichiometric Cobalt Ferrite," *Journal of Applied Physics*, vol. 89, pp. 3370-3376, 2001.

[29] J. P. Chen, C. M. Sorensen, K. J. Klabunde, G. C. Hadjipanayis, E. Devlin, and A. Kostikas, "Size-dependent magnetic properties of $MnFe_2O_4$ fine particles synthesized by coprecipitation," *Physical Review B*, vol. 54, pp. 9288-9296, 1996.

[30] K. Liu, L. Zhao, P. Klavins, F. E. Osterloh, and H. Hiramatsu, "Extrinsic Magnetoresistance in Magnetite Nanoparticles," *Journal of Applied Physics*, vol. 93, pp. 7951-7953, 2003.

[31] R. E. Partch, S. G. Gangolli, D. Owen, C. Ljungqvist, and E. Matijevic, "Conducting Polymer Composites: Polypyrrole-Metal Oxide Latexes," *ACS Symposium Series*, vol. 492 (Polymer Latexes), pp. 368-386, 1992.

[32] J. Deng, Y. Peng, C. He, X. Long, P. Li, and A. S. Chan, "Magnetic and Conducting Fe_3O_4-Polypyrrole Nanoparticles with Core-Shell Structure," *Polymer International*, vol. 52, pp. 1182-1187, 2003.

[33] S. Maeda and S. P. Armes, "Preparation and Characterization of Polypyrrole-Tin(IV) Oxide Nanocomposite Colloids," *Chemistry of Materials*, vol. 7, pp. 171-178, 1995.

[34] C.-L. Huang and E. Matijevic, "Coating of Uniform Inorganic Particles with Polymers: III. Polypyrrole on Different Metal Oxides," *Journal of Materials Research*, vol. 10, pp. 1327-1336, 1995.

[35] N. Murillo, E. Ochoteco, Y. Alesanco, J. A. Pomposo, J. Rodriguez, J. Gonzalez, J. J. d. Val, J. M. Gonzalez, M. R. Britel, F. M. Varela-Feria, and A. R. de Arellano-Lopez, "$CoFe_2O_4$-Polypyrrole Nanocomposites: New Multifunctional Materials," *Nanotechnology*, vol. 15, pp. S322-S327, 2004.

[36] A. Malinauskas, "Chemical Deposition of Conducting Polymers," *Polymer*, vol. 42, pp. 3957-3972, 2001.

[37] O. Yavuz, M. K. Ram, M. Aldissi, P. Poddar, and H. Srikanth, "Polypyrrole Composites for Shielding Applications," *Synthetic Metals*, vol. 151, pp. 211-217, 2005.

[38] Q. A. Pankhurst, J. Connolly, S. K. Jones, and J. Dobson, "Applications of magnetic nanoparticles in biomedicine," *Journal of Physics D: Applied Physics*, vol. 36, pp. R167-R181, 2003.

CHAPTER 2

BACKGROUND ON MAGNETITE AND SUPERPARAMAGNETISM

2.1 Magnetite

Magnetite (Fe_3O_4) is a naturally occurring mineral and is the first magnetic material known to man [1]. Magnetite's ability to point along the north-south direction was known as early as the 4th century in China [2]. By the 12th century, the Chinese were using magnetite to make compasses. Today magnetite is commonly found in igneous, metamorphic, and sedimentary rocks [3]. In June 2005, large deposits of sand that contains 10% of magnetite was found in the dunes of Peru. Magnetite is also found in living organisms, such as bacteria (*Aquaspirillum magnetotacticum*), bees, termites, and pigeons. The presence of this magnetic mineral provides the organisms with innate navigation capability. A picture of magnetite in its natural form is shown in Figure 2-1.

Figure 2-1. Picture of natural magnetite from Kola Peninsula, Russia , from [3]

Magnetite belongs to a family of magnetic ceramics called ferrites with a general formula of $MO{\cdot}Fe_2O_3$, where M = Fe, Ni, Co, Mn, or Cu [4]. Ferrites have either the normal spinel or inverse spinel structure, but in both cases 8 tetrahedral and 16 octahedral sites are occupied. A schematic of a general ferrite crystal structure is shown in Figure 2-2. In a normal spinel structure, the trivalent ions occupy the octahedral sites while the divalent ions reside in the tetrahedral sites. In the inverse spinel structure, the divalent ions are in the octahedral positions with eight trivalent ions and the remaining trivalent ions are found in the tetrahedral sites. Table 2-1 summarizes the distribution of metal ions in both structures. Intermediates between the two types of spinel are also possible [5].

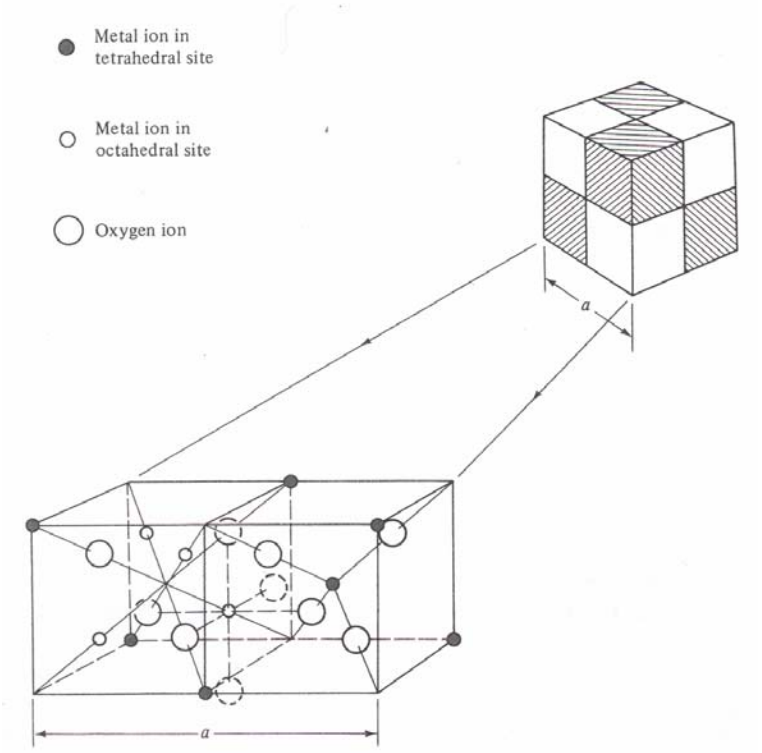

Figure 2-2. Crystal structure of ferrite, from Cullity [5]

Table 2-1. Distribution of metal ions in ferrites $MO \cdot Fe_2O_3$, from Cullity [5].

Site	Available Sites	Occupied Sites	Normal Spinel	Inverse Spinel
Tetrahedral (A)	64	8	8 M^{2+}	8 Fe^{3+}
Octahedral (B)	32	16	16 Fe^{3+}	8 Fe^{3+} 8 M^{2+}

Magnetite has the inverse spinel crystal structure with a face-centered cubic (FCC) lattice and 8 formula units per unit cell. For magnetite, Fe(III) resides in the tetrahedral and half of the octahedral sites and Fe(II) occupies the remaining octahedral sites. Because Fe(III) ions are found in both the octahedral and tetrahedral sites, they provide a path for electron transfer and magnetite has an unusually low bulk resistivity for ceramics [4].

Magnetite is a ferrimagnetic material [5]. The spins of cations in octahedral and tetrahedral sites oppose one another, but there is a still a net magnetic moment. Each magnetite molecule has a net moment of 4 μ_B (Bohr magneton) [4, 5]. Figure 2-3 is a schematic of the spin configuration in a magnetite molecule. Similar to ferromagnets, ferrimagnetic materials undergo a transition to paramagnetic behavior at Curie temperature (T_c) – which for magnetite occurs at 850K. Magnetite has an additional transition temperature at 118 K called the Verwey temperature [1, 6]. Below this temperature, the ions in the octahedral sites are ordered and the resistivity of magnetite increases [6]. The structure of magnetite changes to the triclinic structure and detection of the Verwey temperature is often used to distinguish magnetite from other iron oxides.

.

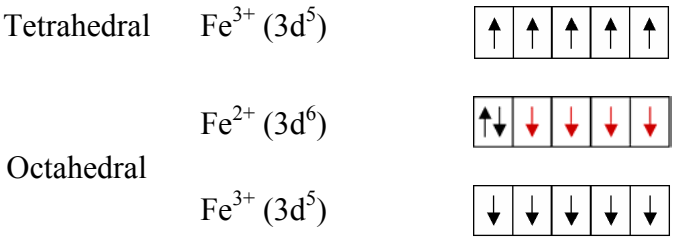

Figure 2-3. Spin arrangement in a Fe_3O_4 molecule (net spins are in red).

Magnetite has a wide range of applications, such as in magnetic storage media, paint pigment, and copier/printer toner [7, 8]. These applications typically use magnetite in the form of particles. The interest level on magnetite particles has increased recently as nanomaterials and their potential impact on technology advancement is being realized. Superparamagnetic particles are compatible for bioapplications, for example as MRI contrast agents, medium for targeted drug delivery, and protein-specific taggers [9]. In this thesis, magnetite nanoparticles will be used as fillers to make multifunctional composites. Further discussion on superparamagnetism will be presented in the next section.

2.2 Magnetism in Nanoparticles: Superparamagnetism

When the diameter of magnetic nanoparticles is small enough, each particle is a single magnetic domain. Consequently, the alignment of spins under applied field is no longer impeded by domain walls. Further reduction in particle size allows for thermal vibrations to randomly fluctuate the net spins and the domains are considered unstable. Since the particles' net spins are randomly oriented, they cancel one another and the net

moment of the collective particles is zero. If a magnetic field is applied, the particles will align producing a net moment. This behavior is characteristic of paramagnetic materials, but the difference is that each molecule has a large net moment, e.g. 4 μ_B per molecule of Fe_3O_4. Thus, Bean coined the term superparamagnetism in 1959 [5].

Superparamagnetic magnetite nanoparticles are useful for the applications described above. In low concentrations, magnetite does not present toxicity risks for humans [10]. One potential bioapplication is to coat the surface of Fe_3O_4 nanoparticles with a specific drug, which then can be given to the patient intravenously. A magnet may be used to direct the particles to the specific area of the body requiring the treatment. This can potentially increase the efficiency of the drug therapy. As fillers in composites, they can improve the modulus of the matrix and provide additional functionality such as electromagnetic interference (EMI) shielding.

There are two characteristic behaviors of superparamagnetism [5]: 1) magnetization curves, i.e. magnetization vs. applied field, do not change with temperature and 2) no hysteresis is observed, i.e. coercivity, $H_c = 0$. For nanoparticles to exhibit superparamagnetism, they must be small enough that each particle is a single domain and the energy barrier for spin reversal is easily overcome by thermal vibrations. Magnetic particles generally become single domain when they are less than 100 nm, and this limit is a function of the material properties [11]. Morrish and Yu determined that Fe_3O_4 particles are single domains when the diameter is 50 nm or less [12]. As the particle size decreases, the coercivity decreases until it reaches $H_c = 0$. At this critical particle size, the particles are superparamagnetic. The change in coercivity with particle diameter is shown in Figure 2-4.

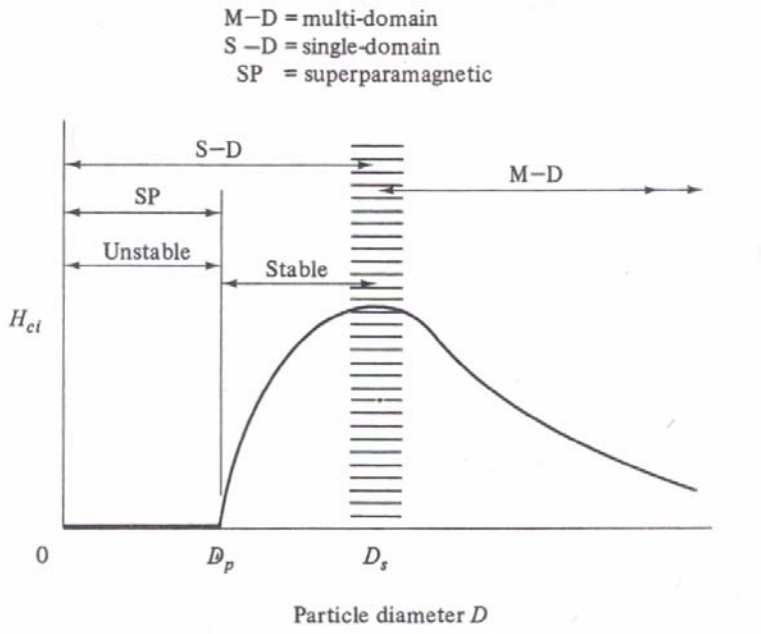

Figure 2-4. Schematic of changes in H_c with particle diameter, from Cullity [5].

Superparamagnetism behavior is observed in particle sizes that meet the following criteria [5]:

$$V_p \leq \frac{25kT}{K} \tag{2-1}$$

where V_p is the volume of the particle, k is Boltzman's constant, T is temperature, and K is the anisotropy constant. In other words, if the energy barrier, $\Delta E = KV_p$, is greater than $25kT$, the net spin within each particle cannot fluctuate randomly from thermal vibrations and they are considered stable (as in Figure 2-4). Particles that are superparamagnetic at room temperature can become stable when the temperature is lowered according to Equation 2-1. This temperature is called the blocking temperature, T_B.

Prediction of the critical particle size for onset of superparamagnetism is highly dependent on the accuracy of anisotropy constant, *K*. The anisotropy constant of nanoparticles is a contribution of different types: crystal, shape, interaction, and surface anisotropies. Crystal anisotropy is intrinsic to the material, while the others are induced or extrinsic. In a crystal, there is a preferred magnetization direction called the easy axis. If the applied field does not align with direction of the easy axis, the crystal anisotropy resists the domains from rotating and aligning with the field. As a result, higher fields must be applied to make all of the domains align. Shape anisotropy applies when the particles are not spherical, with the preferred alignment along the long axis of the particle. Exchange anisotropy is observed in small particles when they are in close contact, such as in clusters [13]. Its existence should be noted since it can change the anisotropy contribution of each particle. Surface anisotropy can contribute significantly to the overall anisotropy of nanoparticles [13, 14]. Its effect is caused by the existence of a magnetically dead layer, spin canting, and presence of disorder and defects on the surface layer [13]. The overall anisotropy energy, E_A, of a spherical nanoparticle is given by the following equation:

$$E_A = K_c V_p \sin^2 \theta + E_{\text{int}\,rxn} + E_{surface} \tag{2-2}$$

where K_c is the crystal anisotropy constant, E_{intrxn} is the contribution of interaction between particles, and D is the particle diameter.

Goya and coworkers estimated the effective anisotropy constant, *K*, of magnetite nanoparticles [14] and have accounted for bulk and surface contributions. Due to the surface effects, the anisotropy constant was increased from 1.1 x 10^4 erg/cm^3 to 3.9 x 10^4 erg/cm^3. Applying Equation (2-1) the critical diameter for superparamagnetism is

18.5 nm for Fe_3O_4. McNab *et al*. found that the anisotropy constant for magnetite nanoparticles in the size range of 10 to 20 nm is between 6.0 x 10^4 erg/cm^3 to 8.0 x 10^4 erg/cm^3 [15]. Using their values, the predicted critical diameter is 14.5 to 16 nm.

In Chapter 3, we will present the synthesis and characterization of magnetite nanoparticles with diameters that range from 5 nm to 12 nm. Therefore, we can expect to observe superparamagnetic properties in those particles. The synthesized Fe_3O_4 nanoparticles were used as fillers in composites, and analysis of their (mechanical and electromagnetic) properties will be discussed in Chapter 4.

2.3 References

[1] R. M. Cornell and U. Schwertmann, *The Iron Oxides*. Weinheim: VCH Verlagsgesellschaft, 1996.

[2] http://en.wikipedia.org/wiki/Lodestone, October 22, 2005

[3] http://en.wikipedia.org/wiki/Magnetite, October 22, 2005

[4] J. Smit and H. P. J. Wijn, *Ferrites*. Eindhoven: John Wiley and Sons, 1959.

[5] B. D. Cullity, *Introduction to Magnetic Materials*. Reading: Addison-Wesley, 1972.

[6] E. Callen, "Magnetic Properties of Magnetite," *Physical Review*, vol. 150, pp. 367-376, 1966.

[7] H. S. Lee, W. C. Lee, and T. Furubayashi, "A Comparison of Coprecipitation with Microemulsion Methods in the Preparation of Magnetite," *Journal of Applied Physics*, vol. 85, pp. 5231-5233, 1999.

[8] R. N. Rothon and M. Hancock, "General Principles Guiding Selection and Use of Particulate Materials," in *Particulate-Filled Polymer Composites*, R. N. Rothon, Ed. Essex: Longman Scientific and Technical, 1995, pp. 1-45.

[9] Q. A. Pankhurst, J. Connolly, S. K. Jones, and J. Dobson, "Applications of magnetic nanoparticles in biomedicine," *Journal of Physics D: Applied Physics*, vol. 36, pp. R167-R181, 2003.

[10] C. C. Berry and A. S. G. Curtis, "Functionalisation of magnetic nanoparticles for applications in biomedicine," *Journal of Physics D: Applied Physics*, vol. 36, pp. R198-R206, 2003.

[11] R. M. Cornell and U. Schwertmann, *The Iron Oxides*, 2nd ed. Weinheim: Wiley-VCH Verlag GmbH & Co., 2003.

[12] A. H. Morrish and S. P. Yu, "Magnetic Measurements on Individual Microscopic Ferrite Particles Near the Single-Domain," *Physical Review*, vol. 102, pp. 670-673, 1956.

[13] X. Batlle and A. Labarta, "Finite-Size Effects in Fine Particles: Magnetic and Transport Properties," *Journal of Physics D: Applied Physics*, vol. 35, pp. R15-R42, 2002.

[14] G. F. Goya, T. S. Berquo, F. C. Fonseaca, and M. P. Morales, "Static and Dynamic Magnetic Properties of Spherical Magnetite Nanoparticles," *Journal of Applied Physics*, vol. 94, pp. 3520-3528, 2003.

[15] T. K. McNab, R. A. Fox, and A. J. F. Boyle, "Some Magnetic Properties of Magnetite (Fe_3O_4) Microcrystals," *Journal of Applied Physics*, vol. 39, pp. 5703-5711, 1968.

CHAPTER 3

SYNTHESIS AND CHARACTERIZATION OF Fe_3O_4 (MAGNETITE) NANOPARTICLES

3.1 Introduction

Magnetite nanoparticles with diameters less than 20 nm are not readily available in large amounts or at reasonable cost. One of the main goals of this research is to fabricate and characterize lightweight multifunctional nanocomposites. The series of characterization tests require a substantial number of specimens, and consequently a significant supply of nanoparticles was essential for this work. This chapter will present the methods used to synthesize and characterize the magnetite nanoparticles that will be used as fillers for nanocomposites to be presented in Chapter 4.

The chapter will begin with a discussion on background and theory of metal oxide particle formation in solution. A literature survey will be presented of the common methods used to synthesize nanoparticles, and will be followed by a more focused survey on chemical coprecipitation. This information will be used to derive the process variables that control particle size and therefore must be adjusted to synthesize superparamagnetic Fe_3O_4 nanoparticles.

3.2 Synthesis of Metal Oxide Particles in Solution

The thermodynamics requirement for the precipitation of a solid phase is that the product of the reactants' activities is greater than the solubility of the solid phase. This condition is achieved when the solution exceeds a critical level of supersaturation [1, 2].

In the formation of magnetite nanoparticles, the product of ferric and ferrous ions' activities must be greater than the solubility of Fe_3O_4 and those conditions are attained at elevated temperature and high pH level. The precipitation of solid phase relieves the level of supersaturation in solution.

As shown in Figure 3-1, there are three pathways for the formation of small particles in solution [2]. In the first path, particles nucleate and then grow by diffusion. The distinct separation of the nucleation and growth processes results in the production of monodisperse particles. This pathway was first proposed by Lamer and Dinegar to explain the formation of sulfur particles [3]. In the second pathway, primary particles form during nucleation and then assemble into aggregates. In the third pathway, nucleation and growth stages are not distinct and result in polydisperse particles [2]. However, if Ostwald ripening occurs during the aging of the particles, the smaller particles preferentially dissolve and larger particles will grow at their expense until all particles reach an equilibrium size [2].

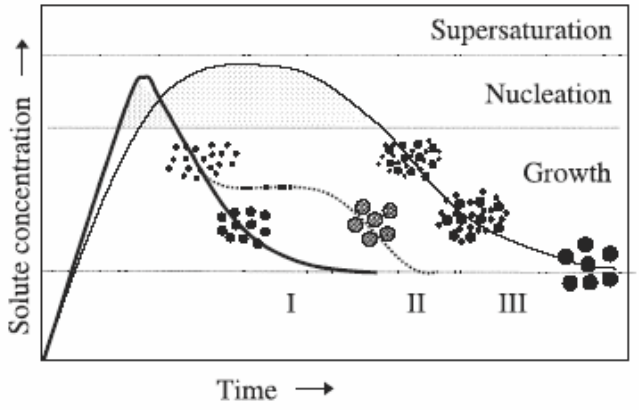

Figure 3-1. Three possible pathways for particle formation, reproduced from Tartaj *et al.* [2].

Currently there are three main methods for synthesizing metal oxide (e.g. magnetite and other ferrites) nanoparticles in solution: chemical coprecipitation [4-6], microemulsion [7-11], and decomposition of metal organic salts [12-16]. Coprecipitation is the least expensive and the simplest approach for making nanoparticles. For example, inexpensive iron salts may be mixed with a precipitating agent such as NaOH to form nanoparticles of iron oxides. In coprecipitation, the nucleation and growth steps overlap as described in the third pathway, but the particles are usually harvested in the time period before Ostwald ripening fully takes into effect.

In microemulsion, surfactants are used to physically restrict the growth of particles, but the reactants are usually the same as in coprecipitation. Because surfactants are ampiphilic, they are compatible in organic and aqueous media and consequently microemulsion reactions can take place in both media too. At a critical concentration, surfactants rearrange themselves into three dimensional structures (spheres, cylinders, or bilayers) in order to achieve thermodynamic equilibirium with their surroundings [17]. Spherical structures, i.e. spherical micelles, are of particular interest for nanoparticle synthesis because the formation of particles is confined within the micelles and their growth is limited; the micelles essentially act as microreactors [18]. By controlling the water content, type of solvent, and concentration of surfactant in solution, one can change the dimension of the spherical micelles and ultimately the particle size [18]. This method is also quite versatile, but the particles may have significant amounts of surfactant remaining on their surface. Microemulsion reactions require much larger reaction volume than chemical coprecipitation for equivalent levels of productivity.

Thermal decomposition of organic precursors is the method of choice when monodispersity is required. This method uses metal organic precursors such as metal acetylacetonates (e.g. iron (III), manganese (II), cobalt (II)) [13, 14, 16] and metal fatty acid salts (e.g. iron (II) and (III), cobalt (II), manganese (II), nickel (II), zinc (II) stearate) [15]. These precursors are decomposed in an organic medium at temperatures (200°C to 340°C) much higher than the coprecipitation reaction temperature [13, 15]. Consensus suggests that the monodispersity of particles is due to distinct steps of nucleation and growth, and recently published data by Hyeon *et al.* support that theory [12]. Although this procedure can yield uniform nanoparticles with diameters that range from 3 nm to 16 nm, process scale-up is challenging due to the extreme temperature requirements. A TEM image of 6 nm particles that illustrates the monodispersity of particles formed from a decomposition reaction is shown in Figure 3-2.

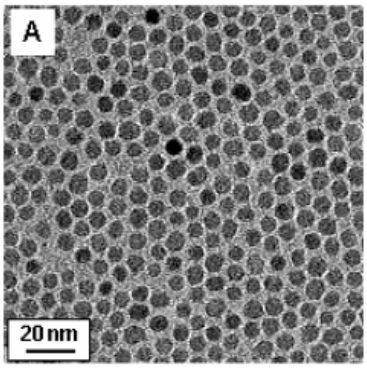

Figure 3-2. TEM image of 6 nm Fe_3O_4 particles synthesized by decomposition of iron (III) acetylacetonate ($Fe(acac)_3$) from Sun *et al*. [14].

3.3 Synthesis of Fe_3O_4 (Magnetite) Nanoparticles by Chemical Coprecipitation

Chemical coprecipitation was selected as the method to synthesize nanoparticles for this study. This method produces nanoparticles in large quantities (order of grams) in a relatively short amount of time and utilizes inexpensive and readily available chemicals as precursors. These two advantages are important in the fabrication of nanocomposites whose potential applications will require a specimen mass of tens of grams. A sample with filler loading of approximately 5 volume% requires a few grams of nanoparticles. Since samples with higher volume fractions were desired, the demand for nanoparticles increased very quickly.

Although coprecipitation was first reported in 1925 by Welo and Baudisch, who studied phase transformation of iron oxide with temperature [19], the work by Massart [4] is most cited by contemporary research groups. The main purpose of early research work involving coprecipitation was to study the magnetic behavior in single domain structures [20-22], but current studies on synthesized magnetic nanoparticles are focused on potential applications and improving the quality of the nanoparticles (i.e. monodispersity and crystallinity).

The versatility and simplicity of coprecipitation has made it one of the preferred techniques to produce nanoparticles. The same procedure is used to synthesize other types of ferrites, such as $MnFe_2O_4$ and $CoFe_2O_4$, by simply changing the metal salt precursors [23-27]. Nanoparticles produced by coprecipitation are usually polydisperse, but generally spherical in shape. However, depending on the reaction conditions, some groups have reported faceted geometries, (e.g. cubic particles) [28].

The coprecipitation reaction to form magnetite is described simply by the following equation [24, 28]:

$$Fe^{2+} + 2Fe^{3+} + 8OH^- \rightarrow Fe_3O_4 + 4H_2O \quad (3\text{-}1)$$

Ferrous ions are easily oxidized, and the products may deviate from the desired stoichiometric ratio of ferric to ferrous ions. Therefore precipitation is performed under inert atmosphere to avoid side products, which will affect the purity of the final product. Examples of side reactions and their products are [29]:

$$Fe_3O_4 + 0.25O_2 + 4.5H_2O \rightarrow 3Fe(OH)_3 \quad (3\text{-}2)$$

$$2Fe_3O_4 + 1/2O_2 \rightarrow 3Fe_2O_3 \quad (3\text{-}3)$$

In coprecipitation, ferric and ferrous salts are dissolved in an aqueous solution and undergo accelerated hydrolysis to produce particles of iron oxides with single domain structures. A number of studies have been conducted over the years on the hydrolysis of ferric and ferrous ions to form different phases of iron oxides/hydroxides. The objectives of these studies were to determine the phases that form at different process conditions and to understand the mechanisms for their formation. The morphology of the product was discussed but was not the main focus of these studies. There are many different phases of iron oxides and oxyhdroxides that are possible and the final phases are highly dependent on the process variables [30-35]. The results of these studies indicate that the formation of iron oxides and hydroxides are dependent on temperature, pH, and type of anions used in the reaction. The sizes of particles in this study are larger, on the order of tens to hundreds of nanometers. Nevertheless, they will provide background information for the formation of magnetite nanoparticles by chemical coprecipitation.

In aqueous conditions, ferric and ferrous salts are known to dissociate and then form hexa-aquo (hydrated) ions [36]:

$$FeCl_3 + 6\ H_2O \rightarrow Fe(H_2O)_6^{3+} + 3Cl^- \quad (3\text{-}4)$$

$$FeCl_2 + 6\ H_2O \rightarrow Fe(H_2O)_6^{2+} + 2Cl^- \quad (3\text{-}5)$$

Under favorable conditions of high pH and elevated temperature (≥ 60°C), the hexa-aquo ions hydrolyze and form polynuclear complexes [36-38]. Hydrolysis reactions of various metal salts are well studied, including Al^{3+}, Ti^{4+}, Zr^{4+}, Cr^{3+}, Y^{3+}, Ce^{4+}, Zn^{2+}, and Ga^{3+} [37]. Most metal ions tend to form strong bonds with oxygen and hydroxyl ion ligands, including Fe2+ and Fe3+. Generally, metal cations with higher valency undergo hydrolysis more readily [37], therefore ferric ions hydrolyze more readily than ferrous ions.

A simple hydrolysis reaction is described by the following equation [37], where z is the valency of the ion and n is the number of sequence of hydrolysis steps.

$$Fe(H_2O)_6^{z+} + H_2O \rightarrow Fe(H_2O)_{(6-n)}(OH)_n^{(z-n)+} + H_3O^+ \quad (3\text{-}6)$$

The possible products from hydrolysis of both ferric and ferrous ions are listed in Table 3-1. A more general hydrolysis reaction is described by Equation (3-7) that accounts for formation of dimers and trimers listed in Table 3-1. In this equation, the water ligands have been omitted for clarity.

$$mFe(H_2O)_6^{z+} + xH_2O \rightarrow Fe_m(H_2O)_y(OH)_{(nm-y)}^{(zm-y)+} + xH_3O^+ \quad (3\text{-}7)$$

Figure 3-3 summarizes metal complex formation as a function of pH and valency. Metal ions with valency of +2 and +3 form hydroxo complexes under basic conditions. For example, both $Fe(OH)_4^-$ and $Fe(OH)_3^-$ are the dominant hydrolysis products at pH

12-14 for ferric and ferrous ions, respectively. Only $Fe(OH)_3$ exists in both acidic and basic conditions [36].

Table 3-1. Products of hydrolysis reactions [37].

Fe^{2+}	Fe^{3+}
$Fe(OH)^+$	$Fe(OH)^{2+}$
$Fe(OH)_2$	$Fe(OH)_2^+$
$Fe(OH)_3^-$	$Fe(OH)_3$
$Fe(OH)_4^{2-}$	$Fe(OH)_4^-$
	$Fe_2(OH)_2^{4+}$
	$Fe_3(OH)_4^{5+}$

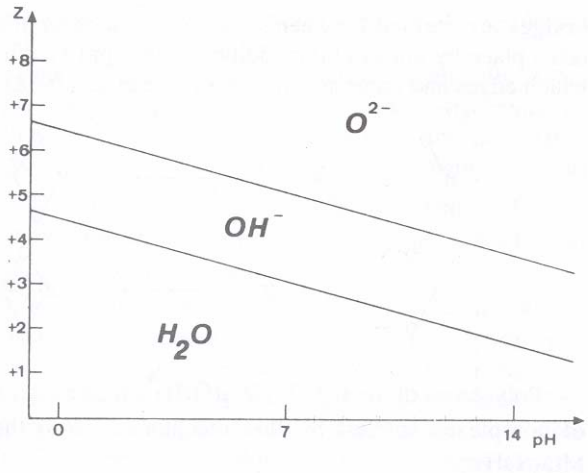

Figure 3-3. Dependence of metal complex with pH and its valency, from Otterstedt and Brandredth [37].

The products of hydrolysis assemble into polynuclear complexes by olation or oxolation reactions and they subsequently evolve through similar condensation reactions

to form small particles of iron oxides or hydroxides [37]. The pH level plays a major role in determining the dominant condensation reactions that occurs between hydrolysis products [37]. In olation reactions, metal atoms are bridged together by hydroxyl groups to form polynuclear complexes and water as the byproduct [37]. A schematic of the reaction is shown in the following figure:

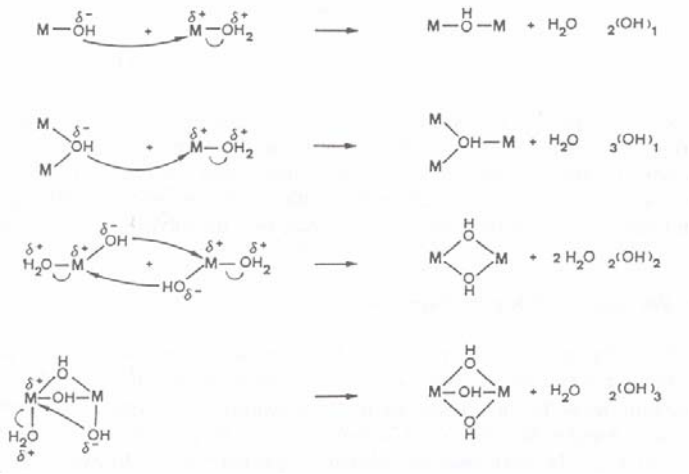

Figure 3-4. Olation reactions to form polynuclear complexes, from Otterstedt and Brandredth [37]

Some of the hydroxy bridges formed by olation mechanism are unstable and can result in particles of the composition $MO_{x/2}(OH)_{(z-x)}$, e.g. FeOOH [37], such as shown below:

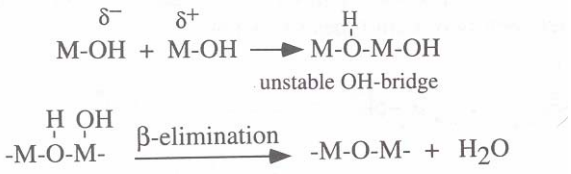

Figure 3-5. Oxolation reaction from an unstable hydroxyl bridge, from Otterstedt and Brandredth [37].

The oxolation reactions take place in a wider range of pH, and the end result of this type of assembling process is the precipitation of small particles of metal oxides, as shown in Figure 3-6, e.g. Fe_2O_3 and Fe_3O_4 where M is Fe

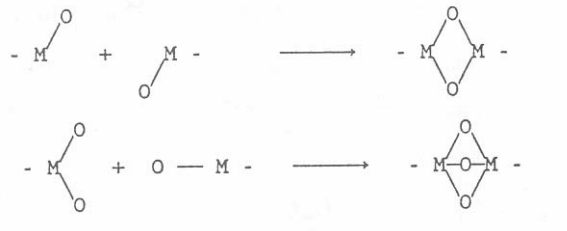

Figure 3-6. Oxolation reaction, from Otterstedt and Brandredth [37]

Misawa *et al.* [30, 39] characterized the polynuclear complexes that precede the formation of iron oxides and oxyhydroxide and clarified the structures of the polynuclear complexes and their roles as intermediates. Three different reactions that produce Fe_3O_4 were discussed, and the one that pertains to coprecipitation is of a solution containing Fe^{2+} and Fe^{3+}. When base is added into the solution, a dark red complex, $[Fe(II)Fe(III)_2O_x(OH)_{2(3-x)}]_m^{2m+}$, is formed and its reaction is shown below.

$$m\mathrm{Fe}^{2+} + 2m\mathrm{Fe}^{3+} + 6m\mathrm{OH}^- \rightarrow [\mathrm{Fe(II)Fe(III)_2O}_x(\mathrm{OH})_{2(3-x)}]_m^{2m+} + mx\mathrm{H_2O} \qquad (3\text{-}8)$$

The complex has the same ratio of ferric to ferrous ions as in magnetite. Subsequently, the dark red complex will begin to precipitate out into fine black particles of Fe_3O_4 when more OH^- ions are added and the pH of the solution is at least 7.2, which is consistent with the alkaline conditions required for chemical coprecipitation [5].

A study that focused on the synthesis and morphology of Fe_3O_4 particles is by Regazzoni *et al.* [40]. That study found that temperature, type of anion, degree of

heterogeneity during alkalinization, stirring of the solution, and time of aging played significant roles in control of morphology. Furthermore, they determined that methods starting with ferrous hydroxide generally gave rise to polydisperse particles.

Systematic studies on chemical coprecipitation for the production of nanoparticles are not well documented. Most of the studies on chemical coprecipitation and Fe_3O_4 nanoparticles (less than 20nm) only focused on one variable or described one process condition yielding particles with a certain set of properties. The work here will present a more comprehensive and systematic study on chemical coprecipitation.

Some information can be collected from a survey of published results on the different ways process conditions are used to control the size of Fe_3O_4 particles. Table 3-2 summarizes the results of the survey. The most common iron salts used in chemical coprecipitation are $FeCl_2$ and $FeCl_3$. However, there are several groups who selected ferric nitrate and ferrous sulfate in place of $FeCl_3$ and $FeCl_2$, respectively. The majority of the groups used NaOH or NH_4OH as the precipitating agent, but some used tetramethylammonium hydroxide ($N(CH_3)_4OH$ or TMAOH) because it can prevent the particles from agglomerating. Reaction temperatures range from room temperature to 100°C with reported nanoparticle diameter ranging from 2 nm to 51 nm.

Table 3-2. Overview of published results on synthesis of Fe_3O_4 using chemical coprecipitation.

Source of Fe^{2+}	Source of Fe^{3+}	Precipitating Agent	Temperature	Particle Size (diameter)	Ref.
$FeCl_2$	$FeCl_3$	NaOH	RT and 80°C	6 nm and 12nm	[29] Kim
$FeCl_2$	$FeCl_3$	NH_4OH	RT	12nm	[4] Massart
$FeCl_2$	$FeCl_3$	NH_4OH	80°C	3-15nm	[41] Fried
$FeCl_2$	$FeCl_3$	NaOH	Not listed	8.5 nm	[5] Kang
$FeCl_2$	$Fe(NO_3)_3$	NaOH	88°C	7nm	[6] Gee
$FeSO_4$	$FeCl_3$	NH_4OH	Not listed	7.5nm	[42] Ma
Not reported	Not reported	NaOH	80°C	5.5 nm (0.5), 12.5 nm (1.0)	[43] Zhu
$FeCl_2$	$FeCl_3$	NH_4OH	RT	3-11 nm	[44] Qu
$FeCl_2$	$FeCl_3$	NH_4OH	30-90°C	8.4-51nm	[28] Liu
$FeSO_4$	$FeCl_3$	NaOH	Heated	11.8nm	[45] Hong
$FeCl_2$	$FeCl_3$	NaOH	70°C	Not listed	[38] Wu
$FeCl_2$	$Fe(NO_3)_3$	NaOH NH_4OH $N(CH_3)_4OH$	25°C and 45°C	2-12.5 nm	[46] Vayssieres

The literature survey on chemical coprecipitation has shown that temperature was a major factor in controlling particle size, where the increased reaction temperature led to larger particle size [28, 29]. This may be an indication that the particle growth is diffusion limited. Studies on hydrolysis of ferric and ferrous ions indicate that both pH and temperature may be significant factors. However, the impact of pH was not consistent since some studies showed that particle size decreases with increasing pH level [4], but may increase it under some conditions [38].

3.4 Chapter Objectives and Overview

It is apparent that magnetite may be synthesized using chemical coprecipitation at a wide range of conditions, as reported by many groups. However, published work on systematic studies to vary the size of Fe_3O_4 nanoparticles by chemical coprecipitation and to measure their corresponding magnetic properties is lacking. Therefore, the major focus of the following research is to identify and to understand the process variables that influence magnetite particle size, and to correlate their size to their magnetic properties. This task will provide the process recipes for synthesizing nanoparticles to be used as fillers in magnetic nanocomposites.

Nanoparticle qualities on the order of one to two grams will be prepared. Magnetization and coercivity measurements of particles at varying diameters will formulate a relationship between particle size and magnetic properties. Available published data will be added to reinforce analysis of the functional relationship between magnetic properties and particle size. Furthermore, determination of a size-functional relationship will serve the research community at large, since variation of magnetic properties with particle size would facilitate the nanoparticles' use as magnetic taggers [47].

3.5 Experimental

3.5.1 Design of Experiment

Based on the data from a literature survey on chemical coprecipitation, the initial design of experiment matrix design has three process variables (total iron concentration, $[Fe^{2+}] + [Fe^{3+}]$; pH or [OH-]; and temperature) and two levels (high and low) for each

variable. Using a full factorial design, there are $2^3 = 8$ conditions to be tested. By systematically designing an experiment matrix, the data can be analyzed to identify variables that have a significant impact on the targeted response (in this case, particle size) and to identify any variable interactions. Table 3-3 shows the experiment matrix and the combination of test conditions that will be conducted. Data from the initial experiment matrix provided guidance for selecting which variables should be tested further. For the process variable that shows a strong influence on particle size, additional levels will be studied. At the end of this study, 25 different combinations of chemical coprecipitation processes were completed. The synthesized particles range in size (diameter) from 5 nm to 12 nm.

Table 3-3. Experiment matrix 1 for chemical coprecipitation with three variables and two levels.

Condition or Sample No.	$[Fe^{2+}] + [Fe^{3+}]$	$[OH^-]$	Temperature
1	0.9 M	0.5 M	65°C
2	1.8 M	0.5 M	65°C
3	0.9 M	3.0 M	65°C
4	1.8 M	3.0 M	65°C
5	0.9 M	0.5 M	95°C
6	1.8 M	0.5 M	95°C
7	0.9 M	3.0 M	95°C
8	1.8 M	3.0 M	95°C

3.5.2 Synthesis of Fe_3O_4 Nanoparticles

In a 100 mL 3-neck flask, ferric salt, such as $Fe(NO_3)_3 \cdot 9H_20$ or $FeCl_3 \cdot 6H_2O$, was dissolved in 12.5 mL of distilled water to produce a solution with a concentration that is specified in the experiment matrix (Table 3-3) and purged with nitrogen for at least 30 minutes. Ferrous salts were then added in the form of $FeCl_2 \cdot 4H_20$ while the nitrogen purge was continued. In a 500mL 3-neck flask, NaOH was dissolved in 125 mL of distilled water to achieve the desired concentration that is listed in Table 3-3. The basic solution was purged with nitrogen and then heated in an oil bath to reaction temperature. When the reaction temperature was reached, the solution of iron salts was added dropwise into the basic solution. Black precipitates formed immediately upon addition of the iron salt solution. The reaction solution was mixed vigorously for 30 minutes (from where the iron salt was added). The reaction time was kept constant for this study.

At the end of the 30 minutes, the flask was removed from the heated oil bath. A permanent magnet was used to separate the particles. The supernatant was decanted and the particles were rinsed three times with approximately 150 mL of distilled and deoxygenated water. The particles were rinsed with approximately 100 mL of 0.01M HCl to neutralize them. The particles were filtered, then collected, and were dried in an oven at 75-80°C for 4 hours.

3.5.3 Characterization of Particles

Transmission Electron Microscope (TEM)

The transmission electron microscope (TEM) is an essential tool to visually analyze nanomaterials. TEM has the capability to view nanostructures because the wavelength of an electron beam can be adjusted to a few hundredth of an angstrom. The wavelength of the electron beam, λ, is a function of its voltage as shown in the following equation [48]:

$$\lambda = \frac{1.226}{\left[U_o(1 + 0.9788 \times 10^{-6} U_o)\right]^{1/2}} \tag{3-9}$$

where U_o is the voltage of the electron beam. In this work, TEM images were collected at magnifications ranging from 100,000X to 190,000X at 100kV (λ = 0.037 Å) using a JEOL 100CX II TEM.

When a sample is inserted in the path of an electron beam, the transmitted beam is affected by the sample. Electrons are scattered when they interact with the specimen and the change in beam intensity results in phase contrast, thereby a projection of the sample is viewed on the image plane.

To prepare TEM samples, a drop of solution containing dispersed nanoparticles was placed on a TEM grid and then left to dry in air. The best results were obtained using carbon-coated copper grids (200-300 mesh). Some samples were prepared using holey or lacey carbon-coated copper grids, but those grids are best suited for capturing a single particle for high-resolution TEM studies.

A dispersed solution was prepared by first collecting a small amount of nanoparticle slurry at the final rinsing step just prior to the filtration step.

Approximately 1 mL of that concentrated slurry was added into 25 mL solution of 0.01M HCl and $1X10^{-3}$M sodium dodecylbenzene sulfonic acid (NaDBS), followed by sonication for approximately 5 minutes to disperse the nanoparticles.

X-Ray Diffraction (XRD)

X-Ray diffraction (XRD) is extremely valuable because its data are used to determine the sample's crystallinity, confirm its phase, and measure the average crystal size. The basis of diffraction is Bragg's law, which describes the condition when diffraction occurs in a crystalline material [49]:

$$n\lambda_x = 2d\sin\theta \tag{3-10}$$

where λ_x is the wavelength of the X-ray beam, d is the lattice spacing, θ is the angle of the beam with respect to the plane of the lattice, and n is the order of the lattice plane. In other words, when the wavelength of the incoming x-ray is at a specific angle, the rays will diffract coherently from the lattice planes and the scattered rays mutually reinforce one another producing a signal peak. This is shown schematically in Figure 3-7.

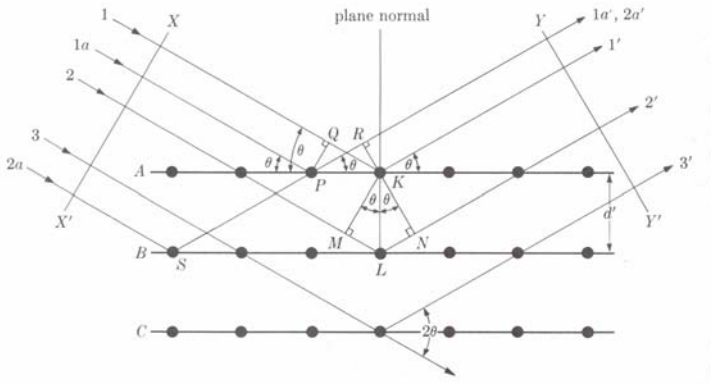

Figure 3-7. Diffraction of x-rays by a crystal, from Cullity [49].

The peaks of an XRD spectrum is governed by atoms in the unit cell while their intensity is a function of the structure, Lorentz-polarization, multiplicity, and temperature factors. XRD peaks can be predicted using the structure factor, F_{hkl}, in Equation (3-11):

$$F_{hkl} = \sum_{1}^{N} f_n e^{2\pi i(hu_n + kv_n + lw_n)} \tag{3-11}$$

where N is the number of atoms in the unit cell, n represents the identity of the atom, (hkl) are the Miller indices of the lattice plane, and uvw are the coordinates of the atoms in the unit cell. The intensity is a contribution of several factors, as shown in the following equation:

$$I = \left|F_{hkl}\right|^2 p\left(\frac{1+\cos^2 2\theta}{\sin^2\theta\cos\theta}\right)e^{-2M} \tag{3-12}$$

where p is the multiplicity factor, the quantity in brackets is the Lorentz-polarization factor, and the last quantity is the temperature factor (M is a function of scattering angle, θ, and of atom displacement due to thermal vibration).

The unit cell of Fe_3O_4 is face-centered cubic (FCC) and the structure of magnetite is inverse spinel. There are eight formula units per unit cell. The peaks that are systematically absent for an FCC structure represent lattice planes with both even and odd indices. Therefore, one can expect only peaks from lattice planes with all even or all odd indices in the XRD spectra of Fe_3O_4 particles.

X-rays are created when high-speed electrons collide with a metal target causing electrons in the target to be excited to a shell of higher energy. Subsequently an electron in a higher energy shell fills the resulting vacancy and releases its residual energy as x-

rays. That process is illustrated in Figure 3-8. K lines are most useful in XRD since the longer wavelengths are too easily absorbed by the sample. Therefore, the energy of the electrons aimed at the target must be high enough to displace K electrons out of their shells. X-rays are characteristic of the energy difference between K, L, and M shells, thus their wavelengths depend on the target element used to create the X-rays, as shown in Table 3-4.

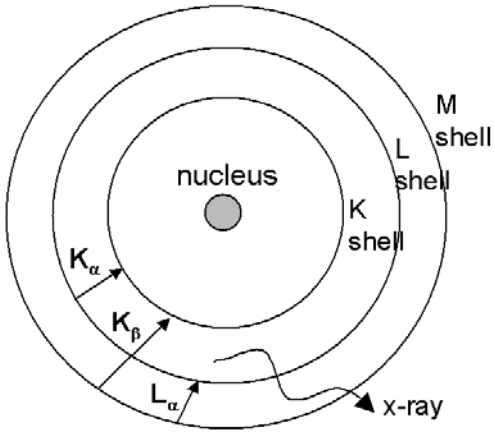

Figure 3-8. Schematic of x-ray production from electronic transitions.

Table 3-4. List of characteristic x-ray wavelengths for different targets.

Target Element	Kα (Å)
Cr	2.291
Fe	1.937
Co	1.790
Cu	1.541
Mo	0.711

XRD spectra of the particles were collected on the Phillips PW-1800 diffractometer, which uses a copper target. LaB_6 was used as a standard to measure the inherent peak broadening of the equipment.

Vibrating Sample Magnetometer

A vibrating sample magnetometer (VSM) was used to collect the hysteresis behavior of nanoparticles at room temperature. VSM was developed by Foner in 1959, and a schematic of its configuration is shown in Figure 3-9 [50]. The basis of the method is that a flux change is induced when a vibrating magnetic sample is placed within a uniform magnetic field. The detection coils measure a voltage, which is compared with the voltage of the reference sample. The difference between the two voltages is proportional to the sample's magnetic moment.

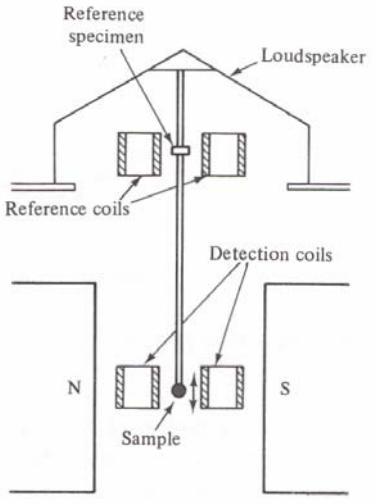

Figure 3-9. Configuration of a typical VSM, from Cullity [50].

A VSM was used to measure the hysteresis of Fe_3O_4 particles. The raw data collected was of the total moment of the sample. This value is dependent on sample size, but by accounting for the weight of the sample, a set of specific properties was obtained. The magnetic properties of interest are saturation magnetization, M_s, and coercivity, H_c, as indicated in Figure 3-10.

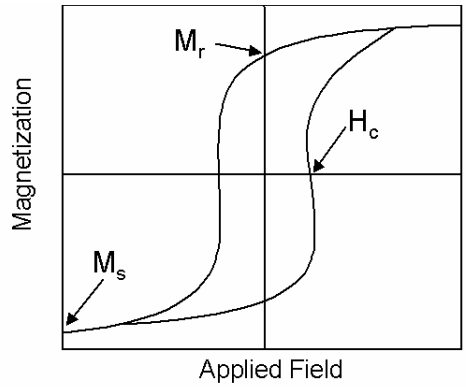

Figure 3-10. Schematic of magnetic hysteresis data from VSM.

A system by Lakeshore VSM Model 3700 was used for this work. Two measurements were collected for each sample: 1) a high field sweep from ±10,000 Oersted and 2) a low field sweep from ±1,000 Oersted. The intent of the high field experiment was to measure the saturation magnetization of the samples. The low field measurement was performed to measure the coercive field with a small applied field increment to improve resolution of the measurement. The measurement conditions for low field and high field experiments are listed in the table below.

Table 3-5. Measurement parameters for the VSM.

	High Field ±10,000 Oersted	Low Field ±1,000 Oersted
Time constant	0.1	0.1
Time per pt	3 seconds	3 seconds
Field increment	60 Oe	5 Oe
Field ramp rate	16.6 Oe/sec	1.66 Oe/sec

Particles were pressed into pellets about 5 mm in diameter and between 1 to 2 mm in thickness so that they can be mounted easily on the VSM sample holder. Particles were blended with a commonly used binder, polyvinyl alcohol (PVA), using a mortar and pestle. The pressed pellet consisted of about one-third magnetic particles and two-thirds PVA (by weight). The weight of the magnetic particles was used to calculate the specific moment (emu per gram) of each sample.

The pellet mold was machined from a teflon rod by the GTRI Machine Shop. A Carver Laboratory Press was used to shape the pellet at forces ranging from 2500 – 3000 lb_f, which translates to approximately 97,000 psi (670 Mpa).

3.6 Results and Discussion

3.6.1 Properties of Nanoparticles

Morphology and Phase

TEM provided a method for viewing the shape of the particles and determining the particle sizes, however, it was not the primary method. The TEM used in this study is not optimized for high-resolution analysis, i.e. greater than 200,000X, which was needed to accurately measure particle size. Therefore, XRD was used as the primary method for which particle size will be determined, and TEM images were used to validate XRD data with visual evidence.

Typical TEM images of the synthesized particles, such as those synthesized using condition number 1, Table 3-3, is shown in Figure 3-11. Particles are spherical with diameters that range from 8-11 nm. Although the particles were dispersed with the help of a surfactant and a sonicator, they still had a propensity to agglomerate and this

was more apparent when using lacey or holey carbon TEM grids. Better results were usually obtained with carbon grids.

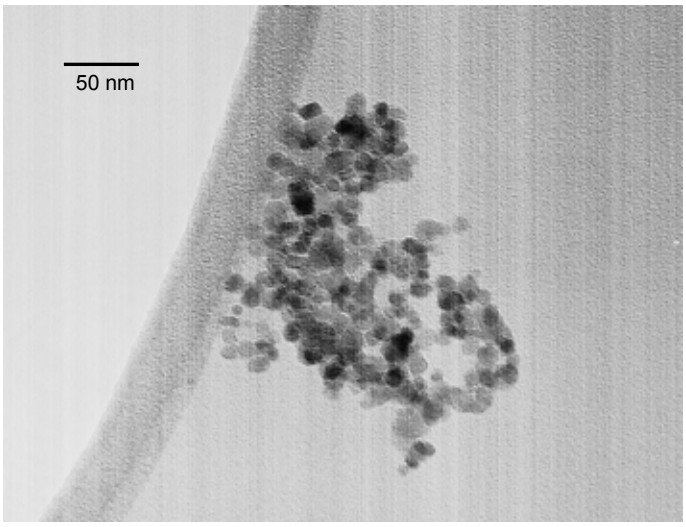

(a)

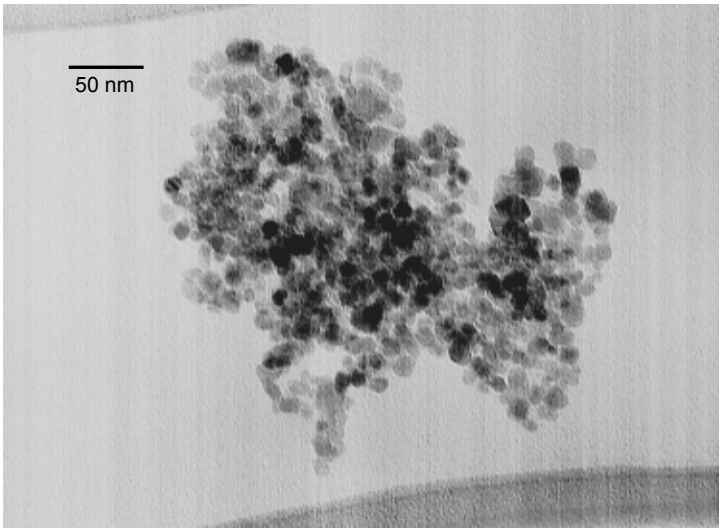

(b)

Figure 3-11. TEM images of particles synthesized using condition #1 of Table 3-3.

XRD spectra of the synthesized nanoparticles showed distinct peaks, indicative of their crystallinity. Spectra from Samples 1 and 6 of Table 3-3 are shown in Figure 3-12, which are representative data of the particles synthesized in this study. There is a significant amount of noise in the spectrum, typical of samples containing iron. Iron produces excessive fluorescence when Cu target is used to produce the x-ray beam [51]. These fluorescence do not contribute to the characteristic peaks but contribute to the background level.

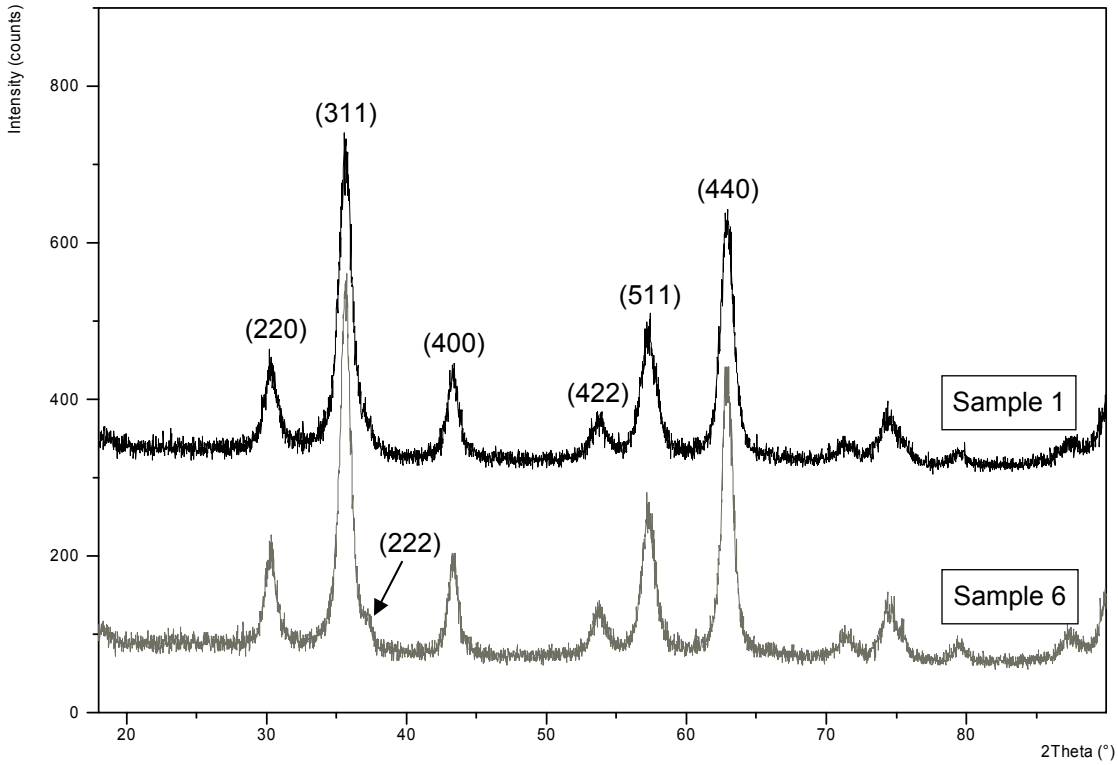

Figure 3-12. Representative XRD spectra of synthesized Fe_3O_4 particles.

As shown in Figure 3-12, the peaks correspond with the JCPDS (Joint Committee on Powder Diffraction Standards) card for magnetite (19-0629). It is

difficult to discern the (222) peak from the (311) peak due to broadening, but there is a distinctive shoulder at 2θ ~ 37° indicating that the (311) peak partially overlapped with the (222) peak [52], as shown in the spectrum of Sample 6. The spectra of samples with crystallite size smaller than 10 nm, e.g. Sample 1, did not show the (222) peak because the broadening of the (311) peak will be larger and will encompass the (222) peak.

The average crystallite size of the nanoparticles was determined using Scherrer's equation, which can be applied to crystals that are as large as 100 nm [49]:

$$t = \frac{k\lambda}{B\cos\theta} \tag{3-13}$$

where t = crystallite size, k=0.89, λ = 1.54Å (Cu K_α), θ = peak position, and B = effective full width half maximum (FWHM) of peak (440). The (440) peak was selected for particle size determination because there would be greater error associated with the more intense (311) peak, which overlapped with the (222) peak.

The effective FWHM of the peak separates the contribution of the broadening inherent in the equipment, which was measured using a standard compound, LaB_6. To ensure that there would be no other contribution to peak broadening, the standard sample was collected at the same conditions as those used for the nanoparticles. The spectrum of the standard compound is shown in Figure 3-13. The broadening inherent to the equipment in the vicinity of the (440) peak, 2θ = 62° to 65°, was measured to be 0.078°. An assumption was made that the peaks have a Cauchy distribution and therefore the effective FWHM can be determined by simply subtracting 0.078° from the FWHM of the (440) peak for each sample. To verify that there is no residual stress that can contribute to peak broadening, a Williamson-Hall curve was plotted for Sample 2 as

shown in Figure 3-14. If there were contribution from stress, the broadening at higher angles would be much greater than at lower angles.

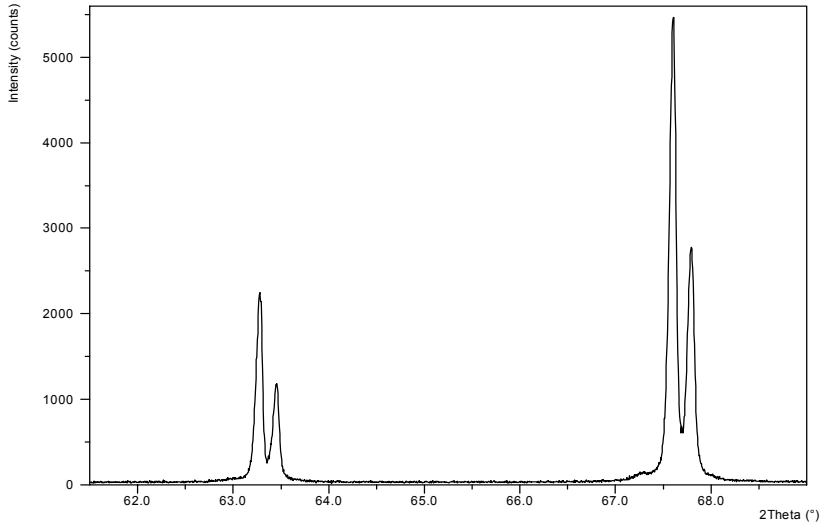

Figure 3-13. XRD spectrum of standard compound LaB_6 collected at the same settings as the nanoparticle samples.

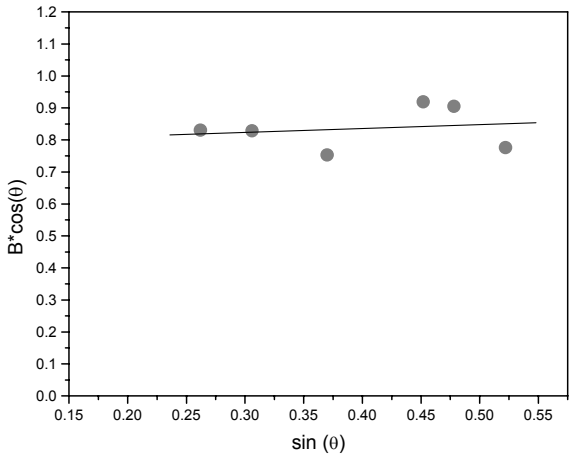

Figure 3-14. Williamson-Hall plot for Sample 2.

After calibrating for broadening from the equipment, the crystallite size of Samples 1 and 6 was determined to be 8.9 nm and 10.7 nm, respectively. A comparison of the crystallite size with the particle size from TEM images shows that they are approximately the same. Therefore, it can be inferred that the particles are single crystals and consequently, XRD data can be used to determine the particle size. Not only does this method provide a better representation of the average particle size than counting particles from TEM images, it is also more expedient.

Magnetic Properties

Magnetic properties of the nanoparticles were measured at room temperature using a VSM. High field conditions were used to assure that saturation magnetization was achieved and measured. Once again, Samples 1 and 6 will be used to illustrate typical analysis of the nanoparticles. The hysteresis curves of both samples are shown in Figures 3-15 and 3-16. For Sample 1, M_s is 49.61 emu/g Fe_3O_4 and for Sample 6, M_s is 54.05 emu/g Fe_3O_4. The saturation magnetizations of the nanoparticles are lower than the M_s of the bulk phase (M_s is 92-100 emu/g Fe_3O_4), and the measured decrease is consistent with literature [53, 54]. Analysis of the relationship between particle size and magnetic properties will be discussed in greater detail in the upcoming sections.

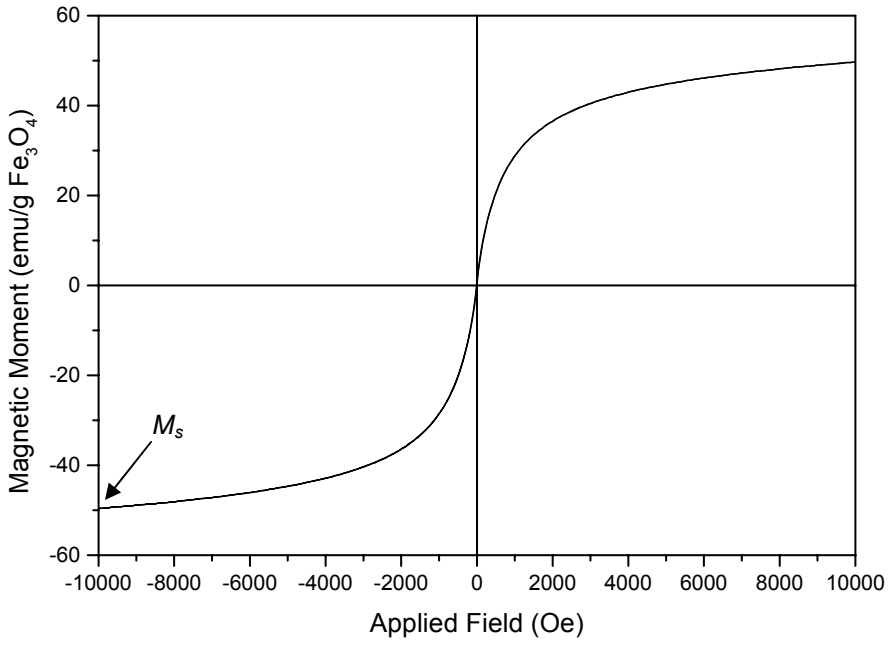

Figure 3-15. Hysteresis of Sample 1, ±10,000Oe.

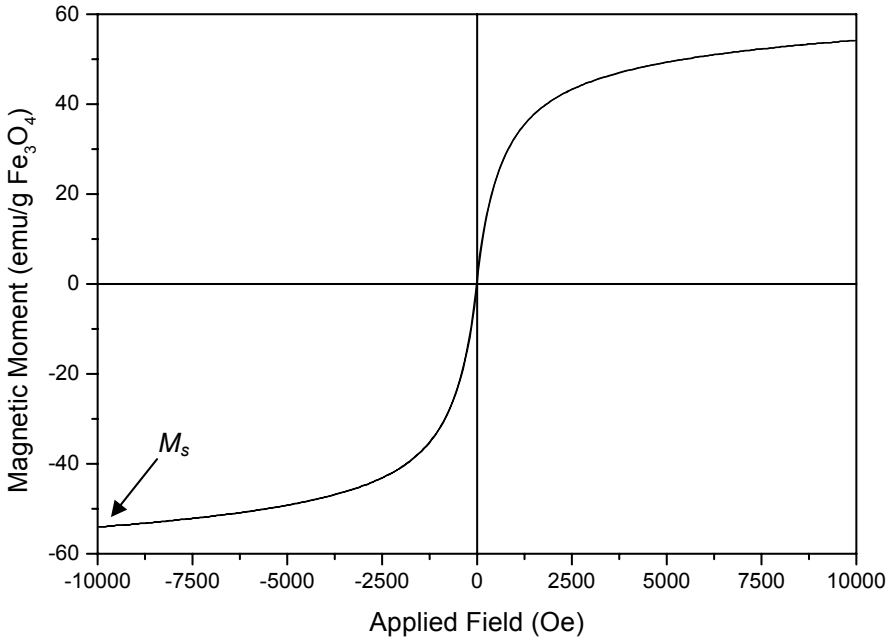

Figure 3-16. Hysteresis of Sample 6, ±10,000Oe.

The low field measurement conditions were used to measure the coercivity of the samples. The hysteresis curve of Sample 1 is representative of nanoparticles with diameters less than 10 nm, and shows that its H_c is less than 1 Oersted (Figure 3-17). Measurement of a sample known to be superparamagnetic at room temperature (provided by Prof. Y.K. Hong of University of Idaho) was conducted on this VSM and its coercivity is 1 Oersted. The observation that H_c only approached zero may be a contribution of dipolar interactions between particles, which increases the effective anisotropy constant. Particles were pressed into pellets for VSM measurements, and they formed clusters passivated by PVA, but particle interactions within the cluster may have contributed to the effective anisotropy constant. Therefore for this VSM study, samples with $H_c \leq 1$ will be grouped as $H_c \cong 0$. Since one of the conditions for superparamagnetism is for $H_c \sim 0$, Sample 1 may be considered superparamagnetic.

The coercivity of Sample 6 is 6 Oersteds (Figure 3-18), but its average particle size is less than 20 nm, which should fall below the superparamagnetic size limit at room temperature (from Chapter 2). The TEM images clearly show that the nanoparticles are polydisperse, so it is possible that particles larger than 20 nm in diameter contributed to the small hysteresis. Therefore, Sample 6 can be considered to be partially superparamagnetic.

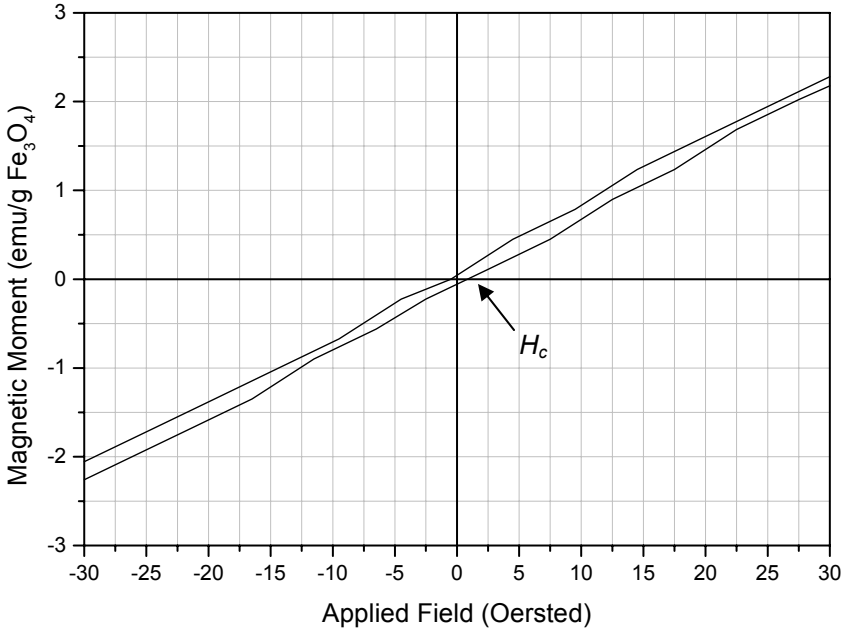

Figure 3-17. Hysteresis of Sample 1, ±1,000Oe.

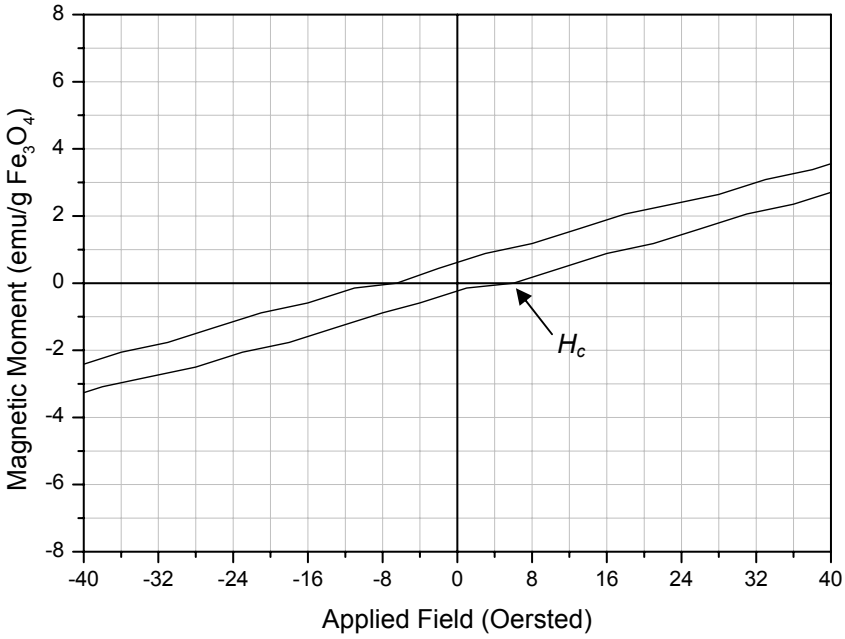

Figure 3-18. Hysteresis of Sample 6, ±1,000Oe.

3.6.2 Analysis of Experiment Matrix 1

The size, magnetization, and coercivity of magnetite particles synthesized with process conditions listed in the experiment matrix (Table 3-3) were measured and they are summarized in Table 3-6. The analysis was conducted using particle size as the response and the assistance of statistical software, Minitab V.14. The software graphically summarized the average responses for each process variable and that is presented in Figure 3-15. A quantitative experiment analysis is an option but that would require multiple samples for each process condition, thereby increasing the time and cost of the study. Since the main purpose of the first experiment matrix is to identify variables that strongly influences particle size and eliminate those that do not. The qualitative approach that was implemented here will suffice. Furthermore, additional experiments were conducted to verify the trends observed from this set of experiment.

The main effects plot in Figure 3-19 qualitatively shows that the total concentration of iron had the most influence on particle size: the higher the initial iron concentration, the larger the particles. A similar trend was observed by Tang *et al.* when they increased the total concentration of metal salts in their reaction to make $MnFe_2O_4$ nanoparticles [25].

The effect of temperature was less significant than originally expected, especially given the results reported in two other independent studies [28, 29]. However, this study varied temperature over a smaller range than those two studies, e.g. room temperature to 85°C. Therefore, the temperature effect was more amplified in those two studies.

The effect of pH was also less significant than iron concentration. Hydrolysis reactions become more favorable as the alkalinity of the solution is increased [36, 37], so it is reasonable to expect more of the iron to participate in nucleation, which subsequently results in less iron available during particle growth. In such situations, the average particle size should be smaller when the pH is higher.

Data showed that the trends discussed above for pH and temperature were not consistent in all conditions. These inconsistencies implied some interaction between pH and temperature. Thus, additional experiment matrices were designed and completed to validate the observed trends.

Table 3-6. Experiment Matrix 1 and measured properties of nanoparticles.

Condition or Sample No.	Total $[Fe^{z+}]$	$[OH^-]$	Temperature	Particle Size (nm)	M_s (emu/g)	H_c (Oersted)
1	0.9 M	0.5 M	65°C	8.9	49.61	0.75
2	1.8 M	0.5 M	65°C	9.5	53.66	3.0
3	0.9 M	3.0 M	65°C	8.5	46.31	1.5
4	1.8 M	3.0 M	65°C	10.6	52.94	6
5	0.9 M	0.5 M	95°C	9.5	51.16	2.25
6	1.8 M	0.5 M	95°C	10.7	54.05	6
7	0.9 M	3.0 M	95°C	8.4	46.12	0.65
8	1.8 M	3.0 M	95°C	10.0	51.73	4

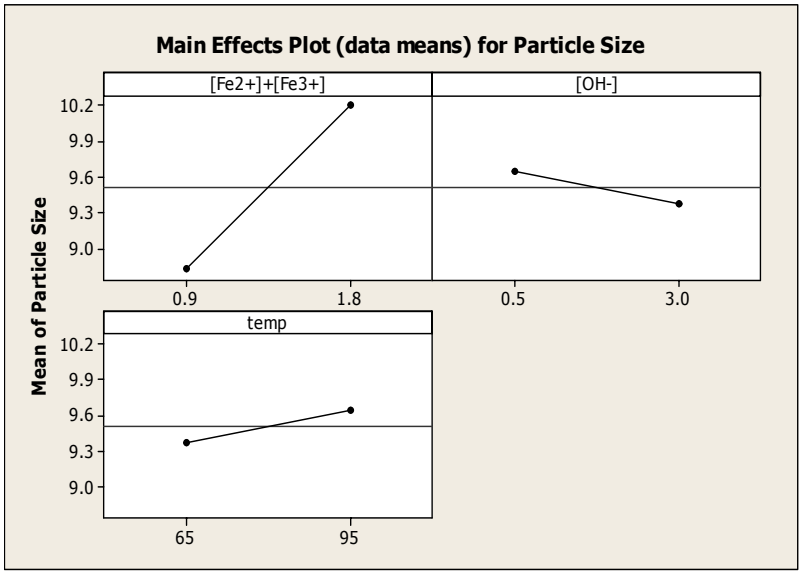

Figure 3-19. Results of design of experiment Matrix 1.

3.6.3 Analysis of Experiment Matrix 2

In the initial experiment matrix, the particle size increased when the iron salt concentration was increased. The range of the iron salt concentration was expanded in the second experiment matrix to verify that trend. The second experiment matrix and the measured nanoparticle properties are shown in Table 3-7.

Process conditions where the iron salt concentration of 2.3 M with a base concentration of 0.5 M were not included in the matrix since Fe_3O_4 particles did not form under those conditions. The precipitates were reddish brown and did not contain magnetic properties. It is theorized that the precipitates were some combination of FeOOH and α-Fe_2O_3 since they had the appearance of those phases [36]. Equation (8) predicts that the ratio of $[Fe^{z+}]/[OH^-]$ in the total reaction solution must be at least 0.5 for the dark red complex to form, and at these conditions ($[Fe^{z+}]$ = 2.3M and $[OH^-]$ =0.5M), the ratio was only 0.46. Furthermore, the final pH of the solution after the precipitates

formed was less than 2 – another indicator that the reaction solution was not alkaline enough. To form the precipitates, sufficient OH^- ions are required to deprotonate the hydroxy bridges in the complex and produce Fe_3O_4. Therefore, for process conditions that called for [OH-] = 0.5 M, only [Fe^{z+}] = 0.4 M was added to the second experiment matrix.

Table 3-7. Experiment Matrix 2 with expanded range of [Fe^{z+}].

Sample ID	Total [Fe^{z+}]	[OH-]	Temperature (°C)	Particle Size (nm)	M_s (emu/g)	H_c (Oersted)
9	0.4	0.5	65	8.8	51.01	1.5
1	0.9	0.5	65	8.9	49.61	0.75
2	1.8	0.5	65	9.5	53.66	3.0
10	0.4	3.0	65	7.7	40.23	1.5
3	0.9	3.0	65	8.5	46.31	1.5
4	1.8	3.0	65	10.6	52.94	6
11	2.3	3.0	65	10.6	52.07	6.75
12	0.4	0.5	95	8.5	46.34	0.5
5	0.9	0.5	95	9.5	51.16	2.25
6	1.8	0.5	95	10.7	54.05	6
13	0.4	3.0	95	8.2	48.11	0.2
7	0.9	3.0	95	8.4	46.12	0.65
8	1.8	3.0	95	10.0	51.73	4
14	2.3	3.0	95	10	50.50	8.25

The measured variation in particle size with iron salt concentration is plotted in Figure 3-20. It is apparent that increasing iron salt concentration is a way to control particle size, but its effectiveness hits a plateau at higher concentrations. At both 65°C and 95°C, particle size was approximately equal at iron salt concentration 1.8 M and 2.3 M. However, the coercivities are slightly larger for the ones synthesized at the higher

iron concentration. This may imply a wider distribution of particle size, i.e. larger particles that are not superparamagnetic contributed to H_c.

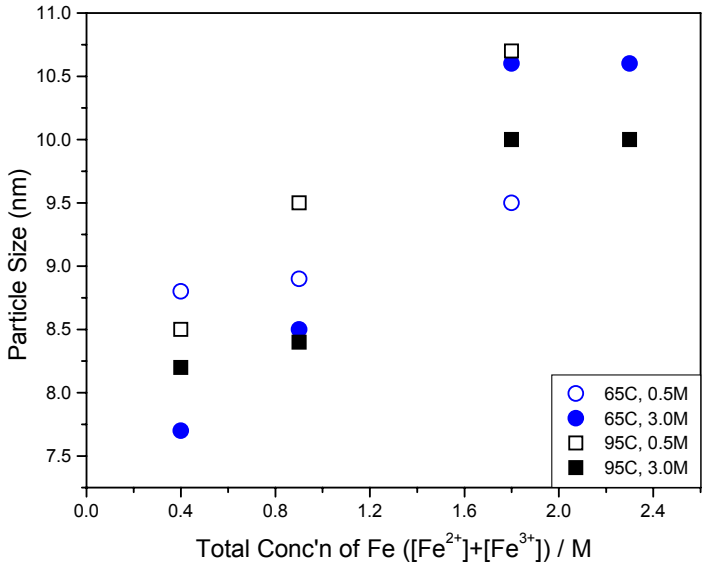

Figure 3-20. Plot of particle size with $[Fe^{Z+}]$.

Increased temperature is thought to increase particle size [28]. Reasoning suggests that ions diffuse through solution faster at higher temperatures, and the increased diffusion rate enables faster growth of particles. In fact, at [OH-] = 3.0M, the data show decreased size with increasing temperature. We theorize that since hydrolysis is more favorable at higher temperatures and in solutions with greater alkalinity, the concentration of iron salt in solution is consumed faster during nucleation. This causes the supply of iron in solution to deplete much earlier in the reaction thereby leaving less iron for particle growth.

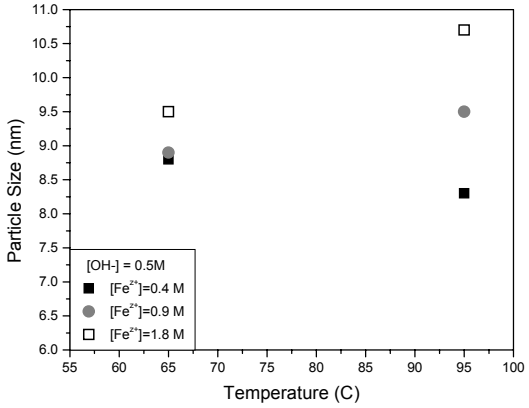

(a)

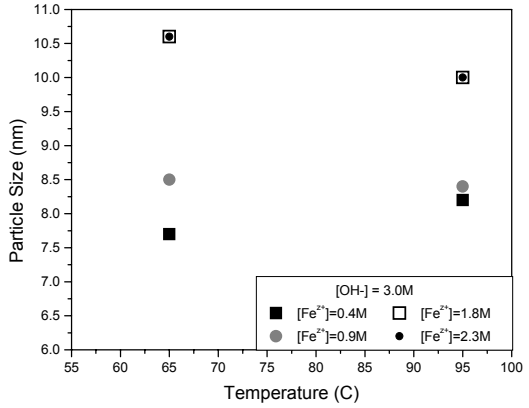

(b)

Figure 3-21. Plot of particle size with temperature at

(a) $[OH^-] = 0.5M$ and (b) $[OH^-] = 3.0M$.

TEM analysis indicates that temperature impacts the morphology of particles. Nanoparticles produced at 65°C are rounded and spherical. However, particles produced at 95°C appear more angular in shape; particles are generally cubic, with some showing a pyramidal shape. A similar observation was made by Liu *et al.* [28], where

they found cubic particles at reaction temperature 90°C. The intended application of these nanoparticles is fillers in composites. A more isotropic shape, such as spheres, is generally more desirable because sharp corners in fillers can create high stress concentration areas, which are weak points and may catalyze crack growth and induce failure [55]. Therefore, a reaction temperature of 65°C was used in production of particles for nanocomposites.

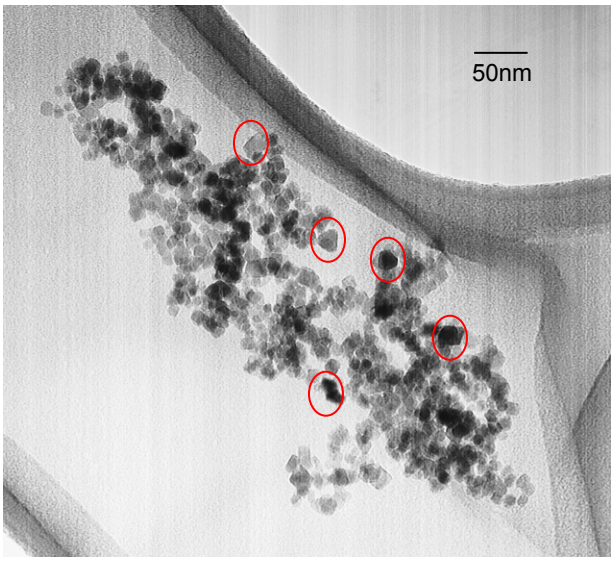

Figure 3-22. TEM image of faceted particles (Sample 7) reaction temperature 95°C.

The majority of data shows that particles are smaller when the base concentration is higher, as shown in Figure 3-23, and this trend is consistent with other publications [4, 46] . The sample synthesized with iron salt concentration of $[Fe^{Z+}]$ = 1.8M, [OH-] = 3.0M, and T = 65°C deviates from this trend. When particle size is plotted against a normalized variable, $[Fe^{Z+}]/[OH^{-}]$, the process conditions at $[Fe^{Z+}]$ = 1.8M and [OH-] = 3.0M at both 65°C and 95°C show a spike in the data set, as shown in Figure 3-24. The

ratio $[Fe^{z+}]/[OH^-] = 0.06$ is equivalent to the process condition $[Fe^{z+}] = 1.8M$ and [OH-] = 3.0M, and appears to be an optimum ratio to produce larger particles. An explanation for this has not been identified, but one possible reason is that the variables pH and temperature interact and the observed trends were a combined effect. Further studies are necessary to elucidate this behavior.

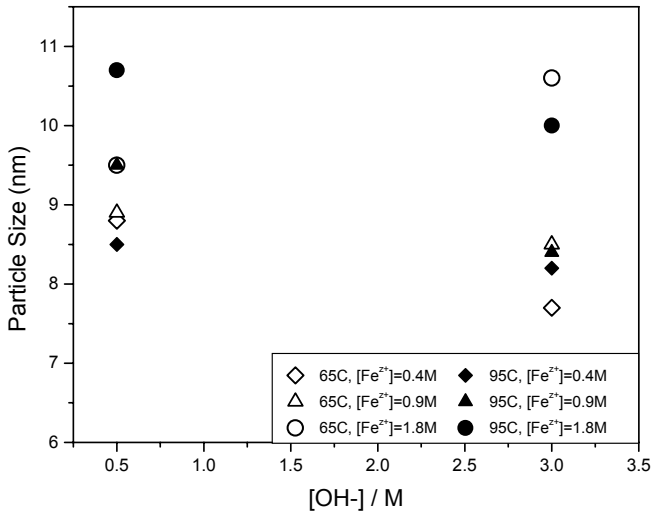

Figure 3-23. Plot of particle size with [OH-].

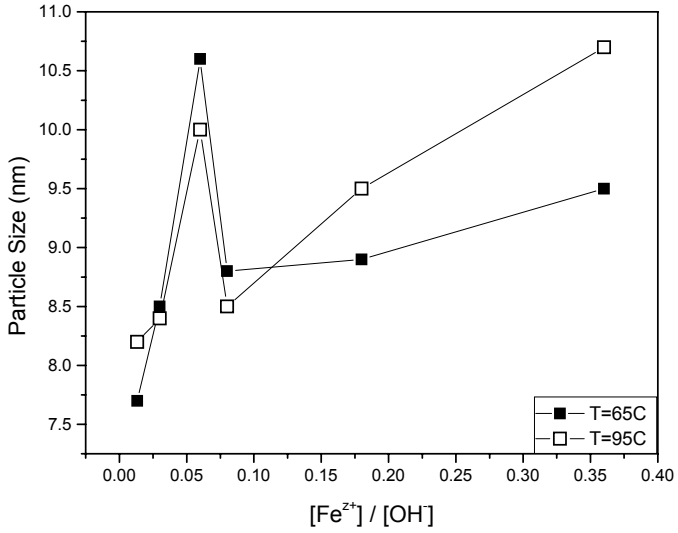

Figure 3-24. Plot of particle size with $[Fe^{z+}]/[OH^-]$.

3.6.4 Other Particle Size-Controlling Variables

Ratio of Ferric to Ferrous Ions

The stoichiometric ratio of Fe(II) to Fe(III) in magnetite is 0.5. Some studies show that adjusting that ratio can be significant in controlling particle size and morphology [6, 43]. Ferric and ferrous salts have different solubilities, and generally ferrous salts are less soluble. At room temperature the solubilities of $FeCl_2$ and $FeCl_3$ are comparable, but the solubility of $FeCl_3$ increases much faster with temperature than that of $FeCl_2$ [56], as shown in Figure 3-25. One goal of this study is to produce spherical nanoparticles. Gee *et al.* found that by having equal amounts of $FeCl_2$ and $FeCl_3$, the particles are more spherical [6]. At 60°C and 80°C, $FeCl_3$ is 1.37 times more soluble than $FeCl_2$. To compensate for this difference, the ratio of $FeCl_2$ to $FeCl_3$ should

be increased to 0.7. The effect of ferric to ferrous salts ratio was examined and the experiment matrix is shown in Table 3-8.

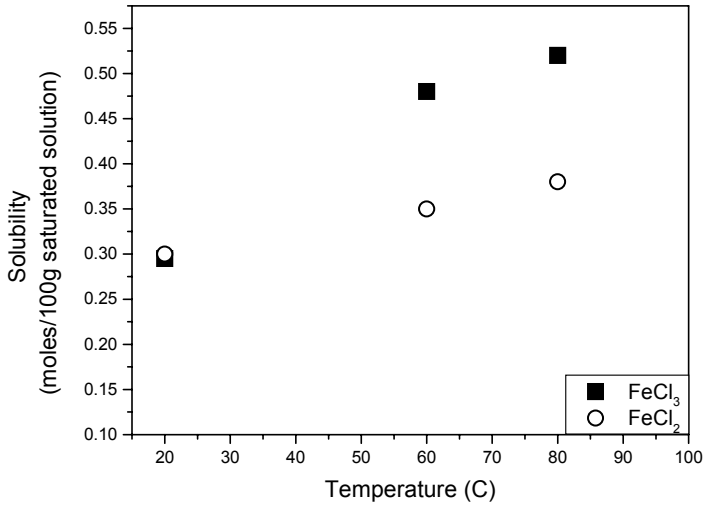

Figure 3-25. Solubility of $FeCl_2$ and $FeCl_3$ in water.

Table 3-8. Experiment matrix studying effect of ferric to ferrous ions ratio.

Sample No.	Total $[Fe^{z+}]$	$[OH^-]$	Temp.	$[Fe^{2+}]$: $[Fe^{3+}]$	Particle Size (nm)	M_s (emu/g)	H_c (Oersted)
2	1.8 M	0.5 M	65°C	0.5	9.5	53.66	3.0
3	0.9 M	3.0 M	65°C	0.5	8.5	46.31	1.5
5	0.9 M	0.5 M	95°C	0.5	9.5	51.16	2.25
8	1.8 M	3.0 M	95°C	0.5	10.0	51.73	4
15	1.8 M	0.5 M	65°C	0.7	12.0	57.84	9
16	0.9 M	3.0 M	65°C	0.7	10.2	52.50	3.50
17	0.9 M	0.5 M	95°C	0.7	10.0	53.99	8.75
18	1.8 M	3.0 M	95°C	0.7	10.7	53.28	7.25
19	1.8 M	0.5 M	65°C	1.0	11.8	58.99	11

This experiment found that ferric to ferrous ion ratio has a strong effect on the particle size and shape. Nanoparticles' properties are also summarized in Table 3-8 and the particle size is plotted against $[Fe^{2+}]$:$[Fe^{3+}]$ in Figure 3-27. The condition that showed the largest particle sizes was at $[Fe^{z+}]$ = 1.8M, [OH-] = 0.5M, and $[Fe^{2+}]$:$[Fe^{3+}]$ = 0.7 and 1.0. Figure 3-26 shows the TEM images of Samples 15, and 19. The presence of excess ferrous ions yields larger and rounder particles. Conditions where there is excess ferrous ions produced rounder particles and that observation was supported by Gee at al. at $[Fe^{2+}]$:$[Fe^{3+}]$ = 1.0, so that ratio is used to produce nanoparticles for composites.

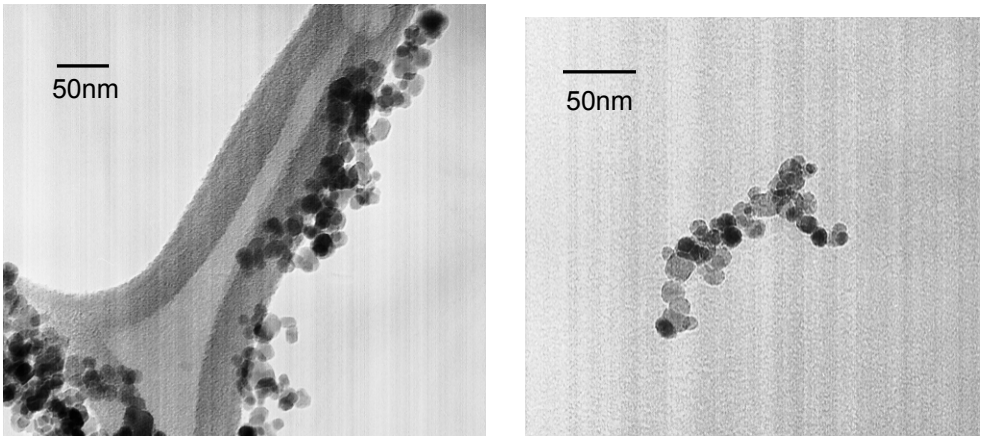

(a) (b)

Figure 3-26. TEM images of Samples (a) 15 and (b) 19.

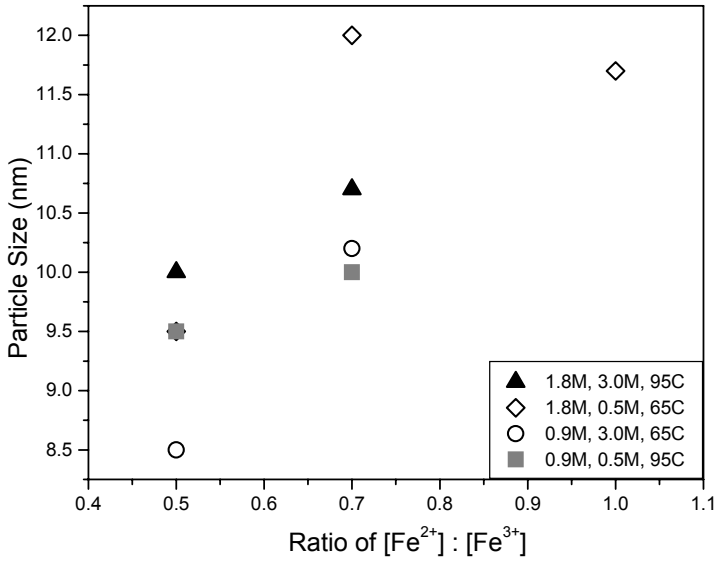

Figure 3-27. Plot of particle size with $[Fe^{2+}]$:$[Fe^{3+}]$.

Ionic Strength of Solution and Source of Iron Salt

The ionic strength of a solution can be adjusted by the addition of electrolyte and it was found to be a major factor in controlling particle size in the study by Vayssieres *et al.* [46]. The presence of a noncomplexing electrolyte, such as $NaNO_3$, in the reaction solution reduces the particles' surface potential and stabilizes the newly formed particles. In their study, Vayssieres *et al*. compared the effectiveness of $NaNO_3$, NH_4NO_3, and $N(CH_3)_4NO_3$ as electrolytes. They found that electrolytes with smaller cations were better at stabilizing particles, and as a result they selected $NaNO_3$ for further study. Increasing the concentration of $NaNO_3$ allows more surface areas, i.e. smaller particles, to be stabilized. Consequently, they found that smaller particles were formed with increasing ionic strength ($NaNO_3$ concentration).

The effect of electrolyte was studied in this section and the experiment matrix is shown in Table 3-9. It also includes the properties of the synthesized particles. Sample 19 from the previous section and Sample 3 from Experiment Matrix 1 were used as control, and KNO_3 was the electrolyte instead of $NaNO_3$. Since the cations of KNO_3 and $NaNO_3$ are both monovalent and belong to the same group in the periodic table, one can expect KNO_3 to be just as effective in stabilizing particles as $NaNO_3$. Figure 3-28 shows that the addition of KNO_3 in the reaction solution reduced particle size. The particles decreased in size by 35% when 0.75 M of KNO_3 was used. Further increase of ionic strength to 1.5 M did not result in additional reduction in particle size. To verify that the effect of KNO_3 is not unique to those conditions, KNO_3 was amended to process condition of Sample 3, and yielded Sample 22, which was 60% smaller than Sample 3 particles. KNO_3 was proven to be effective in reducing particle size in the same manner as reported for $NaNO_3$.

Table 3-9. Experiment matrix for studying effect of ionic strength.

Sample No.	Total $[Fe^{z+}]$	$[OH^-]$	Temp.	$[Fe^{2+}]$: $[Fe^{3+}]$	$[KNO_3]$	Particle Size (nm)	M_s (emu/g)	H_c (Oersted)
19	1.8 M	0.5 M	65°C	1.0	0 M	11.8	58.99	11
20	1.8 M	0.5 M	65°C	1.0	0.75 M	7.7	42.22	1
21	1.8 M	0.5 M	65°C	1.0	1.50 M	7.6	37.50	<1
3	0.9 M	3.0 M	65°C	0.5	0 M	8.5	46.31	1.5
22	0.9 M	3.0 M	65°C	0.5	0.75M	5.1	25.58	<1

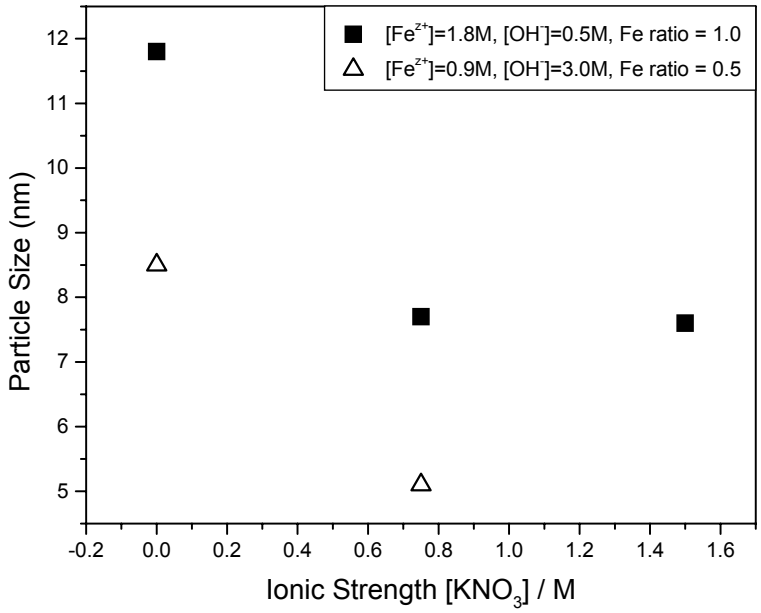

Figure 3-28. Effect of ionic strength on particle size.

It was discussed earlier that some publications on coprecipitation reported using different types of iron salts, such as nitrates and sulfates [6, 45, 57]. Systematic study on the effect of iron salt type on particles size had not been reported before. The impact of salt type on particle size was briefly studied, along with the combined effects of Fe^{3+} source and ionic strength, as summarized in Table 3-10. The new samples are 23-25 and Samples 4, 19, and 20 are included in the table as baselines. Particle sizes are plotted against process variables in Figure 3-29. The use of ferric nitrate in place of chloride salt reduced the particle size by 72% and 57% for Samples 23 and 24, respectively. The solubility of $Fe(NO_3)_3$ (0.19 mols/100g sat. solution at T=25°C) is much lower than that of $FeCl_3$ (0.30 mols/100g sat. solution at T=25°C) [56]. With a lower solubility, the activity of the ferric ion would be lower in solution, and the driving force for

precipitation is reduced. When KNO_3 is present in the reaction solution, the size reducing effect of using ferric nitrate is less. This was observed in Sample 25, which only showed a 5% decrease in particle size.

Table 3-10. Experiment matrix for studying effect of iron salt.

Sample No.	Total $[Fe^{z+}]$	$[OH^-]$	Temp.	$[Fe^{2+}]$: $[Fe^{3+}]$	$[KNO_3]$	Particle Size (nm)	Fe^{3+} source	M_s (emu/g)	H_c (Oe)
19	1.8 M	0.5 M	65°C	1.0	0 M	11.8	$FeCl_3$	58.99	11
23	1.8 M	0.5 M	65°C	1.0	0 M	8.5	$Fe(NO_3)_3$	50.42	2.5
4	1.8 M	3.0 M	65°C	0.5	0 M	10.6	$FeCl_3$	52.94	6.75
24	1.8 M	3.0 M	65°C	0.5	0 M	6.1	$Fe(NO_3)_3$	31.95	<1
20	1.8 M	0.5 M	65°C	1.0	0.75 M	7.7	$FeCl_3$	42.22	1
25	1.8 M	0.5 M	65°C	1.0	0.75 M	7.3	$Fe(NO_3)_3$	39.25	<1

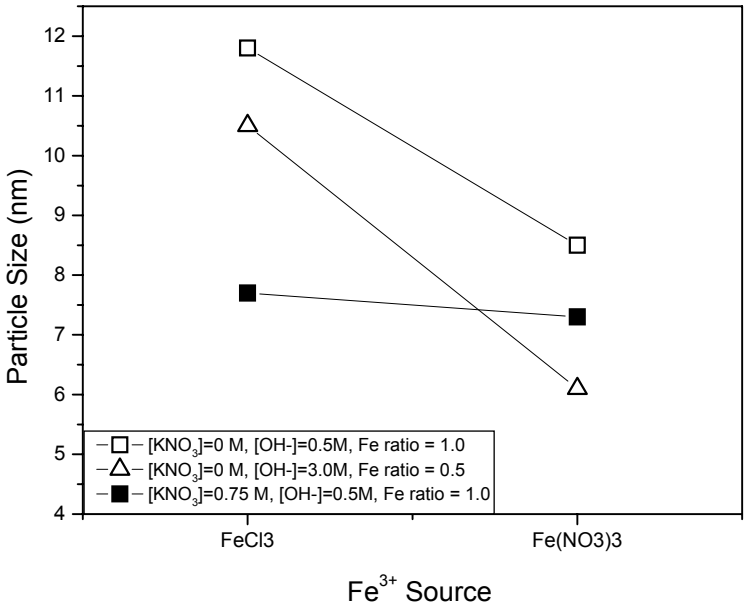

Figure 3-29. Effect of Fe^{3+} source and ionic strength on particle size.

3.6.5 Analysis of Functional Relationship Between Particle Size and Magnetic Properties

This thesis investigates multifunctional (electrical, magnetic, and mechanical) properties of composites using nanoparticles as fillers. To understand magnetic composites the properties of the nanoparticle fillers must be investigated first. The coprecipitation experiments produced 25 samples of Fe_3O_4 nanoparticles with diameters ranging from 5 nm to 12 nm. Magnetization and coercivity measurements were performed on those samples to develop a model that predicts $M_s(R)$ for Fe_3O_4.

The synthesized particles showed a strong correlation between magnetic properties and particle size. A number of publications also have observed a dependence of M_s with the particle size and have attributed this to dominating surface effects [23, 50, 58-60]. As illustrated in Figure 3-30, the ratio of surface area to volume per particle increases significantly as particle size decreases. Fe_3O_4 at the surface is not surrounded by a lattice structure as in bulk phase, thus electrical, magnetic, and chemical properties are expected to differ from bulk Fe_3O_4. Since the properties of free surfaces differ from the bulk, properties of nanoparticles are expected to deviate from bulk properties more significantly as the contribution from the surface increases.

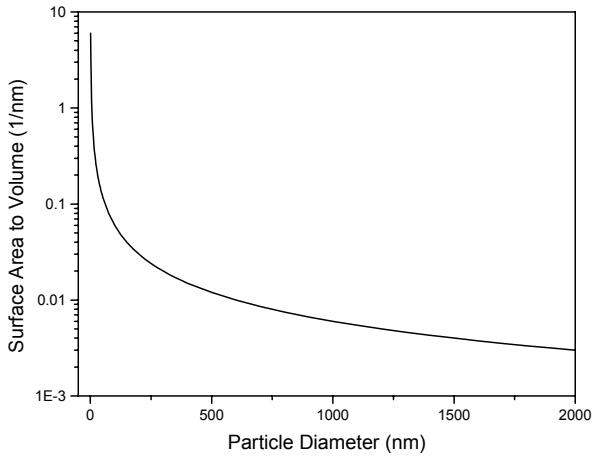

Figure 3-30. Ratio of surface area to volume with particle size.

In general, saturation magnetization and coercivity of the synthesized particles decreased as the particle size decreased. This observation is not unique to magnetite nanoparticles, but is also true for other ferrites [23, 59]. The decrease in coercivity, H_c, at room temperature with particle size is observed when the size of the particles is small enough that each particle is a single domain [50]. The decrease with decreasing particle size continues and at a critical size, $H_c = 0$. For particles at or smaller than this critical value, they are superparamagnetic. That critical value for magnetite can range from 14-19 nm (see superparamagnetism discussion in Chapter 2), depending on the anisotropy constant used in the calculation. Figure 3-31 shows a plot of measured H_c with particle size (diameter), and the relationship can be approximated to be linear at the region near the critical value [50].

From the data of the particles synthesized here, $H_c = 0$ when $D_p = 7.75$ nm. The observed critical size is smaller than the predicted values calculated in Chapter 2. As previously discussed, the coercivity was measured using a VSM where the particles

were pressed into pellets. The interaction between particles may effectively increase the anisotropy constant of the samples during measurement. Particles that were not perfectly spherical can also increase the effective anisotropy constant [61]. Furthermore, the synthesized particles have a size distribution and the larger particles may not be superparamagnetic and have nonzero coercivity. These factors can delay the onset of superparamagnetism to smaller particles.

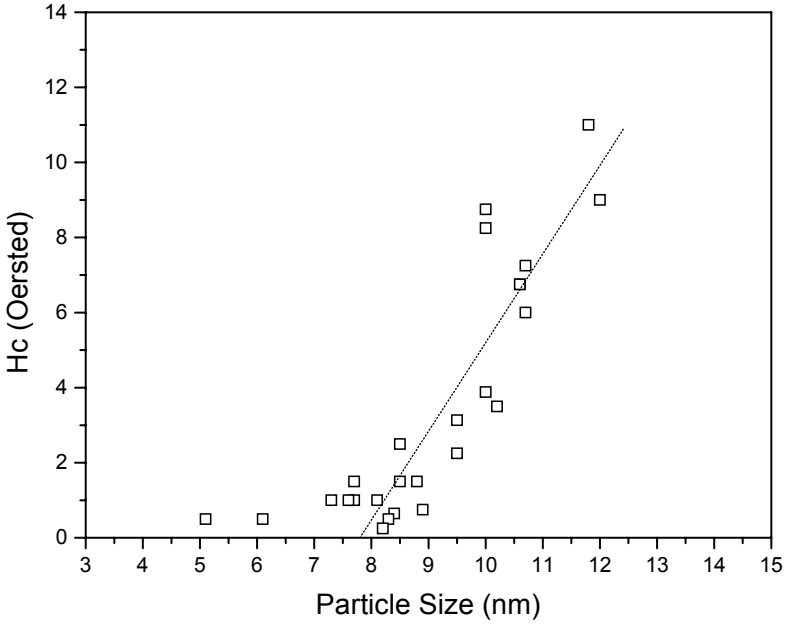

Figure 3-31. Plot of H_c vs. particle size (D_p).

Berkowitz *et al.* [58] suggested a model for the decrease in particle size and that model is applied and then expanded in this study to yield physical insight into the parameters. Power law relationship between M_s and inverse of the particle size was reported in that and other publications [23, 62], which is qualitatively similar to the Fe_3O_4 nanoparticle synthesized in this work. Figure 3-33 is a plot of $M_s^{1/3}$ vs. $1/R$ for the

synthesized Fe_3O_4 particles. The linear relationship between $M_s^{1/3}$ vs. $1/R$ is derived from a supposition that a magnetically dead, $M_s = 0$, layer exists around each particle (or near the particle surface). This layer does not contribute to the magnetic properties, but it does add to the overall mass of the particle. One assumes that R is the total radius of a particle, and it is composed of r and Δr, where r is the radius of the particle with $M_s > 0$ and Δr is the thickness of the magnetically dead layer with $M_s = 0$. Figure 3-32 illustrates the particle. One assumes that the magnetization is a volumetrically weighted average of $M_s > 0$ and $M_s = 0$ and starting with the following ratio:

$$M_{s,effective} = \frac{V_p(r)}{V_p(R)} \cdot M_{s,bulk} = \frac{(R-\Delta r)^3}{R^3} \cdot M_{s,bulk} \tag{3-14}$$

where $M_{s,effective}$ is the measured saturation magnetization for the particle and $M_{s,bulk}$ is the bulk saturation magnetization. Further simplification of Equation (3-14) results in the following:

$$M_{s,effective}^{1/3} = M_{s,bulk}^{1/3}\left[1-\frac{\Delta r}{R}\right] \tag{3-15}$$

Equation (15) represents a linear equation, $M_{s,effective}^{1/3}$ is plotted against 1/R, respectively. Notice that Δr, the thickness of the magnetically dead layer can be determined from the slopes while the bulk saturation can be calculated from the intercepts. Figure 3-33 shows the fitted plot of Equation (15). Table 3-11 reports the results of the linear fit of the equation and the calculated values of Δr and $M_{s,bulk}$.

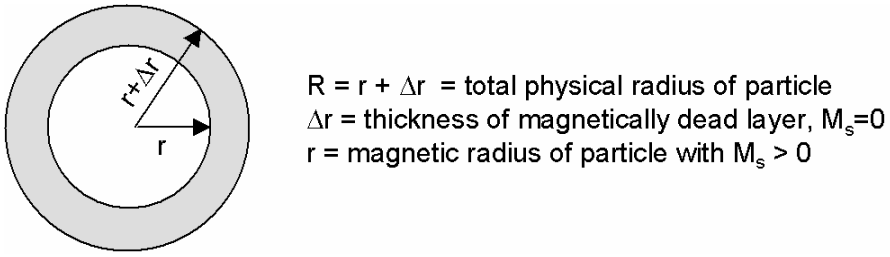

Figure 3-32. Illustration of a particle with a magnetically dead layer, *Δr*.

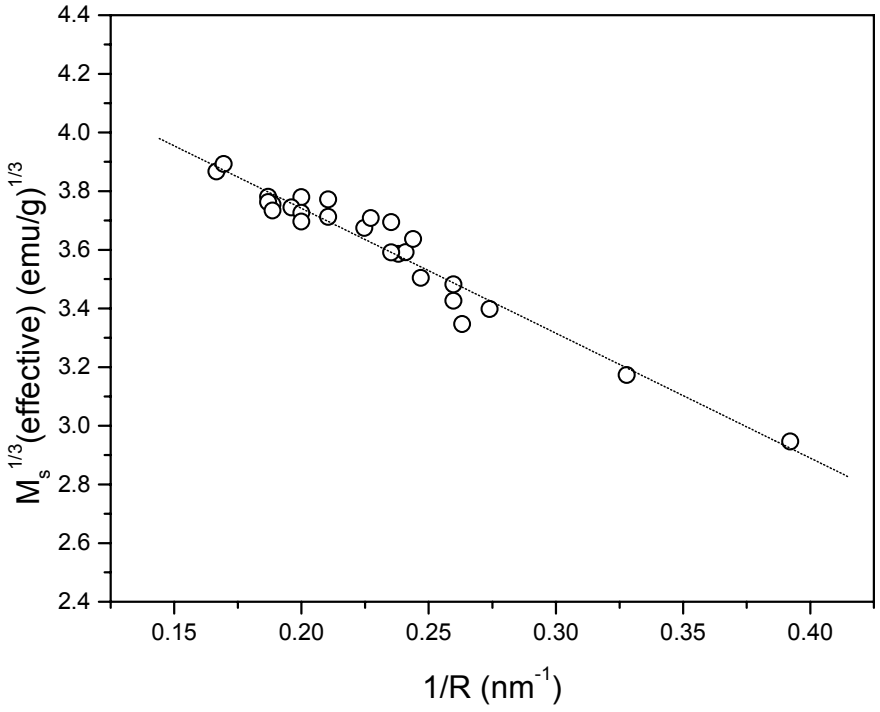

Figure 3-33. Plot of $M_{s,effective}^{1/3}$ vs. 1/R showing the power law relationships of magnetic properties with particle size.

The saturation magnetization calculated from Equation (3-15) is within the range of the reported bulk value (92-100 emu/g) [36]. The thickness of the magnetically dead layer from that equation is larger than those reported by other groups for magnetic

nanoparticles [23, 58]. Other groups used an approximation of Equation (3-14), using only the first two terms of the expansion. We obtained similar results for Δr as those groups when we used the approximated form of Equation (3-15). Since Equation (3-15) did not exclude higher order terms, one can expect the Δr and $M_{s,bulk}$ values from the fit of that equation to be more accurate than previously reported.

Table 3-11. Linear fit results for Equation (3-15).

	Slope	**Intercept**	**R-value**	**Δr (nm)**	**$M_{s,bulk}$ (emu/g)**
$M_{s,effective}^{1/3} = M_{s,bulk}^{1/3}\left[1-\frac{\Delta r}{R}\right]$	-4.26 $\pm$ 0.21	4.59 $\pm$ 0.05	-0.97	0.93	96.89

The reason for the presence of a magnetically dead layer has been assigned to spin canting, high anisotropy, and/or loss of long-range order on the surface [22, 23, 58-60]. Although a plethora of data has proven the existence of spin canting, it cannot be ruled out that noncoherent spins exist in the bulk [22, 23]. It is not a surprise that Δr is very close to the value of the lattice constant, a = 0.8394 nm [53], since the ions on the outer layer are most likely to be misaligned from the applied field resulting in an apparent decrease in saturation magnetization [22]. Future work in this topic should include direct measurements of the thickness of the magnetically dead layer and its correlation with particle size.

3.6.6 Nanoparticles to Bridge Molecular and Bulk Properties

The Fe_3O_4 nanoparticles produced here ranged from 5 nm to 12 nm in diameter. Size range scaling is to be expected and was analyzed quantitatively in the previous section. Particles of this size range contain approximately 200-3000 units of Fe_3O_4 and the scaling from bulk properties was reasonable. However, the question arises concerning the magnetic properties of even smaller particles, when $\Delta r/R$ approaches unity.

Particles 2 nm or less in diameter approach molecular scales and their behavior cannot be predicted using traditional theories. The lattice constant of Fe_3O_4 is 0.84 nm, so a particle that is less than 2 nm (<2.5 times the lattice constant) in diameter would behave differently even from 10 nm particles. The magnetic properties of particles that only consist of a few molecular clusters were predicted to be enhanced beyond that of bulk [47].

Landman and coworkers have modeled the magnetic properties of nanoclusters made of Fe_3O_4 and have predicted that such material would have saturation magnetization 3.5 times that of the bulk [47]. This opposes the trend observed in this study's measurements on nanoparticles with diameter of 5 to 12 nm. deHeer and coworkers took magnetic measurements of smaller particles and observed an upward trend that begins when the particle size is less than 3 nm [47]. Published data from other groups are also included in Figure 3-35, validating the magnetic properties data of the particles synthesized here [6, 60]. Particles with diameter greater than 3 nm exhibit a decrease in saturation magnetization with decreasing particle size. The particles synthesized in this study were made using the same process, chemical coprecipitation.

Previous concerns about the process route contributing to the variation in magnetic properties were minimized. It is valid to assume that the changes in magnetic properties are attributed only to differences in particle size.

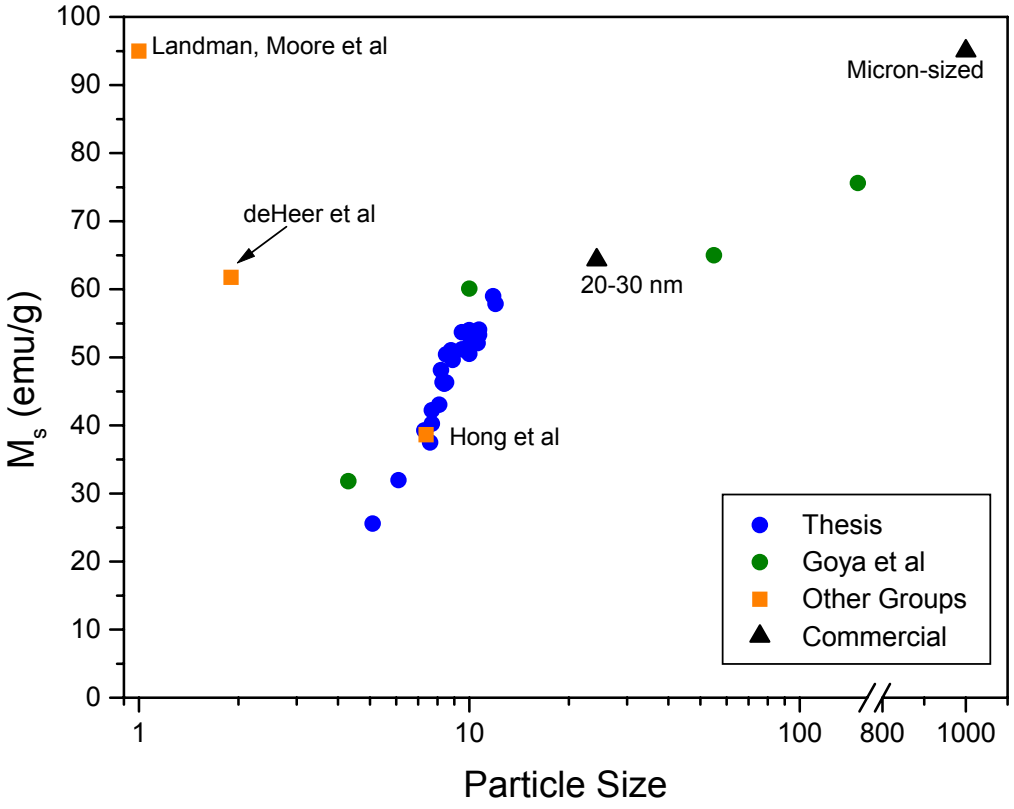

Figure 3-34. M_s vs. particle size of micron to ultra-nano particles.

3.7 Summary

Magnetite (Fe_3O_4) nanoparticles were synthesized using chemical coprecipitation. The main purpose of this work is to determine a process that would produce sufficient quantity of nanoparticles to be used as fillers for composites. Using a systematic experiment design, the process parameters that affect particle size were determined. The concentration of iron salt precursors was important, but as the concentration reached 1.8 M, its effect was not as significant. Other publications reported that increasing temperature would result in larger particles. This was observed, although its effect was mitigated when the pH level of the reaction solution was increased. When the ratio of iron salt concentration to base was 0.06, larger particles were produced. The ratio of ferric to ferrous salt affected particle size and morphology, and this was attributed to a difference in solubility of the salt in aqueous solution. For chloride salts, equal parts of ferric and ferrous ions yielded spherical particles. The type of iron salt also affected the particle size, since that modified the salt's solubility. The ionic strength of the solution was also investigated, where increased ionic strength generated smaller particle sizes.

After a wide size range of Fe_3O_4 nanoparticles were produced, the relationship between the magnetic properties and the particle size was measured and a model of M_s vs. particle diameter was developed. The measured linear relationship between H_c and particles was explained by theories of superparamagnetism. The critical particle size for onset of superparamagnetism was determined to be 7.75 nm for magnetite, and this is smaller than calculated values. The discrepancy can be explained by contributions of particle interactions and shape to the effective anisotropy constant. The measured linear

relationship of $M_s^{1/3}$ with the inverse of particle size was characterized and supported the theory of magnetically dead layer. The dead layer was found to be 0.93 nm, very close to the lattice constant of magnetite. The analysis conducted here is more accurate than previous studies because it did not approximate the weighted average relationship between M_s and particle size. The particles synthesized here helped to connect the bulk properties with nanoscale properties. Based on the results of this study, the process conditions that was selected to synthesize fillers for magnetic nanocomposites are the following:

Table 3-12. Process conditions for nanoparticles selected as fillers.

Sample No.	Total $[Fe^{z+}]$	$[OH^-]$	Temp.	$[Fe^{2+}]$ to $[Fe^{3+}]$	$[KNO_3]$	Particle Size (nm)	Fe^{3+} source	M_s (emu/g)	H_c (Oe)
19	1.8 M	0.5 M	65°C	1.0	0 M	11.8	$FeCl_3$	58.99	11
20	1.8 M	0.5 M	65°C	1.0	0.75 M	7.7	$FeCl_3$	42.22	1

3.8 References

[1] E. Matijevic and R. S. Sapieszko, "Forced Hydrolysis in Homogeneous Solutions," in *Fine Particles*, T. Sugimoto, Ed. New York: Marcel Dekker, Inc., 2000, pp. 2-34.

[2] P. Tartaj, M. del Puerto Morales, S. Veintemillas-Verdaguer, T. Gonzalez-Carreno, and C. J. Serna, "The preparation of magnetic nanoparticles for applications in biomedicine," *Journal of Physics D: Applied Physics*, vol. 36, pp. R182-R197, 2003.

[3] V. K. LaMer and R. H. Dinegar, "Theory, Production and Mechanism of Formation of Monodispersed Hydrosols," *Journal of the American Chemical Society*, vol. 72, pp. 4847-4854, 1950.

[4] R. Massart, "Preparation of Aqueous Magnetic Liquids in Alkaline And Acidic Media," *IEEE Transactions on Magnetics*, vol. 17, pp. 1247-1248, 1981.

[5] Y. S. Kang, S. Risbud, J. F. Rabolt, and P. Stroeve, "Synthesis and Characterization of Nanometer-Size Fe_3O_4 and γ–Fe_2O_3 Particles," *Chemistry of Materials*, vol. 8, pp. 2209-2211, 1996.

[6] S. H. Gee, Y. K. Hong, D. W. Erickson, M. H. Park, and J. C. Sur, "Synthesis and Aging Effect of Spherical Magnetite (Fe_3O_4) Nanoparticles for Biosensor Applications," *Journal of Applied Physics*, vol. 93, pp. 7560-7562, 2003.

[7] Y. Lee, J. Lee, C. J. Bae, J.-G. Park, H.-J. Noh, J.-H. Park, and T. Hyeon, "Large-Scale Synthesis of Uniform and Crystalline Magnetite Nanoparticles Using Reverse Micelles as Nanoreactors under Reflux Conditions," *Advanced Functional Materials*, vol. 15, pp. 503-509, 2005.

[8] Z. L. Liu, X. Wang, K. L. Yao, G. H. Du, Q. H. Lu, Z. H. Ding, J. Tao, Q. Ning, X. P. Luo, D. Y. Tian, and D. Xi, "Synthesis of Magnetite Nanoparticles in W/O Microemulsion," *Journal of Materials Science*, vol. 39, pp. 2633-2636, 2004.

[9] M. Mikhaylova, D. K. Kim, N. Bobrysheva, M. Osmolowsky, V. Semenov, T. Tsakalakos, and M. Muhammed, "Superparamagnetism of Magnetite Nanoparticles: Dependence on Surface Modification," *Langmuir*, vol. 20, pp. 2472-2477, 2004.

[10] C. R. Vestal and Z. J. Zhang, "Synthesis of $CoCrFeO_4$ Nanoparticles Using Microemulsion Methods and Size-Dependent Studies of Their Magnetic Properties," *Chemistry of Materials*, vol. 14, pp. 3817-3822, 2002.

[11] C. Liu, B. Zou, A. J. Rondinone, and Z. J. Zhang, "Reverse Micelle Synthesis and Characterization of Superparamagnetic $MnFe_2O_4$ Spinel Ferrite Nanocrystallites," *The Journal of Physical Chemistry B*, vol. 104, pp. 1141-1145, 2000.

[12] J. N. Park, K. An, Y. Hwang, J.-G. Park, H.-J. Noh, J.-Y. Kim, J.-H. Park, N.-M. Hwang, and T. Hyeon, "Ultra-large-scale syntheses of monodisperse nanocrystals," *Nature Materials*, vol. 3, pp. 381-385, 2004.

[13] S. Sun and H. Zeng, "Size-Controlled Synthesis of Magnetite Nanoparticles," *Journal of the American Chemical Society*, vol. 124, pp. 8204-8205, 2002.

[14] S. Sun, H. Zeng, D. B. Robinson, S. Raoux, P. M. Rice, S. X. Wang, and G. Li, "Monodisperse MFe2O4 (M = Fe, Co, Mn) Nanoparticles," *Journal of the American Chemical Society*, vol. 126, pp. 273-279, 2003.

[15] N. R. Jana, Y. Chen, and X. Peng, "Size- and Shape-Controlled Magnetic (Cr, Mn, Fe, Co, Ni) Oxide Nanocrystals via a Simple and General Approach," *Chemistry of Materials*, vol. 16, pp. 3931-3935, 2004.

[16] H. Zeng, P. M. Rice, S. X. Wang, and S. Sen, "Shape-Controlled Synthesis and Shape-Induced Texture of $MnFe_2O_4$ Nanoparticles," *Journal of the American Chemical Society*, vol. 126, pp. 11458-11459, 2004.

[17] I. W. Hamley, *Introduction to Soft Matter*. West Sussex: John Wiley and Sons, 2000.

[18] M. P. Pileni, "Reverse Micelles as Microreactors," *Journal of Physical Chemistry*, vol. 97, pp. 6961-6973, 1993.

[19] L. A. Welo and O. Baudisch, "The Two-Stage Transformaiton of Magnetite into Hematite," *Philosophical Magazine*, vol. 50, pp. 399-408, 1925.

[20] L. E. Slaten, "Precipitation of Dispersed Fine-Particle Magnetite," *Journal of Applied Physics*, vol. 31, pp. 74S-75S, 1960.

[21] R. Kaiser and G. Miskolczy, "Magnetic Properties of Stable Dispersions of Subdomain Magnetite Particles," *Journal of Applied Physics*, vol. 41, pp. 1064-1072, 1970.

[22] J. M. D. Coey, "Noncollinear Spin Arrangement in Ultrafine Ferrimagnetic Crystallites," *Physics Review Letters*, vol. 27, pp. 1140-1142, 1971.

[23] J. P. Chen, C. M. Sorensen, K. J. Klabunde, G. C. Hadjipanayis, E. Devlin, and A. Kostikas, "Size-dependent magnetic properties of $MnFe_2O_4$ fine particles synthesized by coprecipitation," *Physical Review B*, vol. 54, pp. 9288-9296, 1996.

[24] M. Ozaki, "Formation of Magnetic Particles," in *Fine Particles*, T. Sugimoto, Ed. New York: Marcel Dekker, Inc., 2000, pp. 662-682.

[25] Z. X. Tang, C. M. Sorensen, K. J. Klabunde, and G. C. Hadjipanayis, "Preparation of Manganese Ferrite Fine Particles from Aqueous Solution," *Journal of Colloid and Interface Science*, vol. 146, pp. 38-52, 1991.

[26] Z. J. Zhang, Z. L. Wang, B. C. Chakoumakos, and J. S. Yin, "Temperature Dependence of Cation Distribution of Oxidation State in Magnetic Mn-Fe Ferrite Nanocrystals," *Journal of the American Chemical Society*, vol. 120, pp. 1800-1804, 1998.

[27] S. Neveu, A. Bee, M. Robineau, and D. Talbot, "Size-Selective Chemical Synthesis of Tartrate Stabilized Cobalt Ferrite Ionic Magnetic Fluid," *Journal of Colloid and Interface Science*, vol. 255, pp. 293-298, 2002.

[28] Z. L. Liu, Y. J. Liu, K. L. Yao, Y. H. Ding, J. Tao, and X. Wang, "Synthesis and Magnetic Properties of Fe_3O_4 Nanoparticles," *Journal of Materials Synthesis and Processing*, vol. 10, pp. 83-87, 2002.

[29] D. K. Kim, M. Mikhaylova, Y. Zhang, and M. Muhammed, "Protective Coating of Superparamagnetic Iron Oxide Nanoparticles," *Chemistry of Materials*, vol. 15, pp. 1617-1627, 2003.

[30] T. Misawa, K. Hashimoto, and S. Shimodaira, "The Mechanism of Formation of Iron Oxide and Oxyhydroxides in Aqueous Solutions at Room Temperature," *Corrosion Science*, vol. 14, pp. 131-149, 1974.

[31] S. Music, S. Popovic, and M. Gotic, "Mossbauer Spectroscopy and X-ray Diffraction of Oxide Precipitate Formed from $FeSO_4$ Solution," *Journal of Materials Science*, vol. 25, pp. 3186-3190, 1990.

[32] R. Zao and P. Pan, "A Spectrophotometric Study of Fe(II)-Chloride Complexes in Aqueous Solutions from 10 to 100ºC," *Canadian Journal of Chemistry*, vol. 79, pp. 131-144, 2001.

[33] F. H. Sweeton and J. C. F. Baes, "The Solubility of Magnetite and Hydrolysis of Ferrous Ion in Aqueous Solutions at Elevated Temperatures," *Journal of Chemical Thermodynamics*, vol. 2, pp. 479-500, 1970.

[34] T. Sugimoto and E. Matijevic, "Formation of Uniform Spherical Magnetite Particles by Crystallization from Ferrous Hydroxide Gels," *Journal of Colloid and Interface Science*, vol. 74, pp. 227-243, 1980.

[35] J. Charles M. Flynn, "Hydrolysis of Inorganic Iron(III) Salts," *Chemical Reviews*, vol. 84, pp. 31-41, 1984.

[36] R. M. Cornell and U. Schwertmann, *The Iron Oxides*. Weinheim: VCH Verlagsgesellschaft, 1996.

[37] J.-E. Otterstedt and D. A. Brandredth, *Small Particles Technology*. New York: Plenum Press, 1998.

[38] K. T. Wu, P. C. Kuo, Y. D. Yao, and E. H. Tsai, "Magnetic and optical properties of Fe_3O_4 nanoparticle ferrofluids prepared by coprecipitation technique," *IEEE Transactions on Magnetics*, vol. 37, pp. 2651-2653, 2001.

[39] T. Misawa, K. Hashimoto, W. Suetaka, and S. Shimodaira, "Formation of $Fe(II)_1$-$Fe(III)_3$ Green Complex on Oxidation of Ferrous Ion in Perchloric Acid Solution," *Journal of Inorganic Nuclear Chemistry*, vol. 3, pp. 4159-4166, 1973.

[40] A. E. Regazzoni, G. A. Urrutia, M. A. Blesa, and A. J. G. Maroto, "Some Observations on the Composition and Morphology of Synthetic Magnetites Obtained by Different Routes," *Journal of Inorganic Nuclear Chemistry*, vol. 43, pp. 1489-1493, 1981.

[41] T. Fried, G. Shemer, and G. Markovich, "Ordered Two-Dimensional Arrays of Ferrite Nanoparticles," *Advanced Materials*, vol. 13, pp. 1158-1161, 2001.

[42] M. Ma, Y. Zhang, W. Yu, H.-Y. Shen, H.-Q. Zhang, and N. Gu, "Preparation and Characterization of Magnetite Nanoparticles Coated by Amino Silane," *Colloids and Surfaces, A: Physicochemical and Engineering Aspects*, vol. 212, pp. 21-226, 2003.

[43] Y. Zhu and Q. Wu, "Synthesis of Magnetite Nanoparticles by Precipitation with Forced Mixing," *Journal of Nanoparticle Research*, vol. 1, pp. 393-396, 1999.

[44] S. Qu, H. Yang, D. Ren, S. Kan, G. Zou, D. Li, and M. Li, "Magnetite Nanoparticles Prepared by Precipitation from Partially Reduced Ferric Chloride Aqueous Solutions," *Journal of Colloid and Interface Science*, vol. 215, pp. 190-192, 1999.

[45] C.-Y. Hong, I. J. Jang, H. E. Horng, C. J. Hsu, Y. D. Dao, and H. C. Yang, "Ordered structures in Fe_3O_4 kerosene-based ferrofluids," *Journal of Applied Physics*, vol. 81, pp. 4275-4277, 1997.

[46] L. Vayssieres, C. Chaneac, E. Tronc, and J. P. Jolivet, "Size tailoring of magnetite particles formed by aqueous precipitation: an example of thermodynamic stability of nanometric oxide particles," *Journal of Colloid and Interface Science*, vol. 205, pp. 205-212, 1998.

[47] "Science and Applications of MetaMaterials (SAMM), Final Technical Report," Georgia Tech Research Institute Contract Number F33615-01-C-5023, 24 October 2005.

[48] Z. L. Wang and Z. C. Kang, *Functional and Smart Materials: Structural Evolution and Structure Analysis*. New York: Plenum Press, 1998.

[49] B. D. Cullity, *Elements of X-Ray Diffraction*, 2nd ed. Reading: Addison-Wesley Publishing Co., 1978.

[50] B. D. Cullity, *Introduction to Magnetic Materials*. Reading: Addison-Wesley, 1972.

[51] H. P. Klug and L. E. Alexander, *X-Ray Diffraction Procedures for Polycrystalline and Amorphous Materials*. New York: John Wiley and Sons, 1954.

[52] K. Liu, L. Zhao, P. Klavins, F. E. Osterloh, and H. Hiramatsu, "Extrinsic Magnetoresistance in Magnetite Nanoparticles," *Journal of Applied Physics*, vol. 93, pp. 7951-7953, 2003.

[53] R. M. Cornell and U. Schwertmann, *The Iron Oxides*, 2nd ed. Weinheim: Wiley-VCH Verlag GmbH & Co., 2003.

[54] J. Smit and H. P. J. Wijn, *Ferrites*. Eindhoven: John Wiley and Sons, 1959.

[55] Y. Nakamura, M. Yamaguchi, A. Kitayama, M. Okubo, and T. Matsumoto, "Effect of Particle Size on Fracture Toughness of Epoxy Resin Filled with Angular-Shaped Silica," *Polymer*, vol. 32, pp. 2221-2229, 1991.

[56] W. F. Linke, *Solubilities, Inorganic and Metal-Organic Compounds; a Compilation of Solubility Data from the Periodical Literature*, Fourth ed. Princeton: Van Nostrand, 1958-1965.

[57] J. P. Jolivet, E. Tronc, and C. Chaneac, "Synthesis of Iron Oxide-Based Magnetic Nanomaterials and Composites," *C. R. Chimie*, vol. 5, pp. 659-664, 2002.

[58] A. E. Berkowitz, W. J. Schuele, and P. J. Flanders, "Influence of Crystallite Size on Magnetic Properties of Acicular γ-Fe_2O_3," *Journal of Applied Physics*, vol. 39, pp. 1261-1263, 1968.

[59] A. T. Ngo, P. Bonville, and M. P. Pileni, "Spin Canting and Size Effects in Nanoparticles of Nonstoichiometric Cobalt Ferrite," *Journal of Applied Physics*, vol. 89, pp. 3370-3376, 2001.

[60] G. F. Goya, T. S. Berquo, F. C. Fonseaca, and M. P. Morales, "Static and Dynamic Magnetic Properties of Spherical Magnetite Nanoparticles," *Journal of Applied Physics*, vol. 94, pp. 3520-3528, 2003.

[61] X. Batlle and A. Labarta, "Finite-Size Effects in Fine Particles: Magnetic and Transport Properties," *Journal of Physics D: Applied Physics*, vol. 35, pp. R15-R42, 2002.

[62] G. Rosa, H. Guerrero, D. Levy, A. Alvarez-Herrero, and R. P. del Real, "Surface Effects in Magnetic Nanoparticles Measured by Means of Magneto-Optical Method," *Journal of Applied Physics*, vol. 97, pp. 0643141-0643145, 2005.

CHAPTER 4

MAGNETIC AND MECHANICAL PROPERTIES OF Fe_3O_4 NANOCOMPOSITES

4.1 Introduction

The previous chapter described the synthesis of nanoparticles and measurements of their magnetic properties. This chapter will present the efforts performed during this project to fabricate and characterize nanocomposites using the nanoparticles synthesized in Chapter 3.

Fabricating composites with nanoparticles as fillers is challenging. Nanoparticles have a propensity to agglomerate into clusters and then settle out of their liquid medium, such as aqueous solution and uncured epoxy resin. Valid mechanical and electromagnetic data requires well-dispersed and isotropic composites. To produce a well-dispersed nanocomposite, the particles' surfaces must be modified to prevent them from agglomerating.

In this chapter a procedure for treating the surface of Fe_3O_4 nanoparticles with a surfactant, sodium dodecylbenzene sulfonate (NaDBS), was developed. NaDBS treatment resulted in improved dispersion of nanoparticles in the epoxy-based polymer matrix. Mechanical and electromagnetic properties of Fe_3O_4 nanocomposites with average filler sizes of 7 nm, 12 nm, and 25 nm were measured and compared with properties of composites containing micron-sized Fe_3O_4 fillers. In addition, the effects of volume fraction on electromagnetic and mechanical properties were evaluated. Electromagnetic properties of nanocomposites differed from micron-sized composites.

This is consistent with the size dependence of magnetic properties discussed in Chapter 3.

In the following section a background on surface chemistry of particles will be presented along with approaches for modifying their surfaces to improve dispersion. The selected approach for modifying surface of Fe_3O_4 nanoparticles will be discussed in that section. Details of experimental procedures (fabrication and characterization of composites) will follow and the remaining part of this chapter will present analysis of the measured mechanical and electromagnetic properties.

4.2 Background on Surface Chemistry and Surface Modification of Particles

When small particles are dispersed in a liquid medium, they are at a higher state of free energy than when they are agglomerated [1, 2], as shown in Figure 4-1. The free energy of interaction has contributions from van der Waals, electrostatic, and steric forces [1, 2]:

$$\Delta G = \Delta G^{att}(\text{van der Waals}) + \Delta G^{rep}(\text{electrostatic}) + \Delta G^{rep}(\text{steric}) \qquad (4\text{-}1)$$

where ΔG^{att} and ΔG^{rep} represent the energies of attractive and repulsive interactions, respectively. Unless there is a sufficient energy barrier to prevent it, the particles' tendency is to minimize their energy by flocculating together at small separation lengths. This energy barrier must be at least two to three times the value of kT (k is Boltzmann's constant and T is temperature) so that it cannot be overcome by thermal vibrations [1]. Equation (4-1) shows that stabilization of particles can be attained by increasing the repulsive energy components. Increasing the electrostatic and steric contributions is achieved through surface modifications.

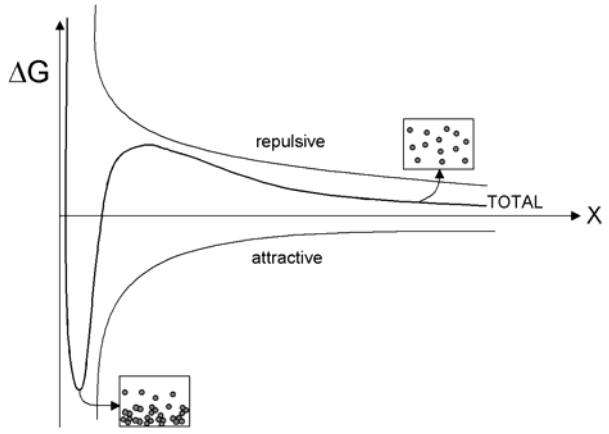

Figure 4-1. Total potential energy of interaction of dispersed and flocculated particles, reproduced from Otterstedt and Brandredth [1].

The surfaces of particles in aqueous solution are often described using the electrical double layer model [3]. The charges that characterize the surface of particles attract ions of the opposite charge from the surrounding solution. These ions (called counter-ions) form a diffuse layer around the particles and their concentration decreases with the distance from the surface of the particles. The region that is occupied by opposing net charges at and near the surface of the particles is called the electrical double layer (EDL), and is shown in Figure 4-2. This layer prevents the particles from flocculating. As they approach particles will experience electrostatic repulsion due to charges in the double layers, as described by the classical DLVO (Derjaguin-Landau-Verwey-Overbeek) theory [1, 4]. If enough force is provided when two particles collide breaking through the EDL, then they will coalesce and stability (dispersion) will be lost [1].

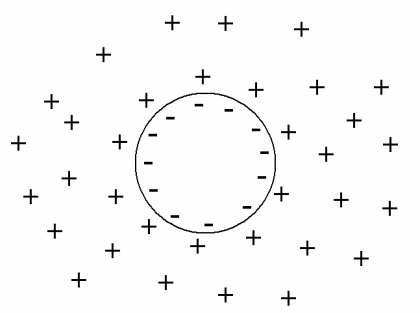

Figure 4-2. Schematic of the electrical double layer (EDL) surrounding a particle.

The electrical double layer can be described more specifically using the Stern layer and the Gouy-Chapman model [1, 3]. The ions that occupy the Stern layer are tightly bound to the surface of the particles by van der Waals and/or electrostatic forces [1]. A schematic of the Stern layer and Gouy-Chapman model is shown in Figure 4-3. The Gouy-Chapman model describes the diffuse layer of counter-ions that occupy the region beyond the Stern layer and where the surface potential decays exponentially with increasing distance away from particle surface. Within the Stern layer, the potential drop is more precipitous because the concentration of ions is greater. The change in potential within the electrical double layer is quantified by the following equation [1]:

$$\psi = \psi_o \exp(-\kappa x) \tag{4-2}$$

where ψ and ψ_o are the electrical potential at a distance x from the surface of the charged particle and at the surface of the charged particle (x = 0), respectively. κ is the Debye-Huckel parameter, and its inverse is called the Debye length and it is used to characterize the thickness of the EDL. κ is a function of temperature (T), ionic strength (I) and dielectric constant (ε) of solution medium, as shown in equation (4-3):

$$\kappa = \left(\frac{e^2 N_A I}{500 \varepsilon \varepsilon_o kT} \right)^{1/2} \tag{4-3}$$

where e is the electron charge, N_A is Avogadro's number, ε_o is the permittivity in vaccum, and k is Boltzmann's constant. The most effective means of varying κ is by changing the ionic strength of the solution.

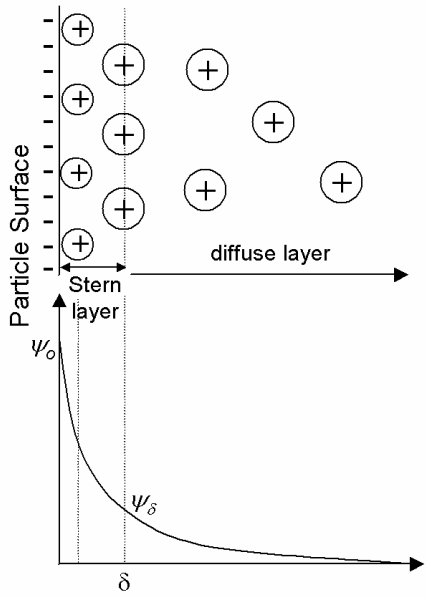

Figure 4-3. Gouy-Chapman model with Stern layer.

The zeta potential , ζ, is often used to approximate the the potential at the edge of the Stern layer, ψ_δ ,and it marks the beginning of the diffuse layer. Zeta potential is defined as the potential between the plane of shear around the particle and the medium surrounding the particle [3, 4]. This plane of shear is just beyond the Stern layer but still within the double layer. Since $\zeta \cong \psi_\delta$, it is an important parameter because it plays a big part in controlling the surface behavior of particles [3].

Electrostatic repulsion energy can be increased using counter-ions to build up the electrical double layer. This method is suitable for dispersing particles in aqueous solutions (medium) and in relatively low concentrations [4]. For dispersing particles in organic medium and/or high concentrations, steric stabilization using surfactants or polymers are more effective. The theories discussed thus far are still applicable for steric stabilization, especially the discussion on adsorbed entities within the Stern layer.

Surface modification of iron oxide particles using surfactants to increase the steric repulsion energy of the surfaces has been reported elsewhere and for various applications [5-11]. The use of oleic acid as surfactant has been very effective in stabilizing iron oxide particles in organic media. The presence of a carboxylic group on one end of the oleic acid structure can form a complex with the surface of the particles and the cis-double-bond midway along its chain allows for better solubility in hydrocarbon solvents [5, 10]. Other groups have also demonstrated success using tartaric and citric acids as stabilizing agents and their effectiveness can also be attributed to the carboxylic groups [6, 12]. Silane coupling agents are also able to complex with the surface of iron oxide particles through both chemisorption and physisorption [7]. Several publications reported the use of coating with polymer and/or silica to modify the particle surface [10, 13-15]. Such layer of coating will effectively shield the magnetic properties of the particles and increase the size of the particles [15].

Based on the encouraging results reported by other groups on steric stabilization of particles, a surfactant was selected to modify the surface of Fe_3O_4 nanoparticles. Sodium dodecylbenzenesulfonate (NaDBS) was the surfactant used in this study because it is readily available and this group of surfactants was proven effective in modifying the

surface of iron oxide particles [16]. NaDBS is one of the least expensive and more common ionic surfactants and more stable than other common anionic surfactants, such as sodium dodecyl sulfate, over a wide range of pH and at elevated temperatures [17]. Its chemical structure is shown below:

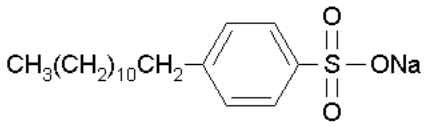

Figure 4-4. Chemical structure of NaDBS.

Surfactants are ampiphilic in nature, having both hydrophilic and hydrophobic groups within the same structure and thus they are soluble in organic and aqueous solvents [4]. The polar end of the surfactant will interact with the surface of the particle, while the hydrophobic tail is compatible with the organic medium, as shown in Figure 4-5. The driving force for adsorption of surfactants on particles can be attributed to the following interactions: electrical, lateral chain-chain, and chemical [3]. The total free energy of adsorption, $\Delta G^{o}_{(ads)}$ can be shown in the following equation:

$$\Delta G_{ads} = \Delta G^{o}_{elec} + \Delta G^{o}_{chem} + \Delta G^{o}_{C-C} + \Delta G^{o}_{H-H} + \Delta G^{o}_{C-S} + \Delta G^{o}_{solv} \qquad (4\text{-}4)$$

where ΔG^{o}_{elec} is due to electrical interaction, ΔG^{o}_{C-C} is the contribution of lateral chain-chain interaction , ΔG^{o}_{chem} is for chemical bonding. Other types of interactions that contribute to the total free energy include hydrogen bonding (ΔG^{o}_{H-H}), the interaction between hydrocarbon chains and non-polar solids (ΔG^{o}_{C-S}), and the interaction between surfactant and solvent/medium (ΔG^{o}_{solv}).

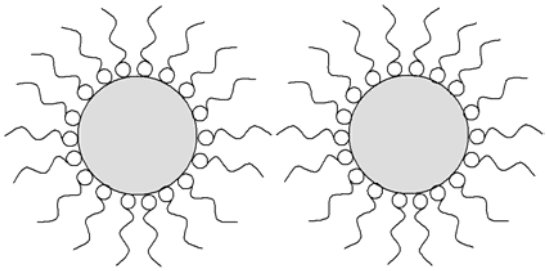

Figure 4-5. Schematic of steric stabilization of particles using adsorbed surfactants.

Electrical and chemical interactions play major roles in the adsoprtion of ionic surfactants on particle surface [3]. Ionic surfactants can be adsorbed by exchanging with counter-ions in the double layer and/or by direct electrostatic affinity between the charged surface of the particle and the polar end of the surfactant that has the opposite charge. Electrical interactions include Coulombic ($\Delta G^o_{(Coul)}$) and dipole ($\Delta G^o_{(dip)}$) free energy contributions:

$$\Delta G^o_{(elec)} = \Delta G^o_{(Coul)} + \Delta G^o_{(dip)} \tag{4-5}$$

As shown in the following scheme, the dipole contribution arises due to the replacement of adsorbed water by surfactant:

$$(\text{surfactant})_{\text{solution}} + n(H_2O)_{\text{adsorbed}} \rightarrow (\text{surfactant})_{\text{adsorbed}} + n(H_2O)_{\text{solution}} \tag{4-6}$$

$$\Delta G^o_{(dip)} = \sum \Delta_{nj} \mu_j E_s \tag{4-7}$$

where Δ_{nj} is the change in the number of adsorbed molecule j, μ_j is the dipole moment of j, and E_s is the field strength of the Stern plane. There is driving force for Coulombic adsorption as long as the zeta potential is positive for anionic surfactants (and negative for cationic surfactants), as shown in the following equation:

$$\Delta G^o_{(Coul)} = zF\psi_\delta \tag{4-8}$$

where z is the valency of the ionic surfactant, ψ_δ is the potential at the Stern plane but the zeta potential can be used in its place, and F is Faraday's constant.

Chemical interactions also play an important role especially for oxide particles [3]. Surfactants containing carboxylic, sulfonates, sulfates, hydroxylic, and amine groups are known for their chemisorption behavior. There is evidence of chemisorption when characteristic peaks of surfactants from infrared spectroscopy have shifted [3]. Chemical interactions can provide additional driving force for adsorption of surfactants. Furthermore, secondary bonds such as van der Waals and hydrogen bonding will also contribute to the adsorption of surfactants.

Since NaDBS is an anionic surfactant, its adsorption on the surface of Fe_3O_4 particles was facilitated when the particles' surface potential is positive, i.e. $\psi_\delta > 0$. The surface potential of metal oxides can be modified using H^+ and OH^-, as shown below [18].

$$M\text{-}OH + H^+ \rightarrow M\text{-}OH_2^+ \quad (4\text{-}9a)$$

$$M\text{-}OH + OH^- \rightarrow M\text{-}O^- + H_2O \quad (4\text{-}9b)$$

M is the metal and M-OH represents the hydroxyl group that is attached to the surface of metal oxide surfaces. Therefore, surface of Fe_3O_4 particles was made positive by placing the particles in an acidic environment, as in Equation (4-9a). With a positive surface potential, electrostatic interaction occurred between the surface of Fe_3O_4 particles and the polar end of NaDBS. This is shown in Figure 4-6. Once NaDBS molecules were near the surface of the particles, they could chemically interact with the surface of Fe_3O_4 particles, which is more robust than electrical interaction.

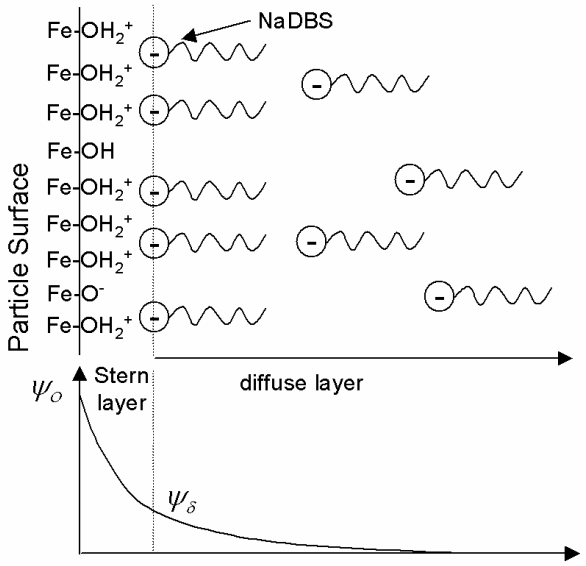

Figure 4-6. Schematic of adsorption of NaDBS on surface of iron oxide particle.

Once the Fe_3O_4 particles were treated in aqueous and acidic solution for adsorption of NaDBS, they were rinsed and then transferred to an organic solvent for dispersion in epoxy resin. Theoretically, the organic tails of adsorbed NaDBS molecules were exposed to the epoxy resin and the polar head was adsorbed on the particles's surface. In conjunction with mechanical agitation, i.e. sonicating bath, NaDBS treatment helped to disperse nanoparticles in epoxy resin.

4.3 Experimental Procedure

4.3.1 Surface treatment of nanoparticles with surfactant (NaDBS)

25nm Particles

Fe_3O_4 nanoparticles with an average diameter of 25nm were purchased from Aldrich (product # 637106). 2 g of nanoparticles were added into 250 mL of distilled water in a 500mL 3-neck flask and sonicated for 30 minutes. The slurry was placed under a nitrogen blanket and deoxygenated for at least 30 minutes. The pH of the slurry was adjusted to approximately 2.5 by adding 2M HCl solution and left to stir for another 60 minutes in inert atmosphere. 0.348 grams of NaDBS was added to the slurry. This amount produced a solution with a NaDBS concentration of $4x10^{-3}$ M, which is lower than the critical micelle concentration (CMC) for NaDBS ($5x10^{-3}$ M) [17]. It is known that surfactants assemble into ordered structures, i.e. spherical micelles, at concentrations near the CMC and higher [4], and this process competes with the adsorption of surfactants on particle surface. Therefore, a concentration less than the CMC was selected. The nanoparticles were left to stir in the solution for 20 to 24 hours under a nitrogen blanket.

To collect the particles, a permanent magnet was used to separate it from the solution and then it was decanted. Subsequently, the particles were rinsed with acetone twice and then with toluene twice. Approximately 50 mL of the solvent was used at each rinsing step. It was difficult to extract all of the toluene completely, and about 1 mL of toluene remained with the particles. The slurry of surfactant-treated particles was mixed with an epoxy formulation, and details of the procedure are in the following section. The toluene that remained with the particles was convenient since that allowed

for the surface-treated particles to disperse more easily in epoxy resin and toluene reduced the viscosity of epoxy resin.

7 nm and 12 nm Particles

Using the process conditions of Samples 19 and 20 as described in Table 3-35, 7nm and 12 nm particles were synthesized. After the final rinsing step, the particles were not filtered and dried as described in Chapter 3, but they were transferred to another 500 mL 3-neck flask containing 225 mL of distilled and deoxygenated water. The pH of the slurry was adjusted to approximately 2.5 using 2 M HCl solution, just as described for 25 nm particles. The mixture was stirred and deoxygenated for at least 60 minutes and then 0.314 grams of NaDBS was added. The mixture was stirred for 20-24 hours under a nitrogen blanket. The particles were collected following the same procedure as described for 25 nm particles.

4.3.2 Nanocomposites Formulation

The polymer matrix in the nanocomposites consists of bisphenol A – type epoxy resin (Epon 828 - Miller Stephenson), hexahydro-4-methylphthalic anhydride (HMPA) purchased from Aldrich as hardener, and triphenylphosphine (TPP) purchased from Fluka as curing agent (catalyst). Their chemical structures are shown in Figure 4-7. The formulation included 100 phr (per hundred parts of resin by weight) of Epon 828, 80 phr of HMPA, and 2.7 phr of TPP in the formulation. Toluene was also accounted for in the formulation at 6-10 wt% of the three essential components desribed previously.

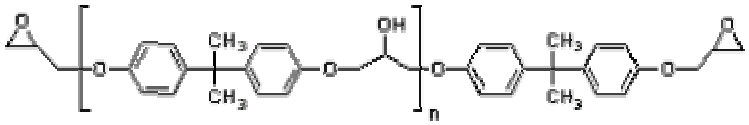

(a)

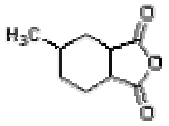

(b)

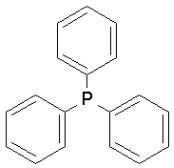

(c)

Figure 4-7. Chemical structures of (a) bisphenol A – type epoxy resin, (b) hexahydromethylphthalic anhydride and (c) triphenylphosphine.

4.3.3 Preparation of Nanocomposites

After the surfactant-treated nanoparticles were collected, HMPA and a stock blend of Epon 828 and TPP were added. For TPP to dissolve in epoxy resin it must be heated to approximately 60°C, therefore a stock blend of resin and curing agent was prepared separately. The mixture of polymer and nanoparticles was mixed using a high shear blade at 760 rpm for 10 minutes. The mixture was then sonicated for four hours. The sonicating bath helped to disperse the nanoparticles and remove any trapped air bubbles in the uncured nanocomposite blend.

The nanocomposite blend was poured into molds for curing. The curing behavior of the nanocomposites is affected by the presence of fillers, and the effect was amplified with smaller filler size. As the filler concentration was increased, longer curing times were required. Furthermore, when the particle size was reduced, the

requirement for longer curing times was observed at lower volume fraction. See discussion in Section 4.5.3.

4.4 Characterization Equipment and Procedures

The goal of the research was to fabricate and characterize nanocomposites with multifunctional properties. Satisfaction of the multifunctional approach requires data acquisition utilizing a plethora of experimental procedures and characterization equipment. This section will describe the equipment and procedures for characterizing chemical, mechanical, and magnetic properties of materials.

4.4.1 FTIR

A Fourier transform infrared (FTIR) spectrometer was used to analyze the surface of nanoparticles [3]. The equipment used was a Nicolet 4700 FT-IR made by Thermo Electron Corporation. To prepare the samples for FTIR measurement, a small amount of it was ground together with KBr and then pressed into a thin disk. The analysis was conducted at wavenumbers 400 to 4000 cm^{-1}, a resolution of 4 cm^{-1} and at transmission mode.

4.4.2 TGA

A thermal gravimetric analyzer (TGA) was used for observing weight loss due to decomposition of surfactant and evaporation of residual solvent. A TGA model Q50 by TA Instruments was used. A platinum sample pan was used, which permitted a maximum temperature of 1000°C. The purging gas was nitrogen and its flow rate was

set at 40 mL/min. The samples were analyzed at a heating rate of 10°C/min from 30°C to 900°C.

4.4.3 DSC

A differential scanning calorimeter (DSC) was used to determine the glass transition temperatures, heat of reactions, peak curing temperature, and onset reaction temperatures of polymer. The DSC Q100 by TA Instruments was used. The purging gas was nitrogen and the flow rate was set at 50 ml/min.

To measure the curing behavior, a sample weighing between 10 mg to 20 mg was placed inside an aluminum pan. The heating rate was set at 10°C/min from 30°C to 300°C. The sample was then cooled at a ramp rate of –10°C /min back to 30°C. During the heating cycle, the polymer is cured and curing parameters are measured. During the cooling stage, the glass transition temperature of the cured polymer is determined.

4.4.4 Mechanical Properties

A Microtester 5548 Instron Co. with a three-point bend fixture was used to measure the flexural properties and fracture behavior of the composites. The same fixture was used to measure two sets of mechanical properties, but with diffferent test parameters and specimens. American Society for Testing and Materials (ASTM) standards were used as guidelines: ASTM D5934 for flexural properties and ASTM D5045-99 for fracture toughness and energy.

To measure the flexural properties, three-point bend method was followed. The test specimens were approximately 30 mm in length, 1.5 mm in thickness, and 6 mm in

width. Each sample was placed in the test fixture as illustarated in Figure 4-8. Three to four specimens of each composite sample were measured to have some statistical validation. The rate of loading was controlled by setting the flexural extension at a rate of 1 mm/min. The test proceeded until the specimen failed and the applied load and extension of the specimen were recorded. The flexural modulus was calculated from the slope of the plot of applied pressure vs. strain. The strength was measured as the maximum applied pressure, before failure.

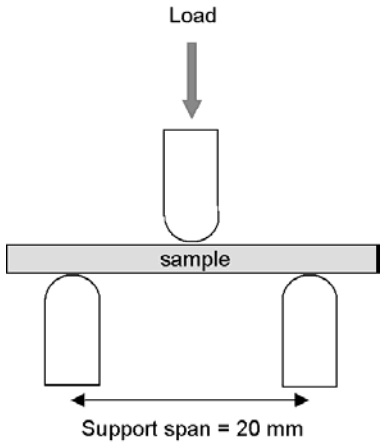

Figure 4-8. Schematic of test set-up for three point bend method, reproduced from ASTM D5934-02.

Fracture behavior was measured using the test set up illustrated in Figure 4-9. The test specimens were approximately 30 mm in length, 2mm in thickness, and 6 mm in width. The time-consuming part of this method is the specimen preparation. It required machining of a V-shaped notch in each specimen. The V-notch was machined using an end mill with a drill diameter of 0.7 mm. Subsequently, a sharp crack was initiated by tapping a sharp blade at the bottom of the machined notch, as illustrated in Figure 4-10. Three to five specimens of each composite sample were tested. The

geometry of the specimens met the required dimensions to meet the plane-strain conditions. Ratio of crack length to sample width (*a/W*) had to be between 0.45 and 0.55. The ratio of sample width to thickneness (*W/B*) was betweeen 2 and 4. The length of the support span was the same as in the three-point bend method, but the load was applied at a rate of 5 mm/min. The total length of the crack, *a*, was measured after the specimens were tested.

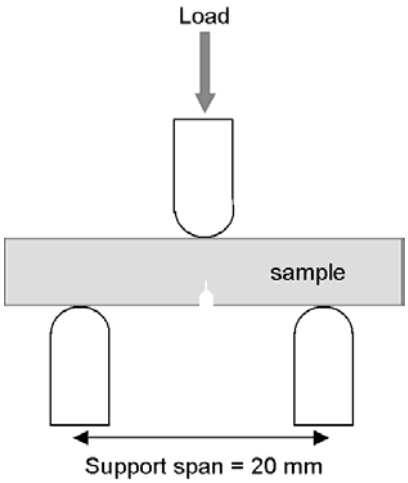

Figure 4-9. Schematic of test set-up for fracture measurements, reproduced from ASTM D5045-99

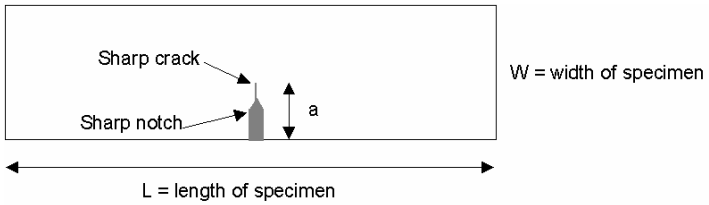

Figure 4-10. Schematic of single-edge notch bending (SENB) test specimen for fracture test.

The recorded data was load vs. displacement (extension). Fracture toughness was calculated using the following equation [19]:

$$K_Q = \frac{P_Q}{BW^{1/2}} f(x), \qquad x = a/W \tag{4-10}$$

where P_Q is the maximum load, B is the thickness of specimen, W is the width of specimen, a is crack length, and $f(x)$ is a function shown below.

$$f(x) = 6x^{1/2} \frac{\left[1.99 - x(1-x)(2.15 - 3.93x + 2.7x^2\right]}{(1+2x)(1-x)^{3/2}} \tag{4-11}$$

The geometric requirements were set, so $K_Q = K_{IC}$ for these tests. Furthermore, the fracture energy, G_{IC}, was calculated using the equation below:

$$G_{IC} = \frac{K_{IC}^2}{E} \tag{4-12}$$

where E is the elastic modulus. The flexural modulus was obtained using the three-point bend method as described previously. Elastic modulus was approximated assuming 70% of flexural modulus [19].

4.4.5 Permeameter

A permeameter designed and fabricated by the Signatures Technology Labratory at Georgia Tech Research Institute was used to measure the frequency dispersive permeability of the composites from 100 MHz to 8 GHz. The dimensions of the samples for this study were approximately 30 mm in length, between 2 to 3 mm in width, 0.2 to 0.5 mm in thickness. A schematic of the permemater is shown in Figure 4-11. The apparent complex permeability was calculated using the following equation [20]:

$$\mu_r^* = \frac{S_{11}^{sample} e^{2\gamma_0 L_2} + 1}{\gamma_0 L_1 \left(1 - S_{11}^{sample} e^{2\gamma_0 L_2}\right)} \tag{4-13a}$$

$$\mu_r^* = \mu_r' + i\mu_r'' \tag{4-13b}$$

where S_{11}^{sample} is the complex reflection coefficient collected from a network analyzer, $\gamma_o = 2\pi/\lambda_o$ is the free space propagation constant and λ_o is the electromagnetic wavelength in free space, L_1 is the width of the sample, and L_2 is the distance between the sample and the reference plane.

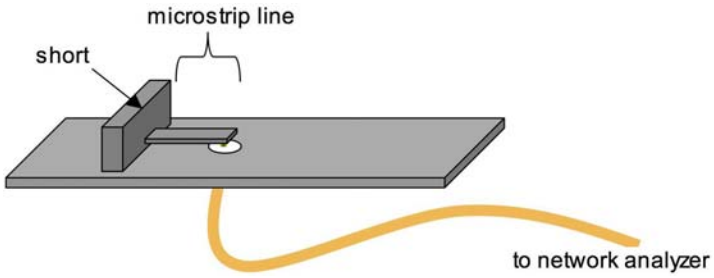

Figure 4-11. Schematic of permeameter, from Schultz [20].

This method provides accurate measurements for higher frequencies, from 100 MHz to 8 GHz. It requires additional data on permeability from a separate measurement in a lower frequency range, such as those collected using a low impedance analyzer, to calibrate the measurement and calculate the actual permeability.

4.4.6 TEM Sample Preparation Using Microtome

Cross sections of nanocomposites were prepared using a Leica Microtome Nova. The samples were first trimmed manually using a razor blade to produce a trapezoidal cross section with an area that was approximately 0.5mm x 0.5 mm. The samples were

then mounted on the microtome and aligned with a glass knife, which was used to trim the sample further. Each sample was trimmed until its surface is parallel to the glass. The glass knife was then replaced with a diamond knife, which was used make the final sections. At times, it was necessary to refine the alignment of the sample to the diamond knife at this time. The final thickness of the sections was between 30-60 nm and they were mounted on a copper TEM grid (200 mesh).

4.5 Results and Discussion

4.5.1 Characterization of the Polymer Matrix

An epoxy resin system was selected for the polymer matrix of (nano)composites. Its process conditions are easily adjusted with the choice of hardener, curing agent and their respective amount in the formulation. A bisphenol A type of epoxy resin with anhydride as hardener have been proven to be reliable [21], and was used in this study. Though a more common selection of curing agent are nitrogen containing compounds, such as amines and imidazoles, it was important to use a curing agent that did not react with the dopant used in the conductive polymer coating. Thus, triphenylphosphine (TPP), a phosphorous-containing curing agent, was selected.

The concentration of TPP in the formulation was determined by analyzing the curing behavior of samples as a function of the curing agent concentration. Toluene was also present in the nanocomposite formulation, so it is included in the analysis of epoxy formulations. Table 4-1 lists the different formulations and the results of those analyses. An optimum concentration of curing agent should not initiate curing too quickly since that can produce.a polymer with low crosslinking density and lower glass transition, T_g

[22]. Further, to facilitate cost-effective processing, the onset of cure and peak of cure temperatures should be less than 150°C. Based on these criteria, a TPP concentration of 1.5 wt% (Formulation 2) appeared promising. It yielded the highest Tg and its onset of cure and curing peak temperatures are less than 150°C.

The addition of toluene (Formulation 6) had minimal effect on the curing cycle requirements, but reduced the Tg. Toluene acts as a nonreactive diluent, and may have an adverse effect on properties of the cured epoxy [23]. However, a 10°C reduction in Tg is not significant since that still resulted in a Tg above 130°C. Therefore, TPP concentration of 1.5wt% was used and the toluene concentration did not exceed 15wt% in the nanocomposite formulation. Figure 4-12 shows the DSC scans of Formulations 2 and 6.

Table 4-1. List of epoxy formulations and the results of DSC analyses.

Epoxy Formulation Number	TPP Conc'n (wt%)	Toluene Conc'n (wt%)	Tg (°C)	Cure Peak (°C)	Cure Onset (°C)	Heat of Cure (J/g)
1	6	0	120.23	125.24	105.69	312.6
2	1.5	0	142.05	142.64	117.24	316.1
3	1	0	137.87	148.06	119.31	322.4
4	6	10	107.28	125.28	107.44	300.6
5	2	15	124.07	136.94	114.25	268.2
6	1.5	15	132.66	141.9	116.53	288.2
7	1	15	121.19	147.67	119.21	283.8

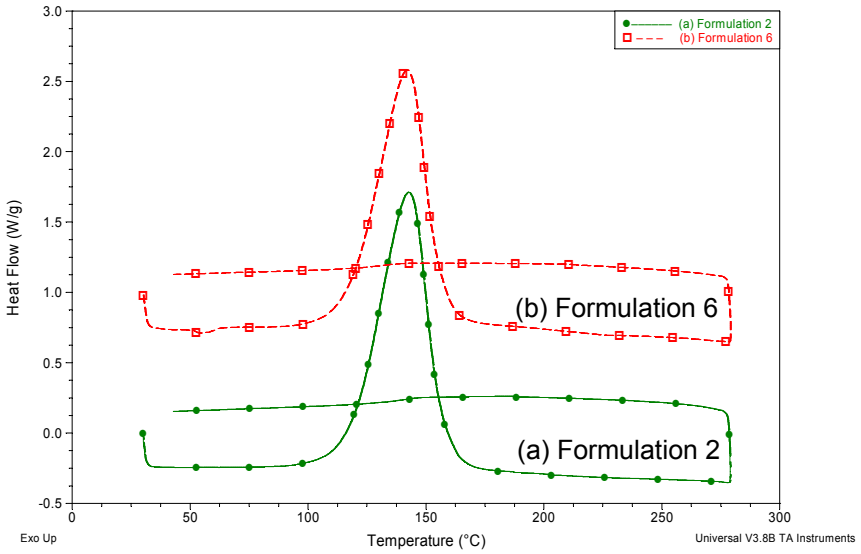

Figure 4-12. DSC scans of Epoxy Formulations (a) 2 and (b) 6.

4.5.2 Surface Treatment of Nanoparticles

The amount of NaDBS adsorbed on the surface of Fe_3O_4 nanoparticles was measured using TGA. Figure 4-13 shows the weight loss attributed to NaDBS being desorbed as the temperature was raised. The weight percentage of NaDBS was determined by taking the difference in weight between 150°C and 900°C, since any weight loss less than 150°C can be attributed to residual solvent. The amount of adsorbed NaDBS on 12 nm particles is greater than on 25 nm particles, as shown by the larger weight loss percentage observed in the TGA scan of 12 nm particles. Since the surface area of particles is inversely proportional to particle size, it is reasonable for more surfactant to be adsorbed on the surface of smaller particles.

Two decomposition temperatures were observed for both 25 nm and 12 nm particles, and they are summarized in Table 4-2. The first decomposition temperatures

are comparable to reported values [16]. The second decomposition temperature was attributed to chemisorbed surfactant. Both of the decomposition temperatures for 12 nm particles are higher, an indication that a greater percentage of the adsorbed NaDBS were chemisorbed on those particles.

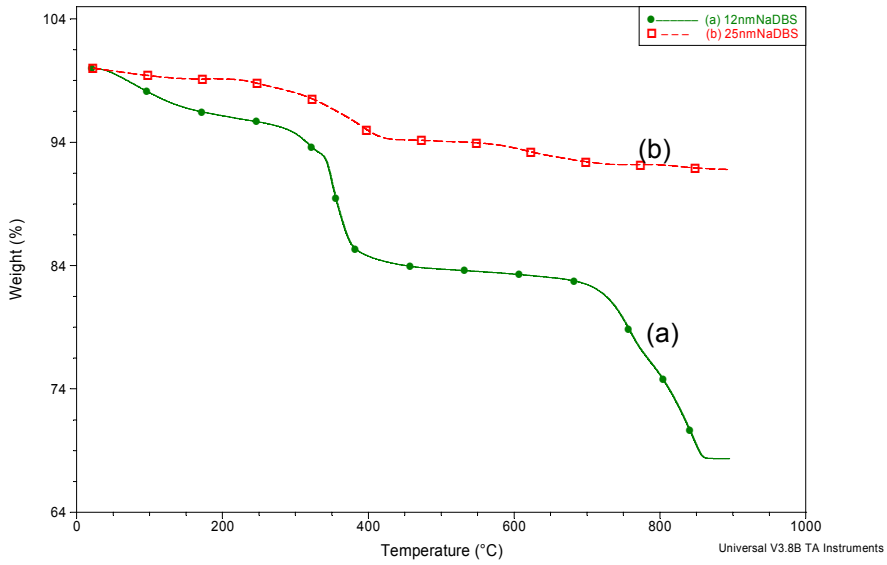

Figure 4-13. TGA of NaDBS-treated nanoparticles: (a) 12 nm and (b) 25 nm.

Table 4-2. Summary of TGA results of NaDBS-treated nanoparticles.

	Weight % NaDBS	Desorption Temperature (°C)
25 nm Fe_3O_4	7%	292°C 695°C
12 nm Fe_3O_4	29%	334°C 750°C

Adsorption of NaDBS on the surfaces of particles was also verified using FTIR. The FTIR spectra of NaDBS and 25nm particles were collected as a basis for comparison and they are shown in Figure 4-14. The set of characteristic peaks of NaDBS and magnetite are listed in the first two columns of Table 4-3. The third column lists the peaks that were observed in the spectrum of NaDBS-treated Fe_3O_4. The peaks that shifted were italicized. Figure 4-15 compares the spectrum of NaDBS-treated Fe_3O_4 with the control spectra in the wavenumber region of interest.

There are two characteristic peaks that shifted relative to the control spectra and they are from the Fe-O and SO_3-R stretching bands (see italicized peak location in Table 4-3) [16, 24]. The specific peaks that exhibited a shift after the surface of the particles was treated are listed in parentheses. A shift in peak location and/or shape is often caused by change in chemical bonding in the structure [3]. A condensation reaction between NaDBS and Fe-OH on the surface is one possible route for chemisorption, as shown in Figure 4-16. The chemisorption process should affect stretching/vibration of Fe-O and SO_3-R bonds and that is consistent with the peak shifts observed in the IR spectra.

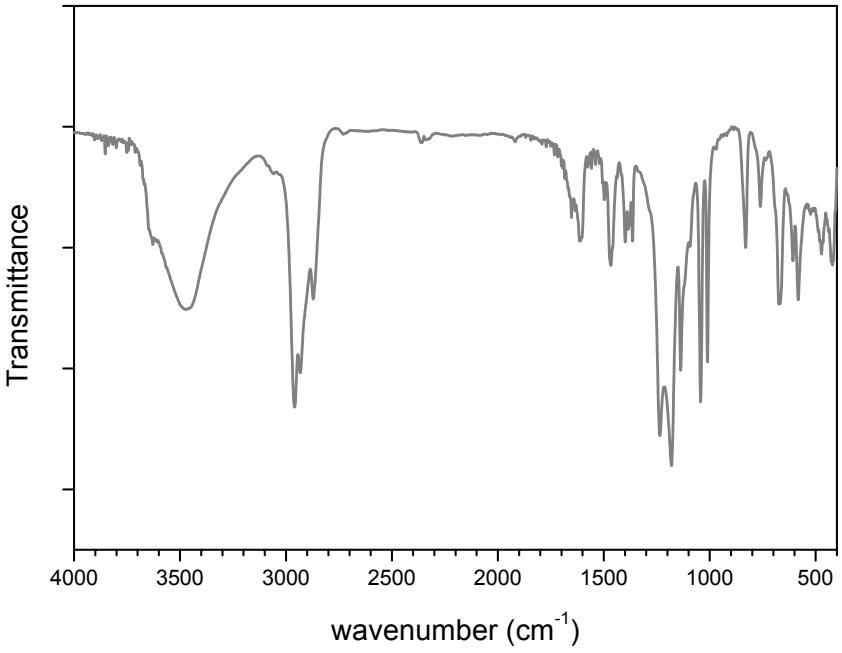

(a)

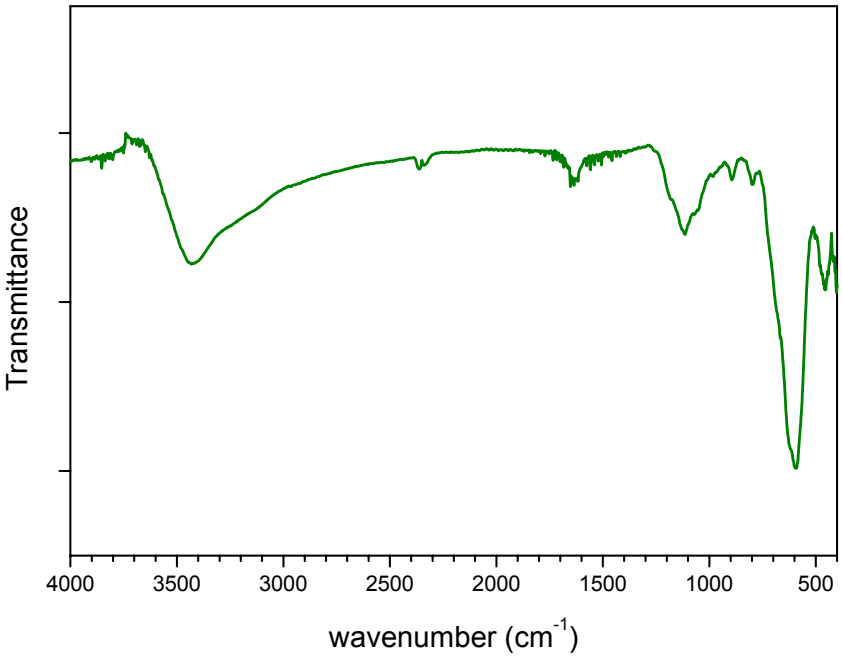

(b)

Figure 4-14. FTIR spectra of (a) NaDBS and (b) 25nm Fe_3O_4.

Table 4-3. Summary of FTIR characteristic peaks for 25nm particles, NaDBS, and NaDBS-treated 25nm particles.

25 nm Fe_3O_4	**NaDBS**	**NaDBS-treated 25 nm Fe_3O_4**	
400-600 cm^{-1} *(592 cm^{-1})*	--	400-600 cm^{-1} *(583 cm^{-1})*	Fe-O stretching [24]
	1000 – 1050 cm^{-1}	1000 – 1050 cm^{-1}	SO_3-R asymmetric stretching [16]
	1150 – 1250 cm^{-1} *(1180 cm^{-1})*	1150 – 1250 cm^{-1} *(1188 cm^{-1})*	SO_3-R symmetric stretching [16]
	1350 – 1800 cm^{-1}	1350 – 1800 cm^{-1}	CH_2 bending [16, 25]
	2870 – 3000 cm^{-1}	2870 – 3000 cm^{-1}	CH_2 stretching [16, 25]

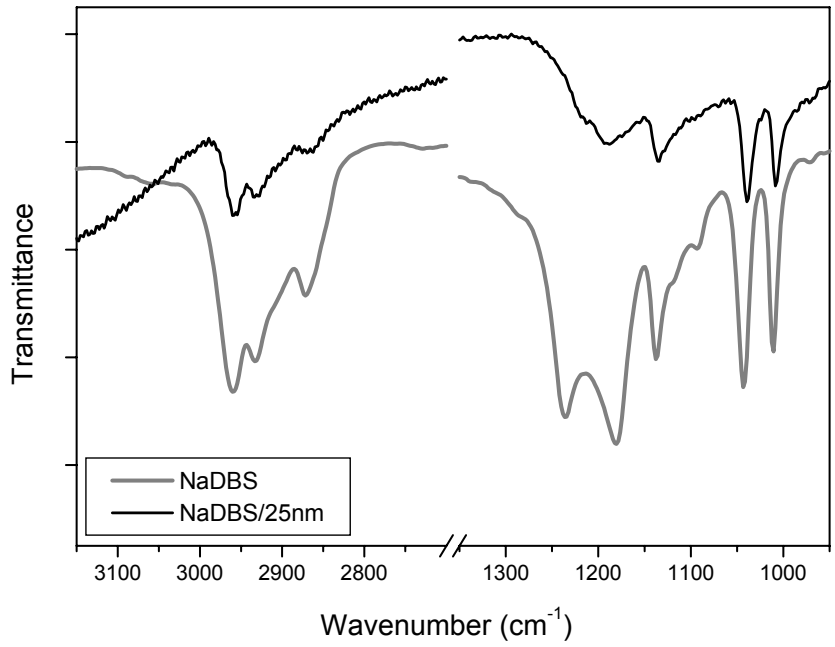

(a)

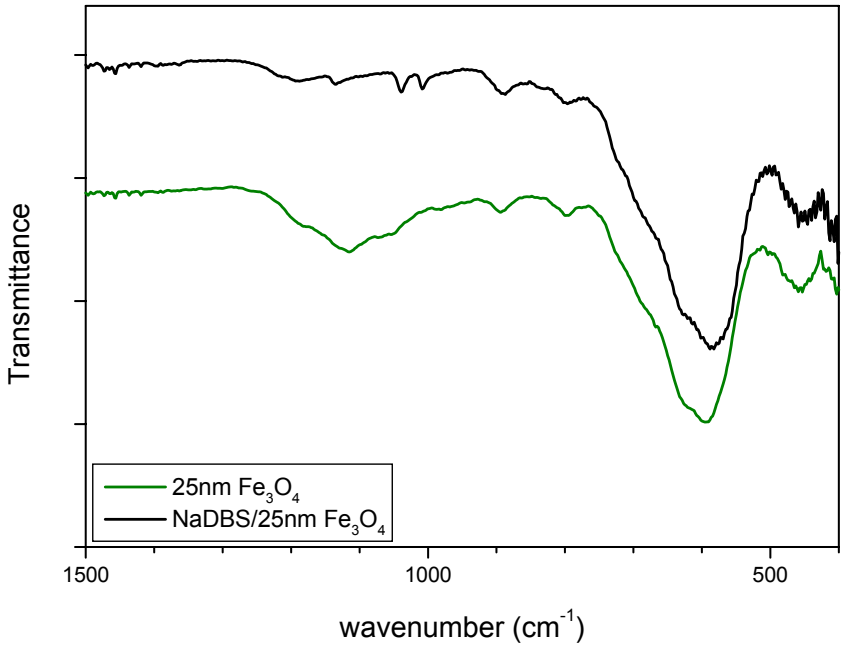

(b)

Figure 4-15. FTIR spectra comparing characteristic peaks of (a) NaDBS and NaDBS-treated 25nm Fe_3O_4 (b) 25nm Fe_3O_4 and NaDBS-treated 25nm Fe_3O_4.

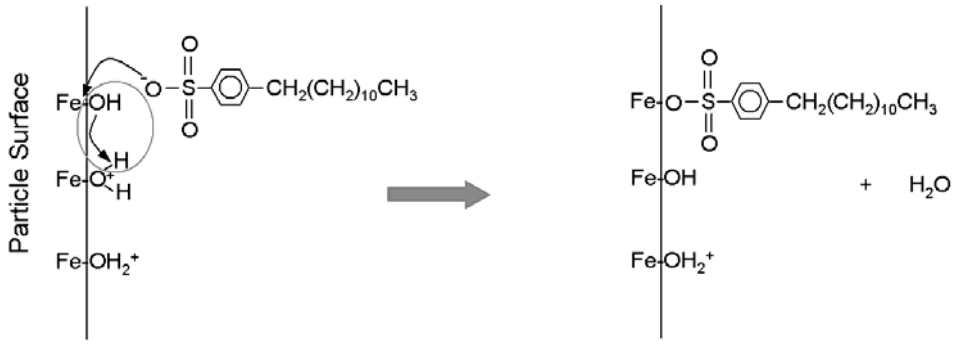

Figure 4-16. Proposed mechanism for chemisorption of NaDBS on surface of Fe_3O_4.

4.5.3 Nanocomposites

Dispersion and Curing

Effectiveness of NaDBS as dispersant was observed during the mixing of particles with the polymer matrix. The nanocomposite blend of surfactant-treated 25 nm particles was more homogeneous than its untreated counterpart. This was evident at the macroscale when a drop from each sample of uncured nanocomposite blends at V_f = 0.025 was spread across a glass slide, obvious formations of larger clusters and agglomerates were in the sample with untreated particles. Little to no change was observed even after the mixtures were mechanically dispersed using high shear mixer and sonicated for 4 hours. The nanocomposite blend with surfactant-treated particles appeared homogeneous and did not have any visible agglomerates.

The microstructures of cured nanocomposites containing surfactant-treated and untreated 25 nm nanoparticles were also compared. Using the same samples discussed in the previous paragraph, thin cross sections of each sample were prepared using a microtome. The cross sections were viewed in TEM and their images are shown in Figures 4-17 and 4-18. A cross section of surfactant-treated 12 nm nanocomposite at V_f

= 0.025 was also analyzed and it is shown in Figure 4-19. The untreated 25 nm nanocomposite in Figure 4-17 showed agglomerates with sizes of several to tens of microns. The particles in surfactant-treated 25 nm nanocomposite were more dispersed but still exhibited agglomeration/clustering. The microstructure of surfactant-treated 12 nm nanocomposite was even more dispersed compared to the 25 nm sample. One possible reason for this difference is that 12 nm particles were never extracted from a liquid medium completely and dried. The nanoparticles were always in some sort of liquid medium, albeit a small volume of liquid in some cases. The difference in degree of dispersion was applied to explain the differences in measured mechanical properties.

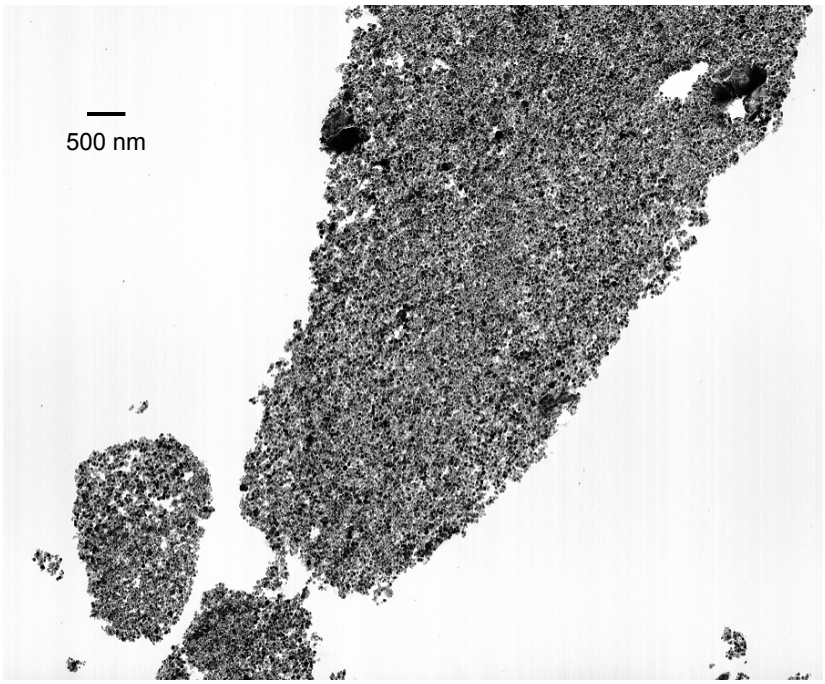

Figure 4-17. Cross section of untreated 25 nm nanocomposite at $V_f = 0.025$.

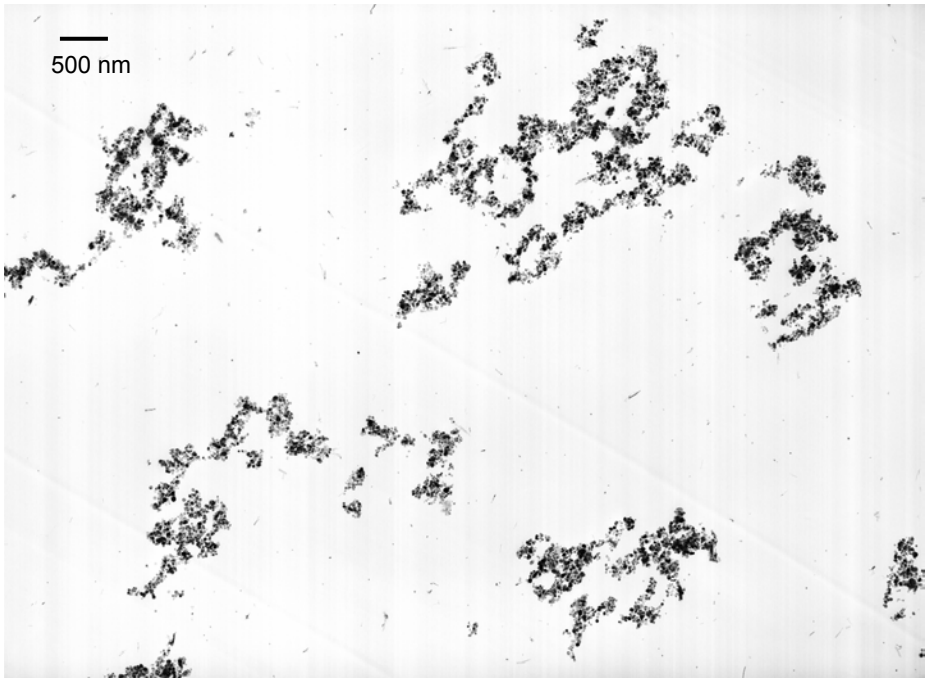

Figure 4-18. Cross section of surfactant-treated 25 nm nanocomposite at $V_f = 0.025$.

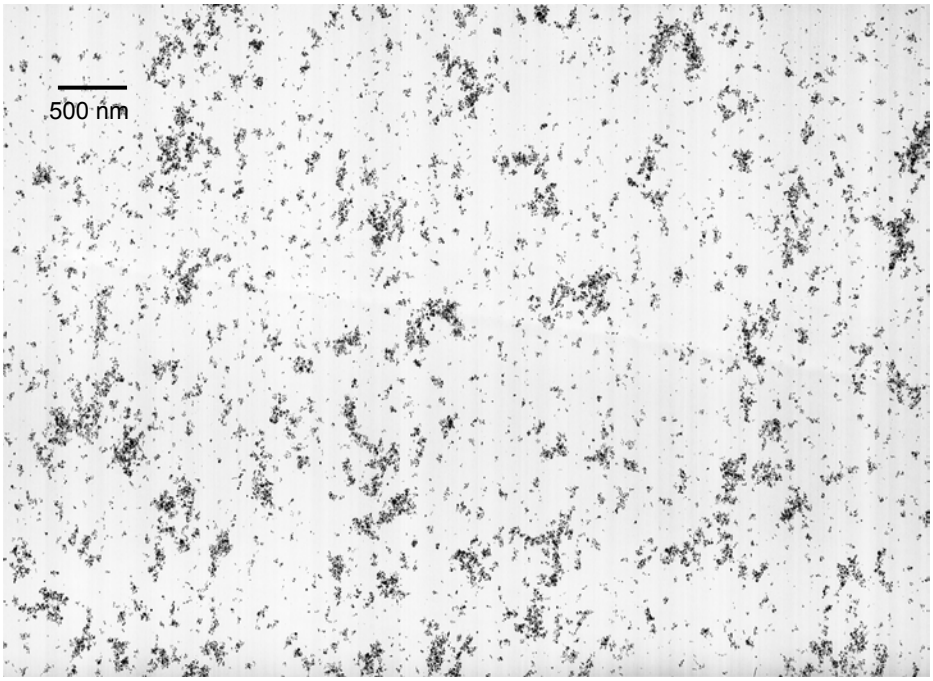

Figure 4-19. Cross section of surfactant-treated 12 nm nanocomposite at $V_f = 0.025$.

One of the goals of this research was to prepare nanocomposites at high filler loading, volume fraction greater than 5%. However, the preparation of nanocomposites with high filler loading proved to be challenging. For example, when 7nm fillers at V_f = 0.025 were used, the resulting composite was extremely brittle and it was decided that the volume fraction would be restricted to V_f = 0.002 to 0.0125. Similar observations were made for nanocomposites with 12 nm fillers, so the maximum volume fraction for that set of samples is 0.025. For 25 nm fillers, samples as high as V_f = 0.10 were successfully fabricated.

The curing process was found to be dependent on the size and concentration of nano-sized filler. As the filler loading increased, a longer cure schedule was required. Table 4-4 lists the cure schedules of the different composite samples and data from DSC analyses. Unfilled samples and those with lower filler loading were cured after two hours at 100°C. However, Sample C4 (25 nm fillers, V_f = 0.05) was still soft after two hours at 100°C, therefore another hour was added to its cure schedule at 100°C. Extending the curing cycle was necessary at lower volume fractions for smaller particle size, e.g. Sample C10 (V_f = 0.025 , 12 nm particles) and Sample C13 (V_f = 0.0125, 7 nm particles) were kept at 100°C for 4 hours before they hardened.

Figure 4-20 shows that the nanocomposites' exothermic peaks from their curing profile are broader than their micron-sized counter parts. The curing profile of Samples C6 (V_f = 0.10, 25 nm) and C10 (V_f = 0.025, 12 nm) illustrates that their curing exotherms are broad, and curing initiated at lower temperatures but completed at higher temperatures. The curing profiles of these samples also show the possibility of two overlapping peaks. Therefore, two modes of curing mechanism must be considered.

Adsorbed surfactants on the surface of nanoparticles coupled with increased interfacial area between filler and epoxy may have altered the curing reaction. Based on the curing data, we propose that hydroxyl group on the surface of the nanoparticles can catalyze the curing reaction. It is well established that pendant hydroxyl groups can react with anhydride and initiate curing [26]. Surface of nanoparticles that did not have adsorbed surfactant have exposed hydroxyl groups that may initiate curing reaction at the lower temperature. At the same time, the dispersed nanoparticles (12 nm and 7 nm) are small enough that they may act as impurities and impede curing in epoxy, as shown by the delayed completion of curing in Figure 4-20 of 12 nm composite. Furthermore, adsorbed NaDBS can interact with epoxy and can have a plasticizing effect. In contrast, the curing of composites with micron-sized fillers was not affected by the volume fraction, as shown by the relatively constant curing parameters from Table 4-4 of Samples C14-C18.

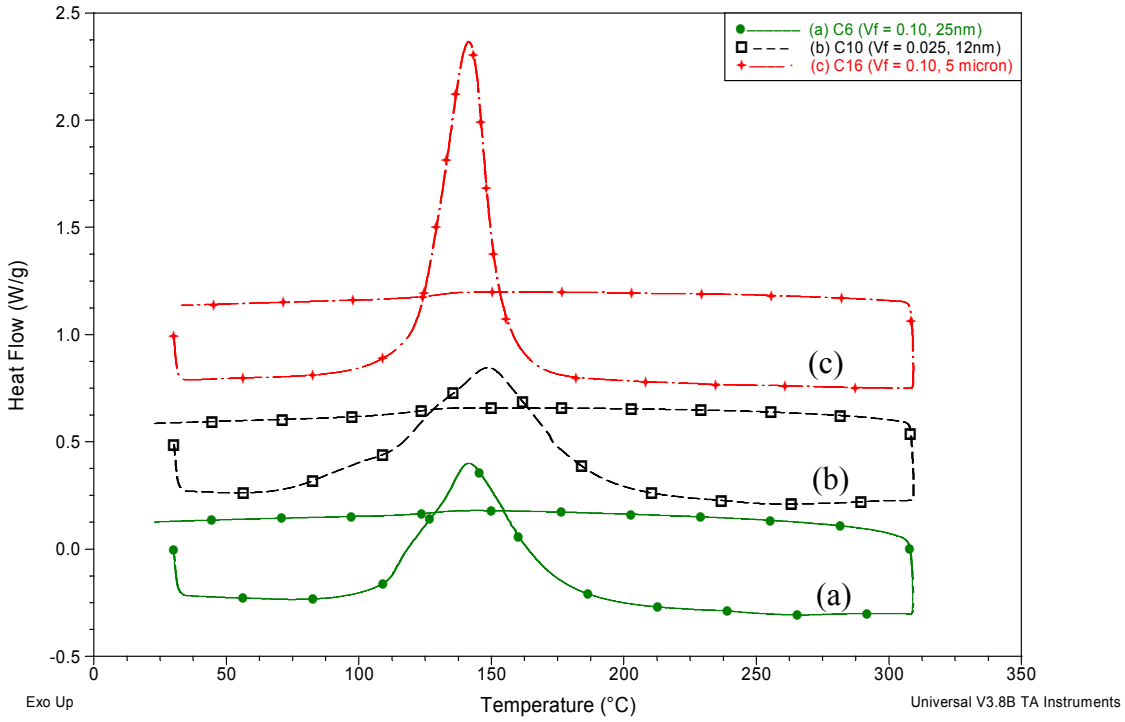

Figure 4-20. Curing behavior of composite Samples (a) C6, (b) C10, and (c) C16.

Table 4-4. Cure schedule and thermal analyses data of fabricated composites.

Sample			Cure Schedule		Thermal Analyses (DSC)			
ID	Particle Size	Vf	100°C	140°C	Tg °C	Cure Peak °C	Cure Onset °C	Heat of Cure (J/g)
C0	--	0	2 hrs	1 hr	142.05	142.64	117.24	316.1
C1	--	0	2 hrs	1 hr	132.66	141.90	116.53	288.2
C2	25 nm	0.013	2 hrs	1 hr	110.59	142.00	119.10	250.6
C3		0.025	2 hrs	1 hr	122.19	147.94	111.03	204.7
C4		0.050	3 hrs	1 hr	108.17	154.57	109.42	212.7
C5		0.075	3 hrs	1 hr	117.38	144.55	101.72	171.7
C6		0.010	3 hrs	1 hr	130.04	141.63	107.35	169.9
C7	12 nm	0.002	2 hrs	1 hr	132.26	148.30	126.60	310.0
C8		0.006	2 hrs	1 hr	126.14	148.21	124.47	300.7
C9		0.013	2 hrs	1 hr	121.34	147.83	116.19	264.9
C10		0.025	4 hrs	2 hrs*	123.83	149.23	70.68	218.7
C11	7 nm	0.002	2 hrs	1 hr	135.11	141.75	121.82	305.5
C12		0.006	2 hrs	1 hr	115.33	145.70	111.47	232.9
C13		0.013	4 hrs	2 hrs	111.43	148.84	99.91	107.8
C14	~ 5 μm	0.025	2 hrs	1 hr	137.25	142.98	119.38	291.7
C15		0.050	2 hrs	1 hr	134.25	143.14	120.01	255.5
C16		0.100	2 hrs	1 hr	130.75	141.40	117.96	223.7
C17		0.150	2 hrs	1 hr	107.23	139.92	114.35	162.21
C18		0.200	2 hrs	1 hr	111.42	141.85	119.96	131.5

*additional hour at 160°C

Mechanical properties

This section presents the measured mechanical properties of nanocomposites as functions of filler content and filler size. The trends of their properties were compared to composites containing micron-sized fillers. Flexural modulus and strength of the composites were measured using the three-point bend method. The fracture toughness of the fabricated samples was measured using a three-point bend fixture and single-edge-notch bending (SENB) specimen geometry. Data from these two sets of tests are summarized in Table 4-5. The data are also presented graphically in Figures 4-21 to 4-28. Properties of micron-sized and 25 nm composites are presented in one group, since they tend to show similar trends. Data of 12 nm and 7nm composites are grouped together.

Table 4-5. Mechanical properties of fabricated nanocomposites.

Sample			Mechanical Properties			
ID	Particle Size	Vf	Flexural Modulus (MPa)	Flexural Strength(MPa)	K_{1c} (MPa·m$^{1/2}$)	G_{Ic} (J/m^2)
C1			2958.38 ± 58.07	140.72 ± 3.40	0.355 ± 0.027	60.8
C2	25nm	0.013	2953.41 ± 126.34	138.98 ± 3.81	0.318 ± 0.041	48.8
C3		0.025	3149.03 ± 71.86	102.97 ± 0.86	0.324 ± 0.127	47.7
C4		0.050	3327.93 ± 76.57	93.75 ± 2.40	0.552 ± 0.086	131
C5		0.075	3600.63 ± 74.75	36.62 ± 3.10	0.331 ± 0.042	43.4
C6		0.010	3967.28 ± 23.78	61.71 ± 3.30	0.350 ± 0.112	44.0
C7	12nm	0.002	2817.24 ± 40.48	131.00 ± 1.19	0.339 ± 0.044	58.2
C8		0.006	2771.06 ± 410.09	121.91 ± 8.79	0.325 ± 0.094	54.5
C9		0.013	3089.25 ± 45.16	113.43 ± 1.32	0.361 ± 0.101	60.2
C10		0.025	2499.02 ± 110.06	28.87 ± 6.76	0.972 ± 0.057	540
C11	7nm	0.002	2864.95 ± 26.92	129.00 ± 0.99	0.289 ± 0.017	41.6
C12		0.006	3046.62 ± 30.70	105.91 ± 0.98	0.497 ± 0.084	116
C13		0.013	1086.04 ± 67.34	28.72 ± 2.22	0.845 ± 0.098	938
C14	~ 5 μm	0.025	3084.06 ± 58.07	131.95 ± 10.37	0.539 ± 0.019	135
C15		0.050	3386.60 ± 58.07	108.04 ± 19.37	0.488 ± 0.117	101
C16		0.100	3965.18 ± 58.07	82.40 ± 26.75	0.505 ± 0.190	91.8
C17		0.150	4717.23 ± 58.07	83.35 ± 32.02	0.412 ± 0.144	52
C18		0.200	5424.51 ± 58.07	96.43 ± 9.02	0.467 ± n/a	58

The modulus of ~5μm composites displayed the expected behavior of increasing linearly with volume fraction when $V_f \leq 0.30$ [27]. Nanocomposites fabricated using 25 nm fillers show the same trend and their data closely align with those of ~5μm composites. Their data are plotted in Figure 4-21. However, nanocomposites with 12 nm and 7nm fillers exhibited unexpected trends, where a modulus drop was observed at higher filler loading. Figure 4-22 shows that modest improvements in modulus were made at $V_f = 0.006$, and then a significant reduction at $V_f = 0.0125$ and $V_f = 0.025$ for 7 nm and 12 nm nanocomposites, respectively. These samples also have unusual curing behavior, which was discussed earlier.

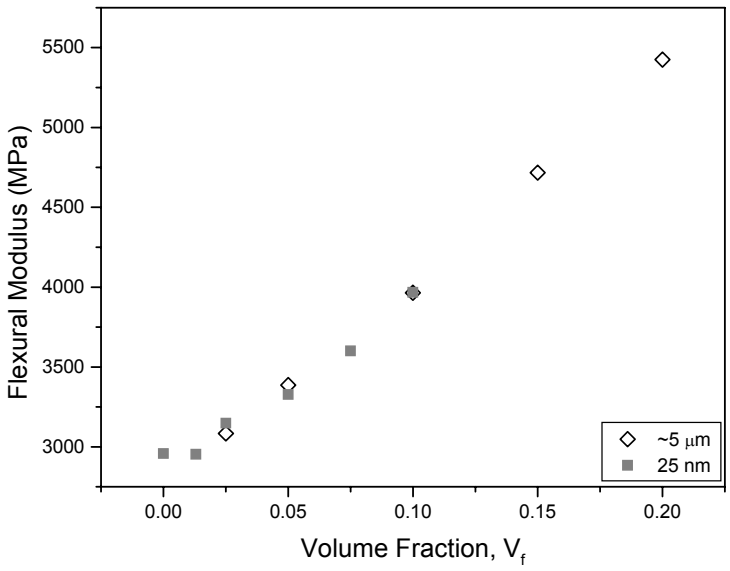

Figure 4-21. Flexural modulus of ~5μm and 25nm composites.

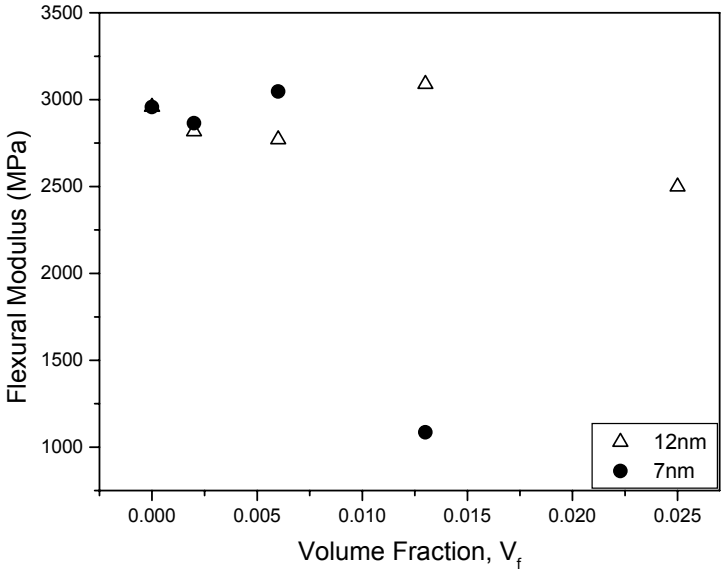

Figure 4-22. Flexural modulus of 12nm and 7nm composites.

The flexural strengths of ~5μm and 25 nm composites did not align together as with the modulus data but showed similar trends. As shown in Figure 4-23, the strengths of both sets of composites decreased with increasing volume fraction. The decrease in strength with filler content suggests that the bonding between particles and matrix are weak points [27]. If the bonding between filler and matrix were poor, the strength would continue to decrease with filler loading. When there is good adhesion between matrix and fillers, the strength decreases minimally with filler loading and/or recovers from the decrease. There is evidence of good bonding between micron-sized Fe_3O_4 particles and the matrix since there is an indication of recovery in strength when $V_f > 0.10$. A large drop in strength was observed for Sample C5 ($V_f = 0.075$, 25nm), but subsequent analysis indicated that the drop may be caused by excessive voids present in that sample. Overall, 25 nm composites had lower strength than their ~5μm

counterparts, probably due to greater interfacial area between filler and matrix. The interfacial areas represent weakness point in the structure. Unfortunately 25 nm composite samples at higher volume fraction were not available for measurements. Therefore recovery of strength, an indication of good bonding between fillers and matrix, could not be verified for 25 nm composites.

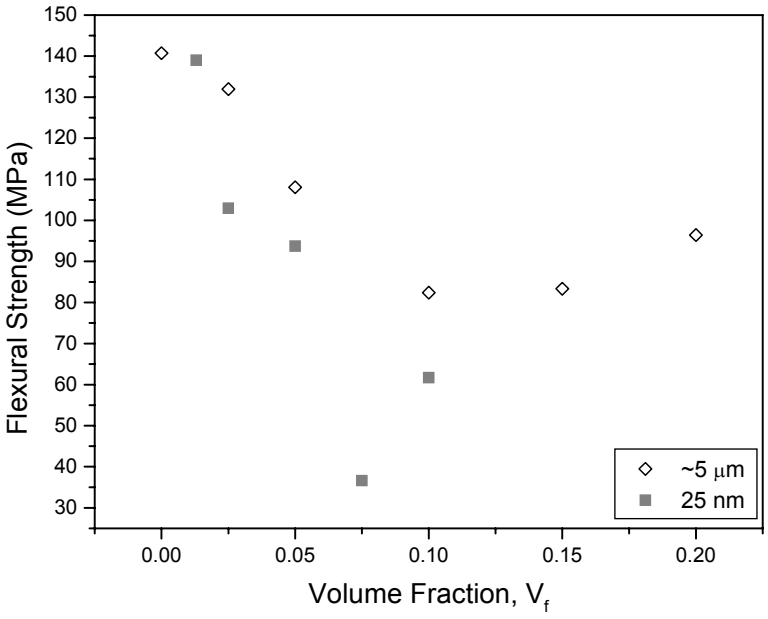

Figure 4-23. Flexural strength of ~5μm and 25nm composites.

Flexural strengths of 12 nm and 7 nm composites are plotted in Figure 4-24. The drop in strength with filler content is more precipitous in smaller filler size. The drop in strength is clearly illustrated by the data of Samples C10 (V_f = 0.025, 12 nm) and C13 (V_f = 0.0125, 7nm). Particles at this size scale have 200-700 times the polymer-filler interfacial area than micron-sized fillers. It is reasonable to observe the additional reduction in strength for composites with 12 nm and 7nm fillers. Using the same

reasoning, the mechanical properties of 25 nm composites should resemble the properties of 12nm and 7nm composites, but as discussed earlier they were more comparable to the properties of micron-sized composites.

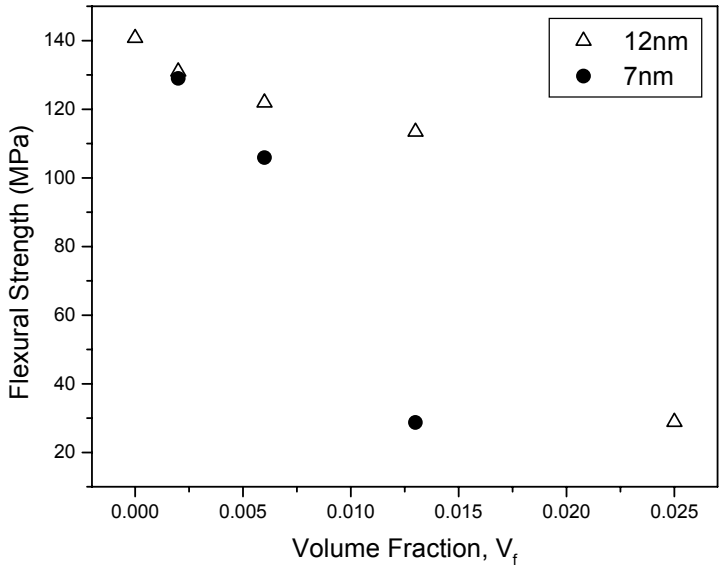

Figure 4-24. Flexural strength of 12nm and 7nm composites.

Recall that the amount of adsorbed surfactants on 12 nm particles was significantly greater than for 25 nm particles (see Figure 4-13 and Table 4-2). The difference can be partially attributed to increasing surface area with decreasing particle size, but another reason may be due to processing. 25 nm particles were purchased as dried particles and were resuspended in solution before surface treatment. In contrast, 12 nm and 7 nm samples were synthesized and then treated with surfactant; there was not a discrete step where the particles were completely extracted and dried from solution. Since 12 nm and 7 nm particles were continuously processed in solution, they were more receptive to surfactant adsorption as indicated by the TGA analysis. The

adsorbed NaDBS can act as a plasticizer to the epoxy resin. Since more surfactant was adsorbed on 12 nm and 7nm particles, the surfactant's plasticizing effect was more apparent in those composites and degraded the flexural modulus and strength of the polymer matrix.

The impact of adsorbed NaDBS on the mechanical properties was evident in Samples C10 (V_f = 0.025, 12 nm) and C13 (V_f = 0.0125, 7nm). Their flexural modulus and strength were inferior and displayed anomalous curing behavior. The onset cure temperature of samples C10 and C13 were the lowest at ~71°C and ~100°C, respectively and yet their cure peak temperatures were among the highest at 148-149°C. On the other hand, 12 nm (and 7nm) composites showed a more dispersed microstructructure. As will be discussed, this influenced the fracture properties of the composites.

The trends observed from fracture data of ~5μm and 25nm composites are consistent with particulate composites. For the most part, the fracture toughness (K_{Ic}) of ~5μm and 25nm composites improve with addition of fillers (Figure 4-25), and this is consistent with observations of particulate composites [27]. Analysis of the fracture energy data, G_{Ic}, shows that there is an optimum volume fraction where fracture energy is maximized (Figure 4-26). At filler loading higher than the optimum value, the fillers form clusters and have low resistance to crack propagation. The optimum volume fraction increased from V_f = 0.025 for ~5μm composites to V_f = 0.05 for 25 nm composites. Generally, the optimum volume fraction shifts to higher value when the particle size decreases [27]. For this set of composites, the addition of these fillers improved the fracture energy by more than twice that of the neat polymer at the optimum volume fraction.

Although the fracture energy data showed that ~5μm and 25 nm fillers improved the fracture properties to similar levels, the processing window for 25 nm composites were narrower. In Figure 4-26, the reinforcing effect of 25 nm particles was optimum at V_f = 0.05, but slight deviations from that filler loading would result in significant reduction in fracture energy. For ~5 μm particles, there is greater latitude for deviation from the optimum volume fraction of V_f = 0.025. A slight deviation from V_f = 0.025 would result only in minor decrease in fracture energy. Therefore, from a processing perspective, fracture properties of composites with 5μm particles are more robust than 25 nm particles.

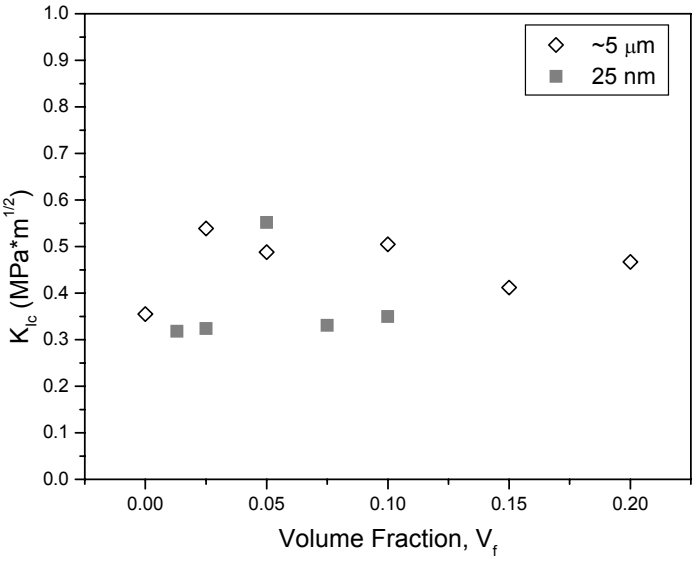

Figure 4-25. Fracture toughness of ~5μm and 25nm composites.

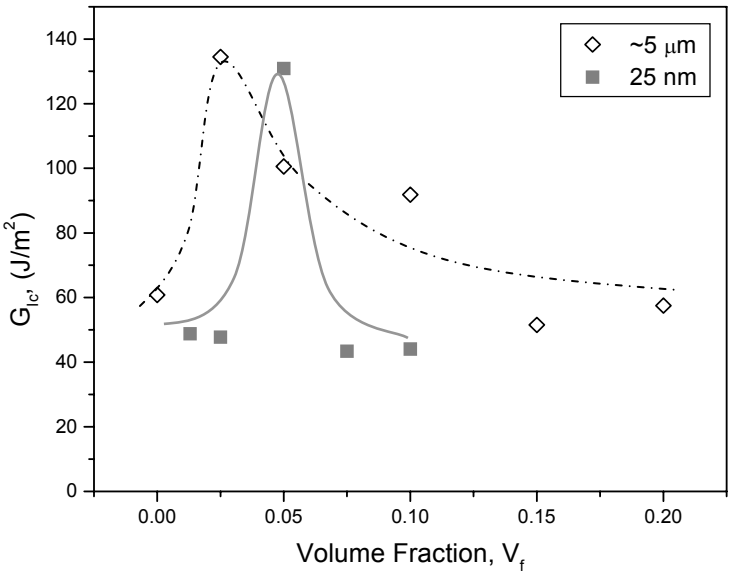

Figure 4-26. Fracture energy of ~5μm and 25nm composites.

The impact of 12 nm and 7nm fillers on fracture behavior is more significant than the larger fillers (see Figures 4-27 and 4-28). The cross section of 12 nm composite at $V_f = 0.025$ showed a more dispersed microstructure than 25 nm composite at the same volume fraction (Figures 4-18 and 4-19). A three-fold increase (relative to neat polymer) in fracture toughness was observed using 12 nm fillers at a filler concentration of $V_f = 0.025$. The fracture toughness also increased by almost three-fold using 7nm fillers and at lower filler concentration ($V_f = 0.0125$). The effects are much more dramatic when comparing the fracture energy. 7nm fillers at $V_f = 0.0125$ increased the fracture energy by an order of magnitude. This amplified effect was a result of a decrease in modulus at that filler concentration, since fracture energy is inversely proportional to elastic modulus. A similar effect also was observed for 12 nm fillers. An optimum volume fraction, i.e. displaying maximized fracture energy, was not

observed in composites with smalle filler size since fabrication of 7 nm and 12 nm nancomposites with higher volume fraction was not successful.

Dispersed nanoparticles in the polymer matrix is important for reinforcing the fracture properties of the matrix. As shown in the cross section of a 25 nm composite (Figure 4-18), clusters and agglomerates as large as 1-2 microns were still present. Therefore, the fracture properties of 25 nm composites were comparable to micron-sized composites. The cross section of a 12 nm composite (Figure 4-19) shows that the nanoparticles were much more dispersed, and consequently the fracture properties were greatly improved. A dispersed microstructure can be assumed for 7 nm composites since the fracture properties were also significantly better than micron-sized and 25 nm composites.

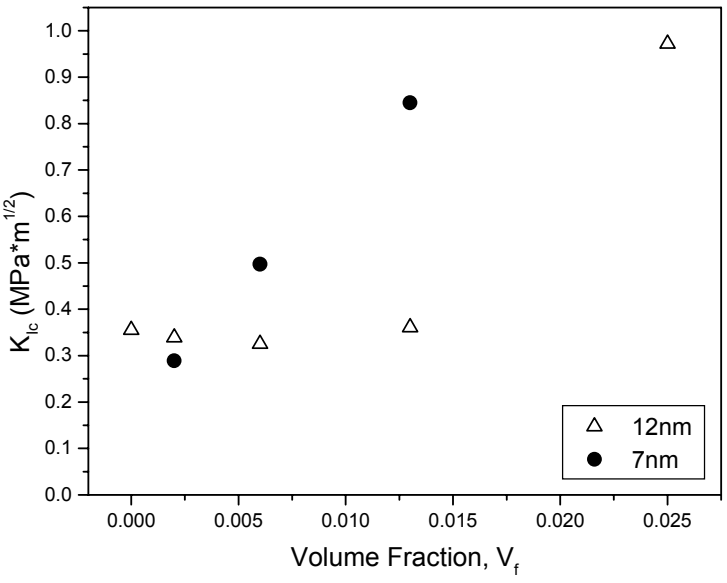

Figure 4-27. Fracture toughness of 12nm and 7nm composites.

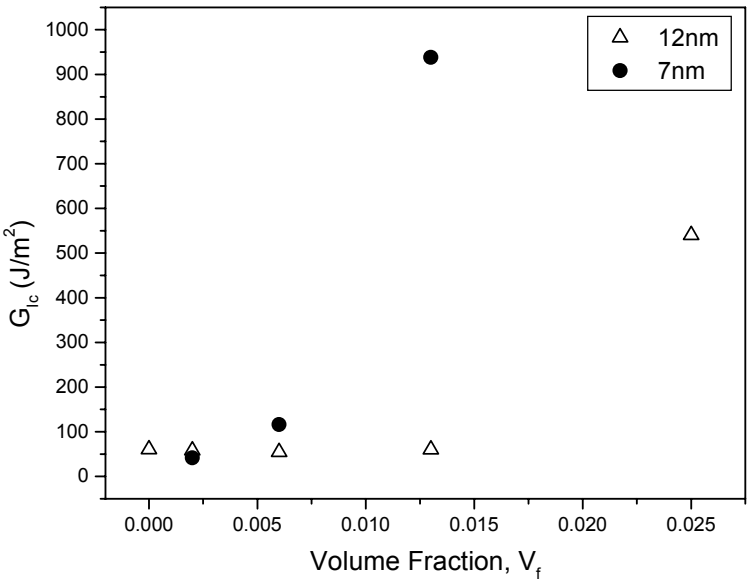

Figure 4-28. Fracture energy of 12nm and 7nm composites.

The interfacial area between polymer and fillers is greater in 12 nm and 7nm composites than in 25 nm composites because the particles are smaller and they were more dispersed. The polymer in the interfacial area could deform plastically and absorb energy from externally applied force. With larger interfacial area that can undergo plastic deformation, 12nm and 7 nm composites have greater resistance for crack propagation, as indicated by their K_{Ic} and G_{Ic} data. The possibility that adsorbed surfactants plasticize the polymer matrix could further explain why 12 nm and 7 nm composites have larger capacity for energy dissipation and their fracture energies were five to ten times greater than the neat polymer matrix. Future studies on the interfacial area between nanoparticles and polymer matrix and the effect of adsorbed surfactant on the properties of polymer at the interface may elucidate how nanoparticles improve the fracture properties of a polymer matrix at low concentrations.

In this part of the study, it was shown that nanoparticles (12 nm and 7 nm) dispersed in the polymer matrix could provide major improvements in fracture properties. The improvements were achieved using low filler loading, V_f = 0.0125 – 0.025 and this is important for application in lightweight materials. These improvements come at a price, where the flexural modulus and strength were greatly reduced. These nanocomposites may be used in conjunction with a fabric- or fiber-reinforced fillers to compensate for the trade-off in properties. This hierachical approach to designing multifunctional composite would be useful because the shortcoming of using nanoparticles to improve fracture properties is addressed by a well-established method of increasing modulus and strength.

Electromagnetic properties

The electromagnetic real and imaginary relative permeabilities of the composites were measured and plotted in Figures 4-29 to 4-31. Data are grouped by particle size and an increase in permeability with volume fraction was observed for all particle sizes. Resonance frequencies appeared to shift with volume fraction and particle size.

The relative permeabilities (real and imaginary) of the fabricated composites increased with the content of Fe_3O_4 particles. Figure 4-32 is a plot of the average real permeabilities in the frequency range of 100 MHz to 200 MHz. The permeabilities are relatively constant within that range of frequency because it is far from the resonant frequencies of all the analyzed samples. Therefore, a direct comparison of the permeabilities of the samples can be made, as in Figure 4-32. At these lower volume fractions, the permeabilities of micron- and nanocomposites increase linearly with filler

volume fraction. This is expected since the volume fractions are lower than the percolation threshold, $V_f \sim 0.33$ for spherical particles. Since the samples prepared in this study are below the percolation threshold, fitting the data to a linear relationship is a valid assumption [28].

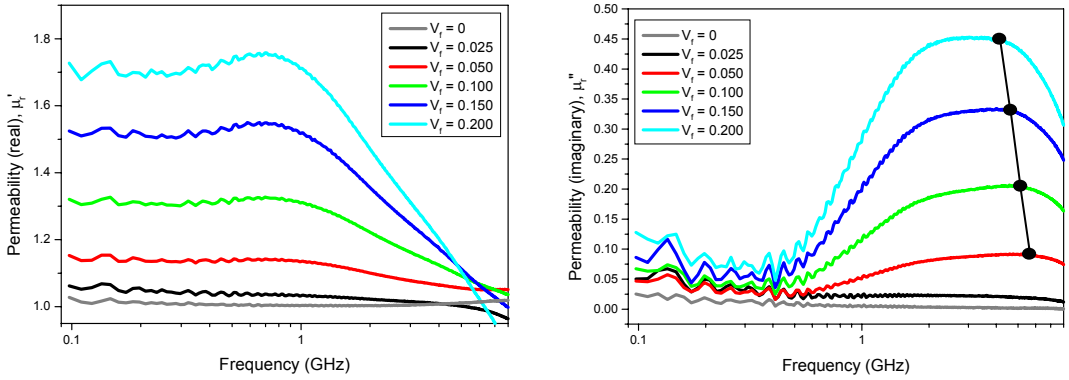

(a) (b)

Figure 4-29. Permeability of ~5um composites (a) real and (b) imaginary.

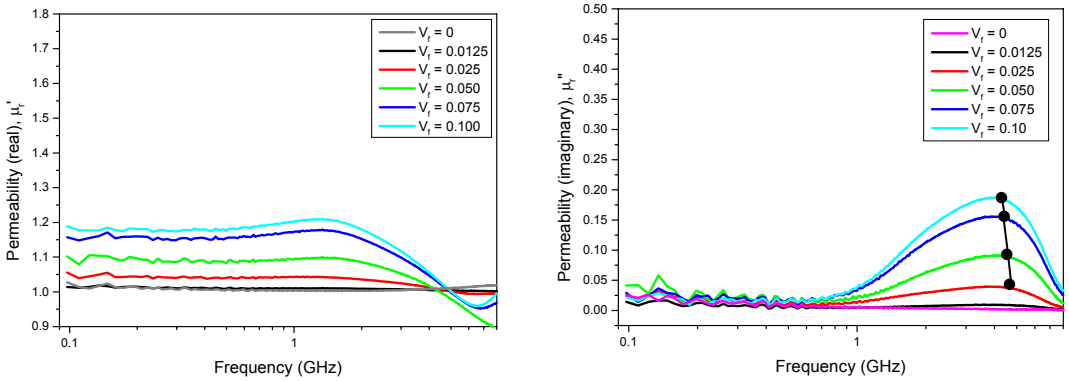

(a) (b)

Figure 4-30. Permeability of 25 nm composites (a) real and (b) imaginary.

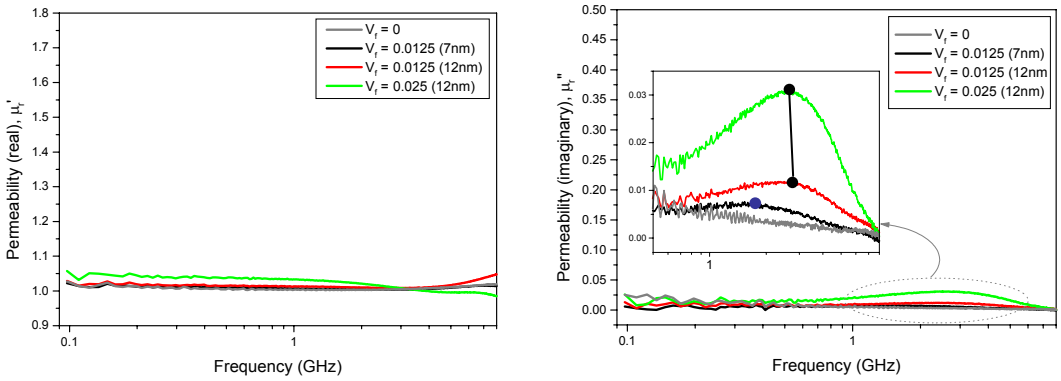

(a) (b)

Figure 4-31. Permeability of 7 nm and 12 nm composites (a) real and (b) imaginary.

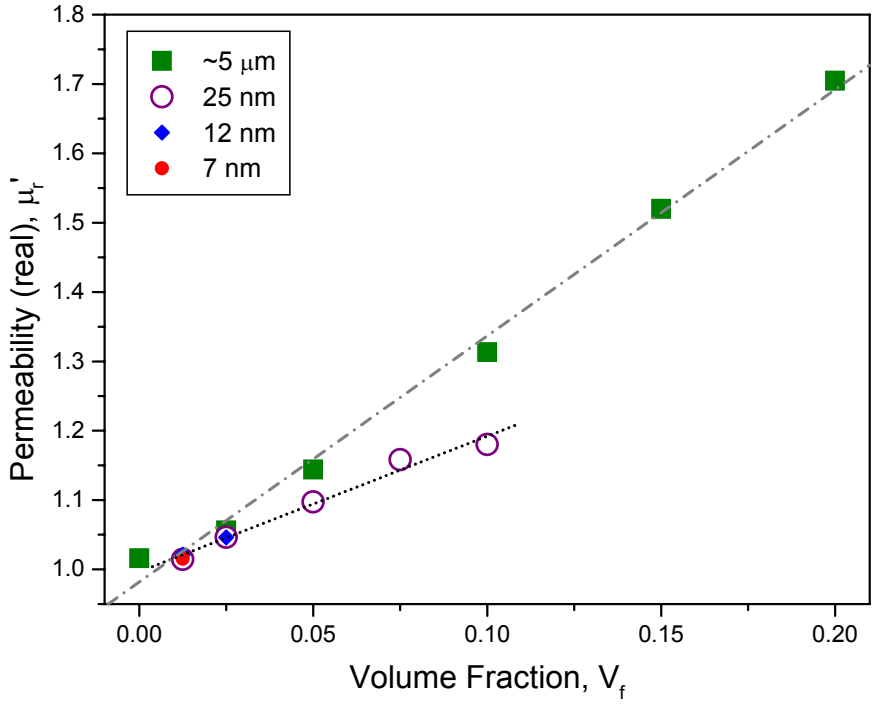

Figure 4-32. Plot of average relative permeability (real) of fabricated composites from 100MHz to 200 MHz.

At the same volume fraction of particles, the permeabilities of nanocomposites are smaller than that of micron-sized composites. This is reasonable since the saturation magnetization of these micron-sized particles was shown in Chapter 3 to be greater than that of the nanoparticles. Table 4-6 lists the magnetization and coercivities of the particles used as fillers in this study. At low volume fractions, the permeability of Fe_3O_4 particles can be calculated using the classical Maxwell-Garnett approximation [29, 30]

$$\frac{\mu_c - \mu_f}{\mu_c + 2\mu_f} = V_m \left(\frac{1 - \mu_f}{1 + 2\mu_f} \right) \tag{4-14}$$

where, μ_f is the permeability of the filler (Fe_3O_4), μ_c is the permeability of the composite, and V_m ($V_f + V_m = 1$) is the volume fraction of the polymer matrix. Since μ_c and V_m were measured or known, the permeabilities of the particles can be calculated by inversion of Equation 4-14. The results of the calculations are shown in Table 4-7, which also lists the μ_c and V_m used to determine the permeabilities of the particles. The decrease in permeability with decreasing particle size is consistent with the magnetization analysis of Fe_3O_4 (nano)particles in Chapter 3, where saturation magnetization decreased as the diameter of the particles were reduced. Therefore, the electromagnetic analysis of composites confirms the strong dependence of magnetic properties on particle size, especially in the case of nanoparticles.

Table 4-6. Properties of Fe_3O_4 (nano)particles.

Particle Size	M_s (emu/g)	H_c (Oersted)
5 μm (Aldrich)	76.62	175
25 nm (Aldrich)	62.29	65
12 nm (synthesized – Sample 19)	58.99	11
7 nm (synthesized – Sample 20)	42.22	1

Table 4-7. Permeabilities of Fe_3O_4 particles and the composite data used in the calculations.

Particle Size	V_f	*average* μ_c (100-200 MHz)	$\mu_f = \mu_{magnetite}$
5 μm	0.10	1.31	5.13
25 nm	0.05	1.18	3.60
12 nm	0.025	1.05	3.39
7 nm	0.0125	1.02	2.50

Figures 4-29(b) to 4-31(b) show that the resonance frequencies of the composites changed with particle size and filler concentration. A resonance frequency is determined to be the frequency where the permeability's imaginary part is at a maximum. The range of resonance frequencies are grouped by the particle (filler) size and summarized in Table 4-8. In the cases of 5 μm, 25 nm, and 7 nm composites, the resonance frequencies increase with decreasing filler concentration, and similar behavior was

reported in other publications [30]. A change in resonance frequencies of 7nm composites with filler content was not observed because samples with $V_f \geq 0.0125$ were not successfully fabricated. The range of resonance frequencies for ~5μm and 25 nm composites are very similar, while 7 nm and 12 nm composites exhibit resonance behavior at lower frequencies.

Table 4-8. Resonance frequencies of composites.

Particle Size	ω_o Resonance Frequency
~5μm	4-5 GHz
25 nm	4-4.5 GHz
12 nm	~2.5 GHz
7 nm	~1.5 GHz

The measured variation in electromagnetic properties of composites containing micron- and nano-sized fillers indicate that particle size could be leveraged as a complementary method of modifying composite properties to the standard method, i.e. volume fraction. As an example, this approach can be useful in applications where permeabilities need to be suppressed, but flexural modulus needs to be maximized. The rise in permeability with filler content is slower when using 25nm fillers instead of micron-sized fillers, but the modulus increases are approximately the same with filler content. Such approach will allow a materials scientist to have additional latitude in designing a composite.

4.6 Summary

A procedure for treating the surface of Fe_3O_4 nanoparticles with NaDBS was developed. The NaDBS-treated nanoparticles displayed better dispersion than without any surface treatment. This was evident when comparing the cross section of 25 nm composites containing surface-treated and untreated particles. Further improvement in dispersion was observed with 12 nm particles, and this was attributed to the continuous wet processing steps during surface treatment of nanoparticles and fabrication of composites. TGA analysis of the nanoparticles showed that more surfactant was adsorbed on the surface of smaller particles as percentage of particle weight, which helped to improve the dispersion of the nanoparticles.

Magnetic nanocomposites were then fabricated using an epoxy-based polymer matrix. The curing behavior of epoxy was affected by the nanoparticles dispersed in it. Their effect was more evident as the volume fraction increased and as the particle size decreased. We theorize that the increased interfacial area between polymer and particles initiated curing at lower temperature, but the nanoparticles also acted as impurities and delayed the completion of curing to a higher temperature. The adsorbed surfactants could also interact with the polymer matrix and result in a plasticizing effect.

The mechanical properties of nanocomposites were measured and compared against composites with micron-sized fillers. Composites with 25 nm fillers behaved similarly to 5 μm fillers. Modulus increased with increasing filler concentration, while strength decreased with it. A recovery in strength was observed in 5 μm composites at $V_f > 0.10$, which is an indication of good bonding between filler and matrix. This behavior was not observed in nanoparticles because fabrication of nanocomposites at

higher filler loading was not successful. The fracture properties of composites containing 12 nm and 7 nm particles were improved over the micron-sized composites. One can see the toughening effect of the nanoparticles at relatively low filler concentration, e.g. $V_f = 0.0125$ for 7 nm fillers and $V_f = 0.025$ for 12 nm fillers. In exchange for the improved resistance to crack growth, 7 nm and 12 nm composites have inferior modulus and strength. This degradation is likely related to the effect of nanoparticles on the curing process of the epoxy resin. The use of nanoparticles in conjunction with fabric- or fiber-reinforcements should be considered to produce hierarchical multifunctional composite system.

The electromagnetic properties of micron-sized composites differed from the nanocomposites. This is explained by the dependence of magnetic properties on particle size, as discussed in Chapter 3. Using Maxwell-Garnett's approximation, the permeabilities of the magnetite particles were calculated. Although there are some limitations to the approximation, the analysis captured the trend that permeability decreased with particle size, which correlates with the trend observed for saturation magnetization. Resonance frequencies were observed in the permeability measurements. 25 nm and 5 μm composites displayed resonance at similar frequencies, between 4 to 5 GHz. 12 nm and 7 nm composites exhibited resonance at lower range of frequencies, starting at approximately 2.5 GHz and 1.5 GHz, respectively. Furthermore, resonance frequencies may be observed at lower volume fraction in nanocomposites. As with mechanical properties, electromagnetic properties of 25 nm composites are more similar to micron-sized composites.

4.7 References

[1] J.-E. Otterstedt and D. A. Brandredth, *Small Particles Technology*. New York: Plenum Press, 1998.

[2] D. H. Everett, *Basic Principles of Colloid Science*. London: Royal Society of Chemistry, 1988.

[3] B. M. Moudgil, P. K. Singh, and J. J. Adler, "Surface Chemistry in Dispersion, Flocculation, and Flotation," in *Handbook of Applied Surface and Colloid Chemistry*, vol. 1, K. Holmberg, Ed. West Sussex: John Wiley and Sons, 2002, pp. 219-249.

[4] I. W. Hamley, *Introduction to Soft Matter*. West Sussex: John Wiley and Sons, 2000.

[5] T. Fried, G. Shemer, and G. Markovich, "Ordered Two-Dimensional Arrays of Ferrite Nanoparticles," *Advanced Materials*, vol. 13, pp. 1158-1161, 2001.

[6] S. Neveu, A. Bee, M. Robineau, and D. Talbot, "Size-Selective Chemical Synthesis of Tartrate Stabilized Cobalt Ferrite Ionic Magnetic Fluid," *Journal of Colloid and Interface Science*, vol. 255, pp. 293-298, 2002.

[7] H. Ishida and J. D. Miller, "Substrate Effects on the Chemisorbed and Physisorbed Layers of Methacryl Silane Modified Particulate Minerals," *Macromolecules*, vol. 17, pp. 1659-1666, 1984.

[8] J. Lin, J. A. Siddiqui, and R. M. Ottebrite, "Surface Modification of Inorganic Oxide Particles with Silane Coupling Agent and Organic Dyes," *Polymers for Advanced Technologies*, vol. 12, pp. 285-292, 2001.

[9] M. Ma, Y. Zhang, W. Yu, H.-Y. Shen, H.-Q. Zhang, and N. Gu, "Preparation and Characterization of Magnetite Nanoparticles Coated by Amino Silane," *Colloids and Surfaces, A: Physicochemical and Engineering Aspects*, vol. 212, pp. 21-226, 2003.

[10] D. K. Kim, M. Mikhaylova, Y. Zhang, and M. Muhammed, "Protective Coating of Superparamagnetic Iron Oxide Nanoparticles," *Chemistry of Materials*, vol. 15, pp. 1617-1627, 2003.

[11] C. Chaneac, E. Tronc, and J. P. Jolivet, "Hybric Composite Materials Containing Magnetic Iron Oxide Nanoparticles," *Materials Research Society Symposium Proceedings*, vol. 628, pp. CC6.4.1-CC6.4.6, 2000.

[12] N. Kallay and E. Matijevic, "Adsorption at Solid/Solution Interfaces. 1. Interpretation of Surface Complexation of Oxalic and Citric Acids with Hematite," *Langmuir*, vol. 1, pp. 195-201, 1985.

[13] A. R. Philipse, M. P. B. van Bruggen, and C. Pathmamanoharan, "Magnetic Silica Dispersions: Preparation and Stability of Surface-Modified Silica Particles with a Magnetic Core," *Langmuir*, vol. 10, pp. 92-99, 1994.

[14] I. J. Bruce, J. Taylor, M. Todd, M. J. Davies, E. Borioni, C. Sangregorio, and T. Sen, "Synthesis, Characterisation and Application of Silica-Magnetite Nanocomposites," *Journal of Magnetism and Magnetic Materials*, vol. 284, 2004.

[15] M. D. Butterworth, S. A. Bell, S. P. Armes, and A. W. Simpson, "Synthesis and Characterization of Polypyrrole-Magnetite-Silica Particles," *Journal of Colloid and Interface Science*, vol. 183, pp. 91-99, 1996.

[16] C. Yee, G. Kataby, A. Ulman, T. Prozorov, H. White, A. King, M. Rafailovich, J. Sokolov, and A. Gedanken, "Self-Assembled Monolayers of Alkanesulfonic and -Phosphonic Acids on Amorphous Iron Oxide Nanoparticles," *Langmuir*, vol. 15, pp. 7111-7115, 1999.

[17] M. R. Porter, *Handbook of Surfactants*, Second ed. Glasgow: Blackie Academic and Professional, 1994.

[18] S. Wall, "Solid Dispersions," in *Handbook of Applied Surface and Colloid Chemistry*, vol. 2, K. Holmberg, Ed. West Sussex: John Wiley and Sons, 2002, pp. 3-21.

[19] J. G. Williams and M. J. Cawood, "European Group on Fracture: K_c and G_c Methods for Polymers," *Polymer Testing*, vol. 9, pp. 15-26, 1990.

[20] J. W. Schultz, "Permeameter Design," GeorgiaTech Research Institute, Atlanta 2005.

[21] W. R. Ashcroft, "Curing Agents for Epoxy Resins," in *Chemistry and Technology of Epoxy Resins*, B. Ellis, Ed. London: Blackie Academic and Professional, 1993, pp. 37-71.

[22] B. Ellis, "Kinetics of Cure," in *Chemistry and Technology of Epoxy Resins*, B. Ellis, Ed. London: Blackie Academic and Professional, 1993, pp. 72-116.

[23] S. J. Shaw, "Additives and Modifiers for Epoxy Resins," in *Chemistry and Technology of Epoxy Resins*, B. Ellis, Ed. London: Blackie Academic and Professional, 1993, pp. 117-143.

[24] R. M. Cornell and U. Schwertmann, *The Iron Oxides*, 2nd ed. Weinheim: Wiley-VCH Verlag GmbH & Co., 2003.

[25] R. M. Silverstein, G. C. Bassler, and T. C. Morril, *Spectrometric Identification of Organic Compounds*. New York: John Wiley and Sons, 1981.

[26] M. P. Stevens, *Polymer Chemistry: An Introduction*, Third ed. New York: Oxford University Press, 1999.

[27] G. V. Jackson and M. L. Orton, "Filled Thermosets," in *Particulate-Filled Polymer Composites*, R. N. Rothon, Ed. Essex: Longman Scientific and Technical, 1995, pp. 317-370.

[28] R. L. McCullough, "Generalized Combining Rules for Predicting Transport Properties of Composite Materials," *Composites Science and Technology*, vol. 22, pp. 3-21, 1985.

[29] T. C. Choy, *Effective Medium Theory: Principles and Applications*. Oxford: Clarendon Press, 1999.

[30] X. Y. Zhang, Y. J. Chen, and T. Y. Cai, "Influences of Temperature and Frequency on Application of EMA in Magnetic Composite," *Materials Letters*, vol. 57, pp. 3315-3319, 2003.

CHAPTER 5

MAGNETIC, CONDUCTIVE, AND MECHANICAL PROPERTIES OF POLYPYRROLE-Fe_3O_4 COMPOSITES

5.1 Introduction

The previous chapter developed, fabricated, and characterized nanocomposites with mechanical and magnetic properties. The impacts of filler content and filler size on the properties of composites were evaluated. Using a similar methodology, this chapter will present the results of a study on composites with magnetic, electrical, and mechanical properties.

In this chapter, multifunctional composites containing polypyrrole-coated 5 μm magnetite particles were used as fillers in a polymer matrix. Electrical conductivity was added to the composite properties by coating the magnetite particles with a conductive polymer, e.g. polypyrrole. Before characterizing the composites' properties, a process that coats magnetite particles with polypyrrole was developed. The effect of polypyrrole coating on the mechanical, electrical, and magnetic properties was measured.

Coating Fe_3O_4 particles with conductive polymer provided multifunctionality to the composite without adding significant weight penalty. If magnetic and conductive fillers were to be added discretely, the following equation would apply:

$$V_m + V_{f,\sigma} + V_{f,\mu} = 1 \tag{5-1}$$

where V_m is the volume fraction of the polymer matrix, $V_{f,\sigma}$ is the volume fraction of conductive filler, and $V_{f,\mu}$ is the volume fraction of magnetic filler. When the

conductivity of the composite is increased (by increasing volume fraction of conductive fillers), it would be at the expense of magnetic properties. In this study, the volume already occupied by Fe_3O_4 was leveraged as platforms for the conductive polymer. By making the surfaces of magnetic fillers conductive with polypyrrole coating, the conductive and magnetic properties may be increased concurrently in a composite. This approach can be useful in developing multifunctional composites.

5.2 Background on Conductive Polymer Coating on Substrates

Conducting polymers have been the focus of much research work since their discovery in 1977 [1-3]. Research work on conductive polymer applications have been targeted mostly on polypyrrole and polyaniline due to their environmental stability [4-6]. However, these polymers present a challenge during processing because they are insoluble and have poor mechanical properties [7]. To circumvent these difficulties, conductive polymers may be coated on organic or inorganic materials (substrates), such as particles and fabrics.

Kuhn *et al*. conducted an extensive research program on developing conductive textiles that have applications as electromagnetic interference (EMI) shielding and anti-static materials [8-12]. They used chemical oxidative polymerization to coat polypyrrole and polyaniline on polyester fabrics. The scheme of chemical oxidative polymerization for polypyrrole is shown in Figure 5-1 [7, 13]. An oxidizing agent initiates the polymerization by forming cation radicals of the monomer. The radicals subsequently react with another monomer to form a dimer. The dimer is oxidized and forms another cation radical, and continues the polymerization reaction.

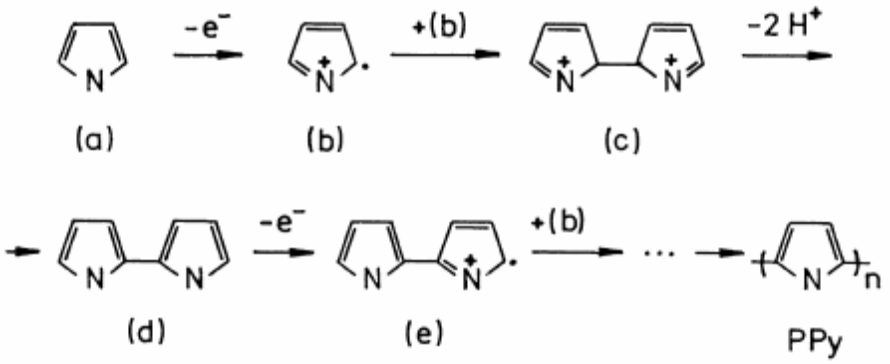

Figure 5-1. Scheme of chemical oxidative polymerization of polypyrrole, from Malinauskas [7]

Kuhn *et al*. reported on the process parameters that facilitated polymerization on the surface of substrates [8, 12]. They found that the monomer concentration should be dilute, less than 0.02 M; a concentration that is approximately 5 to 10 times lower than those used by other groups [12]. At dilute conditions, the monomer complexes with oxidizing agent forming a pre-polymer species that readily adsorbs on the surface of substrates. Ferric chloride ($FeCl_3$) is an effective oxidizing agent for polymerization of pyrrole, and its optimum concentration is in the range of two to three times the concentration of monomer. High conductivities are achieved using anthraquinone-2-sulfonic acid (ASA) as dopant and the recommended concentration is about 0.25 to 0.5 of pyrrole's concentration. A fast polymerization rate favors formation of polypyrrole in solution, reduces the degree of order in polypyrrole, and results in coating with lower conductivity. Therefore, to maximize conductivity of the coating, control of polymerization rate is important.

Although other groups have reported coating polypyrrole on organic and inorganic particles, the procedures were more complicated and/or did not produce the desired coating. For example, particles were stabilized in colloids during the coating process but an additional step of steric stabilization prior to coating of polypyrrole (or polyaniline) was required [14, 15]. In other reports, the coatings were thick and/or had low conductivity [5, 16]. In the work here, we sought to minimize coating thickness of the conductive polymer to maintain maximum magnetic permeability. Kuhn *et al.* developed a process where the conductive polymer coating was less than 1 μm [12]. Therefore, the method for making conductive fabric was selected as the basis for polypyrrole coating process on Fe_3O_4 particles.

5.3 Experimental Procedure

5.3.1 Coating Particles with Polypyrrole

The following procedure describes the details for preparing Sample P7 as listed in Table 5-2 in Section 5.5.1. This method is applicable for the preparation of other samples that will be discussed in that section. The exact amount of pyrrole, anthraquinone-2-sulfonic acid (ASA), and $FeCl_3$ can be calculated from their concentrations listed in Tables 5-1 and 5-2. The basis of those concentrations is the total reaction volume, which is 250 mL.

4.69 g of $FeCl_3 \cdot 6H_2O$ was dissolved in 200 mL of distilled water. 0.235 g of ASA was added into the same solution, which was stirred and heated to approximately 60°C to facilitate dissolution. The prepared solution of $FeCl_3$ and ASA was transferred into a 500 mL 3-neck flask and cooled to 10°C using an ice bath. This solution was

deoxygenated for approximately 30 minutes while it was being cooled. 7 g of 5 μm Fe_3O_4 particles were then added into the flask to form a slurry which was then stirred vigorously under N_2 blanket.

In a separate beaker, 0.235 g of ASA was dissolved in 50 mL of distilled water. This solution was also placed in an ice bath to cool to same temperature as the Fe_3O_4 slurry. 300 μL of pyrrole was added into the solution of ASA and mixed until miscible. The solution of ASA and pyrrole was added slowly into the slurry, at a rate of approximately 1 mL per minute. Polymerization was allowed to proceed for a total of four hours (starting from when ASA/pyrrole solution was added) at 10-15°C under nitrogen blanket.

The coated particles were separated from the reaction solution using a permanent magnet. The particles were rinsed three times with approximately 250 mL of distilled water, until the supernatant was clear. The particles were filtered out of the final rinse solution and then dried in an oven at 75-80°C for 12 hours. The coated particles were characterized using TGA, FTIR, 4-point probe, and SEM.

5.3.2 Composite Fabrication

The composites were fabricated using the same epoxy formulation as the nanocomposites in Chapter 4. Fe_3O_4 or PPy-coated Fe_3O_4 fillers were added to the epoxy blend (resin, hardener, and curing agent) and then mixed using a high shear blade at 760 rpm for 10 minutes. The composite blend was poured into molds, degassed for 6 hours in a vacuum oven and cured at 140°C for 2 hours followed by 160°C for 1 hour.

5.4 Characterization Equipment and Procedures

Several of the characterization methods used to analyze these composites were the same as those used to analyze the nanocomposites in Chapter 4. Please refer to that chapter for details on FTIR, TGA, DSC, and characterization of mechanical properties and electrogmagnetic properties.

5.4.1 SEM

A scanning electron microscope (SEM) was used to view Fe_3O_4 particles at high magnifications. The LEO 1530 thermally-assisted field emission SEM was used for analysis of the particles. Operating voltage was in the range of 2-4 kV to minimize charging on the sample. The particles were spread across a double-sided copper tape and mounted on an SEM sample holder.

5.4.2 4-pt probe

A standard four-point probe technique was used to measure the surface conductivity of polypyrrole-coated and uncoated Fe_3O_4 particles and bulk conductivity of composites. The particles were pressed into a pellet, approximately 13 mm in diameter and 0.5 to 2 mm in thickness. Pellet molds were machined from a teflon rod by the Georgia Tech Research Institute Machine Shop. A Carver Laboratory Press was used to shape the pellets at forces ranging from 2500 – 3000 lb_f or approximately 97,000 psi (670 Mpa). This is a similar procedure used to prepare VSM samples of (nano)particles, except that no binder was used here. Composite samples were trimmed

using a diamond saw into rectangular pieces, approximately 6 mm in width, 30 mm in length and 1 to 2 mm in thickness.

5.5 Results and Discussion

5.5.1 Optimization of Polypyrrole Coating on Fe_3O_4 Particles

Polypyrrole coating on Fe_3O_4 particles provided the opportunity to add electrical conductivity to the list of composite functionalities. Bulk magnetite inherently has high conductivity (~94 S/cm), but small particles have large exposed surface area and are prone to oxidation, and therefore the particles have a high contact resistance [17]. A process to coat the surface of 5 μm Fe_3O_4 particles with polypyrrole was developed to increase the surface conductivity of these particles. These particles were used as fillers to make multifunctional composites with electrical, magnetic, and mechanical properties.

Coating Fe_3O_4 particles with polypyrrole was adapted from the procedure used to coat conductive polymer on quartz and polyester fabric by chemical oxidative polymerization [8-12]. Polymerization of polypyrrole or polyaniline on the fabric was maximized and produced smooth and uniform coatings by finding an optimum ratio of monomer concentration to substrate area. A similar study was conducted here using Fe_3O_4 particles as the substrate and targeting the same goal of uniform polypyrrole coating with maximum conductivity on the particles. Previous research reported that a coating of 5 to 10 weight percent of the particles (substrate) is ideal [18].

Table 5-1 lists the concentration of pyrrole (based on total reaction volume) and the weight percent of PPy, which were determined from TGA analysis. Sample P1 did

not have enough pyrrole to produce the targeted amount of polypyrrole coating. In contrast, increasing the amount of pyrrole by five-fold was excessive, as in Sample P2 that had 30 wt% of polypyrrole. A high concentration of pyrrole monomer in the reaction solution may also increase the fraction of pyrrole that polymerizes in solution and can produce an uneven coating [8, 10, 12, 15]. The weight percent of polypyrrole in Sample P3 was within the targeted range of 5 to 10 weight %. Therefore, sample P3 was used as the baseline condition for further refinements of polypyrrole coating process.

Table 5-1. List of polypyrrole-coated Fe_3O_4 and pyrrole concentration.

Sample ID	pyrrole concentration [M]	Wt % PPy (from TGA)
P1	1.16×10^{-2}	3-4
P2	5.76×10^{-2}	30
P3	1.73×10^{-2}	7

The purpose of the polypyrrole coating was to improve the electrical conductivity of Fe_3O_4 particles. Therefore, the response that was monitored in this part of the optimization study was conductivity of the coated particles. For comparison, the conductivity of uncoated Fe_3O_4 particles was measured to be 3.86×10^{-2} S/cm, which is comparable to reported values [8]. All samples in Table 5-2 show increases in conductivity. The parameters that were evaluated include the concentration of dopant (ASA) and oxidizing agent ($FeCl_3$) and polymerization time and temperature. Table 5-2 also includes the experiment matrix and highlights (bolded and italicized) the parameter

that was varied at each set of process conditions and the properties of the coated particles. The table also includes Sample P3 since it was the baseline condition. Figure 5-2 showed the TGA scans of samples P3 to P7.

Table 5-2. Experiment matrix for optimizing conductivity of polypyrole-coated Fe_3O_4.

Sample ID	ASA conc'n [M]	$FeCl_3$ conc'n [M]	Reaction time (hours)	Reaction temperature (°C)	Wt% PPy	Conductivity* (S/cm)
P3	5.72×10^{-3}	6.93×10^{-2}	4	25	6	1.09
P4	***1.04×10^{-2}***	6.93×10^{-2}	4	25	10	1.12
P5	5.72×10^{-3}	6.93×10^{-2}	***14***	25	15	1.03
P6	5.72×10^{-3}	***1.04×10^{-1}***	4	25	15	0.92
P7	5.72×10^{-3}	6.93×10^{-2}	4	***10-15***	6	2.12

*For comparison, measured conductivity of uncoated Fe_3O_4 particles is 3.86×10^{-2} S/cm.

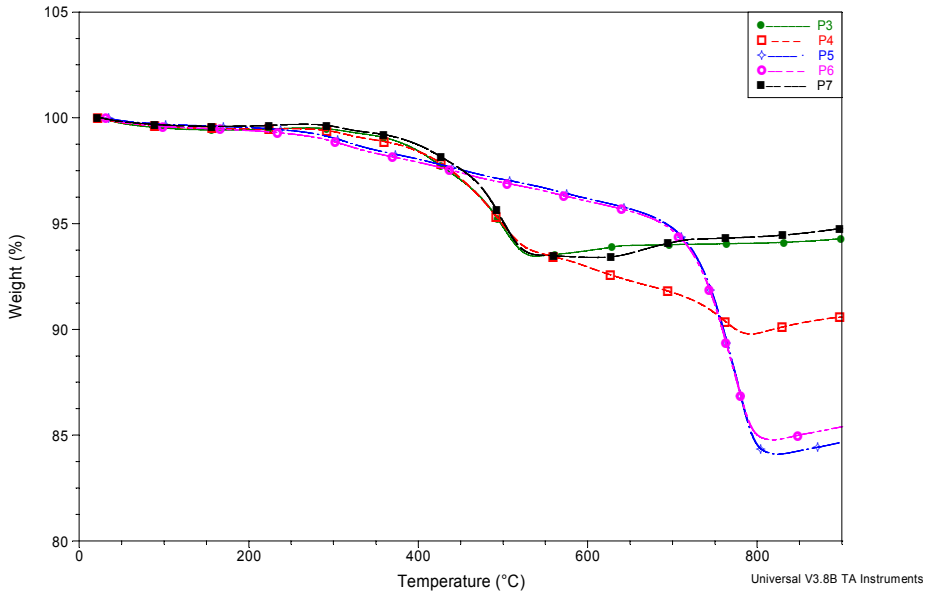

Figure 5-2. TGA of Samples P3 to P7.

Increasing the reaction time, concentration of dopant, and concentration of oxidizing agent increased the amount of polypyrrole coating. Assuming that only a fraction of the pyrrole monomers was consumed in four hours, it is reasonable to see the weight increase in polyprrole when the reaction time was increased (as in Sample P5). Increasing the concentration of $FeCl_3$ should increase the polymerization yield, since it initiates the reaction. This effect was demonstrated by the polypyrrole weight increase in Sample P6. ASA not only acts as a dopant, but can also function as an initiator [8, 13]. Therefore, increasing its concentration had a similar effect as the oxidizing agent, but to a lesser degree as in Sample P4. However, increasing the concentration of ASA did not result in increased conductivity. It has been reported that optimum conductivity is achieved when there is one mole of dopant for every three to four moles of monomer, but additional dopant does not improve conductivity [12].

The process parameters of Sample P7 were selected for coating Fe_3O_4 particles and then used as fillers in multifunctional composites. Sample P7 had the highest conductivity of the samples in Table 5-2 and its polypyrrole weight fraction was within the recommended range. The higher conductivity achieved in Sample P7 was most likely due to the lower reaction temperature. The reduced temperature probably delayed initiation of polymerization and/or slowed the rate of polymerization [10]. Kuhn *et al*. proposed that pyrrole and its oxidizing agent, $FeCl_3$, form a complex that adsorbs on the surface of the substrate and then undergo polymerization [8]. Delaying the polymerization allowed time for the complex to form and then adsorb on the surface of particles [10]. Furthermore, a decrease in polymerization rate can promote higher degree of order in the product, which increases conductivity. In summary, the lower

temperature enhanced polymerization on the surface and produced more uniform coating of polypyrrole on Fe_3O_4 particles, resulting in higher conductivity.

Polypyrrole is a black powder so it is not easy to discern between PPy-coated and uncoated Fe_3O_4 particles, which also has a black granular appearance. However, inspection of the particles at high magnification using an SEM showed that there were distinct differences. Figure 5-3 is an SEM image of uncoated Fe_3O_4 particles, as purchased from Aldrich. The uncoated particles were faceted but the surfaces can be described as smooth. Figure 5-4 shows an SEM image of polypyrrole coated Fe_3O_4 particles and the surfaces are textured. The globular morphology was also observed in polypyrrole-coated polystyrene latexes and quartz fabrics [19, 20]. It appeared that smaller particles clustered together during the coating process, and some were attached to the surface of the larger particles.

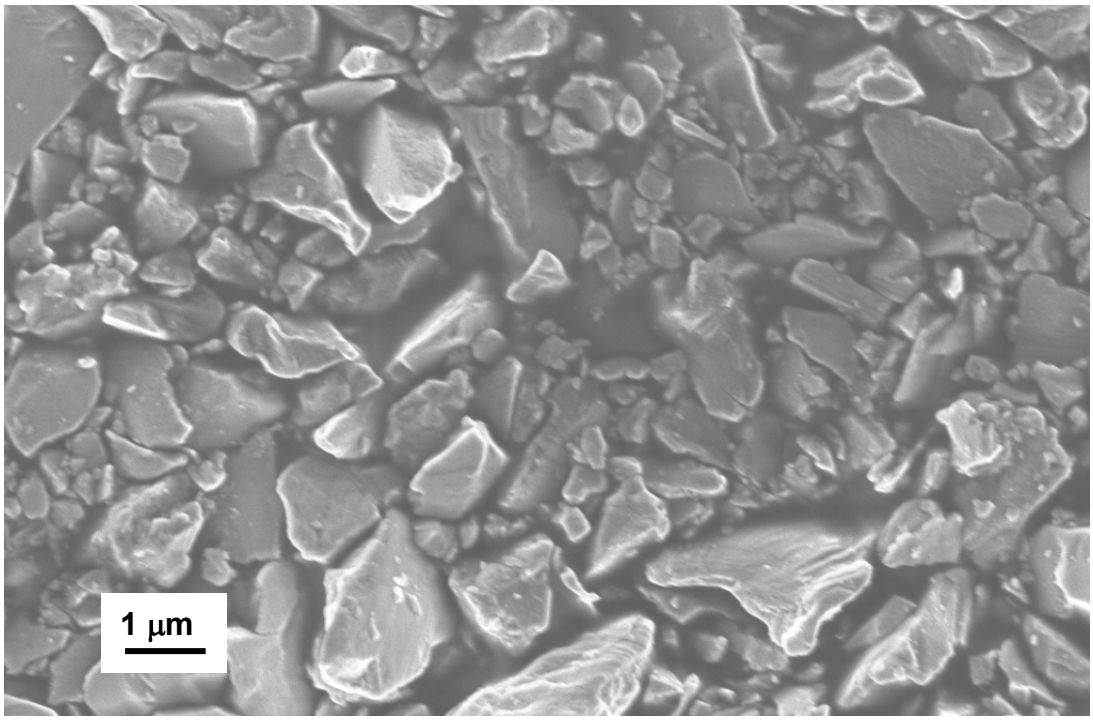

Figure 5-3. SEM image of as-purchased Fe_3O_4 particles.

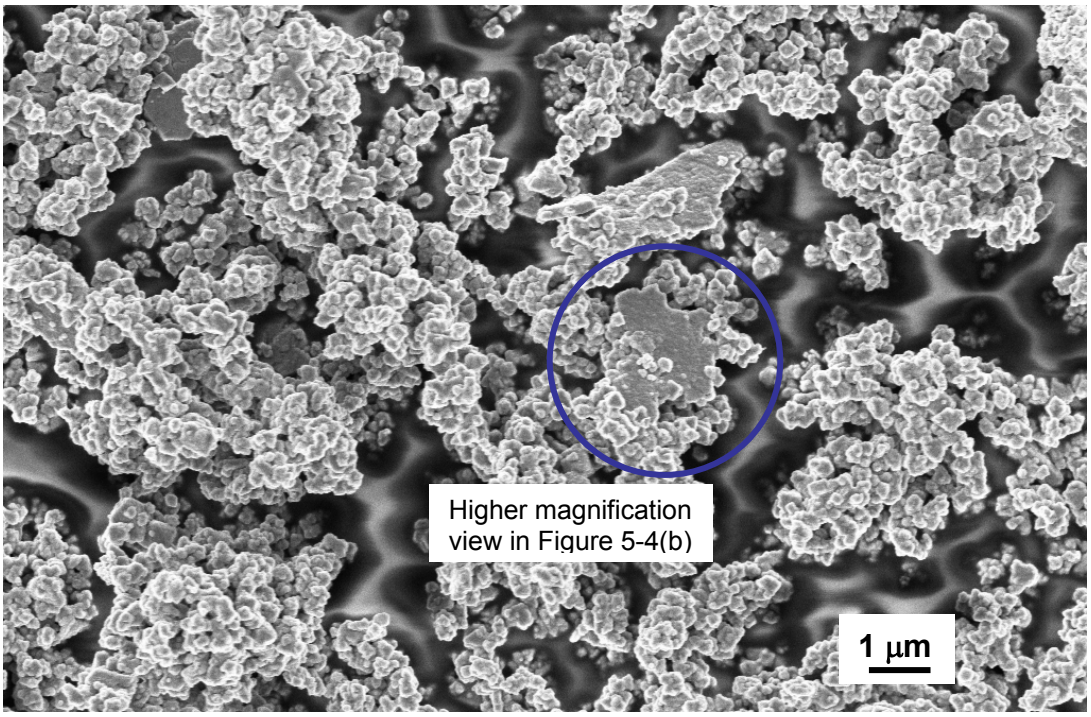

(a)

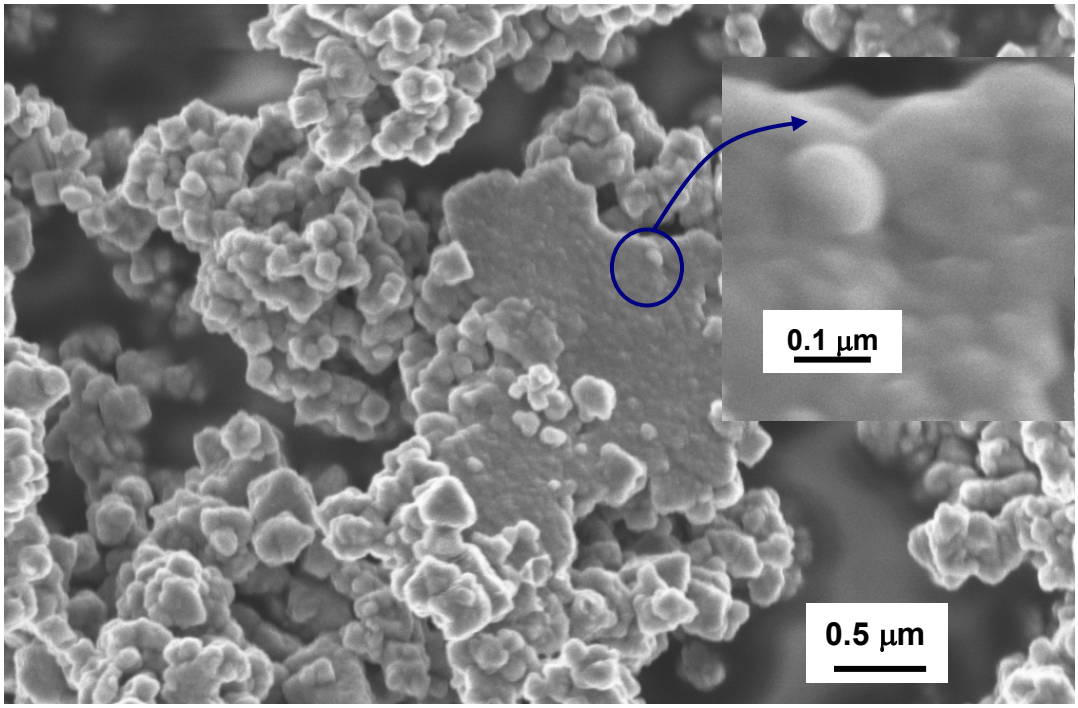

(b)

Figure 5-4. SEM image of polypyrrole-coated Fe_3O_4 particles at (a) low magnification and (b) high magnification.

The thermal stability of polypyrrole was improved when it was polymerized on a substrate such as Fe_3O_4. The TGA scans of Sample P3 and polypyrrole in Figure 5-5 shows differences in thermal stability between the two samples. The polypyrrole sample was produced using the same conditions as the coating process except without the Fe_3O_4 particles. Therefore, polypyrrole polymerized exclusively in solution. The polypyrrole powder was collected and dried as described for coated particles. TGA analyses found that the decomposition temperature of pure polypyrrole was 335°C while the polypyrrole coating on Fe_3O_4 decomposed at 371°C. Other groups have observed this behavior and attributed the improved thermal stability to interaction between Fe_3O_4 and PPy backbone [20]. Comparison of the FTIR spectra of polypyrrole and polypyrrole-coated Fe_3O_4 (Figure 5-6 and Table 5-3) indicated that two peaks have shifted: one of the peaks was assigned to pyrrole ring vibrations (1540 cm^{-1}) and the other peak was assigned to C-H in plane vibrations (1170 cm^{-1}). The observed shift in peaks supports the assertion of chemical bonding between polypyrrole and the surface of magnetite particles.

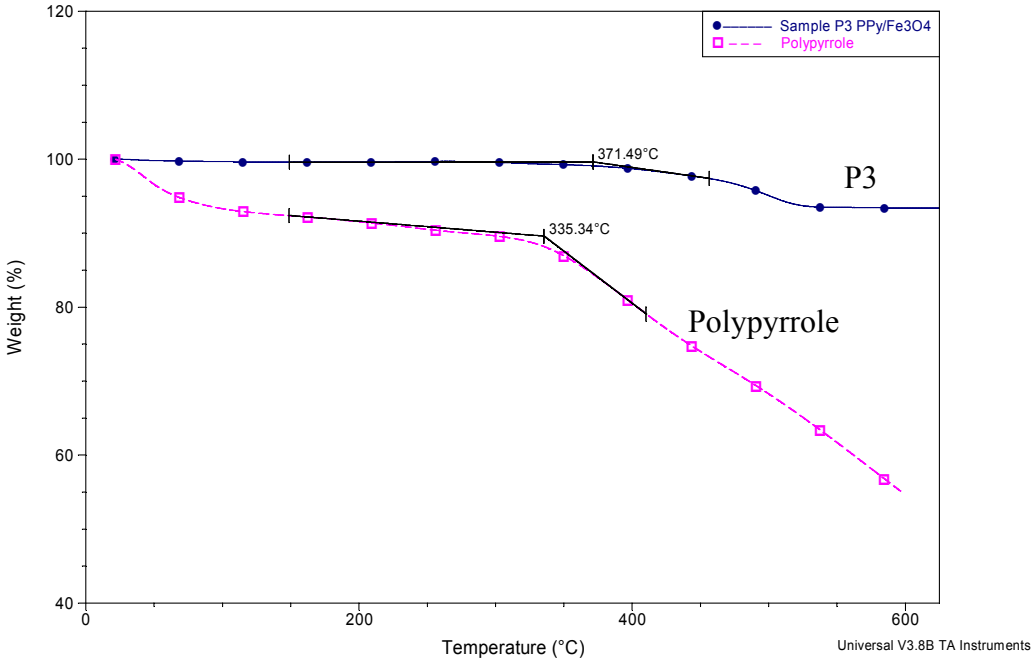

Figure 5-5. TGA scans of Sample P3 and polypyrrole.

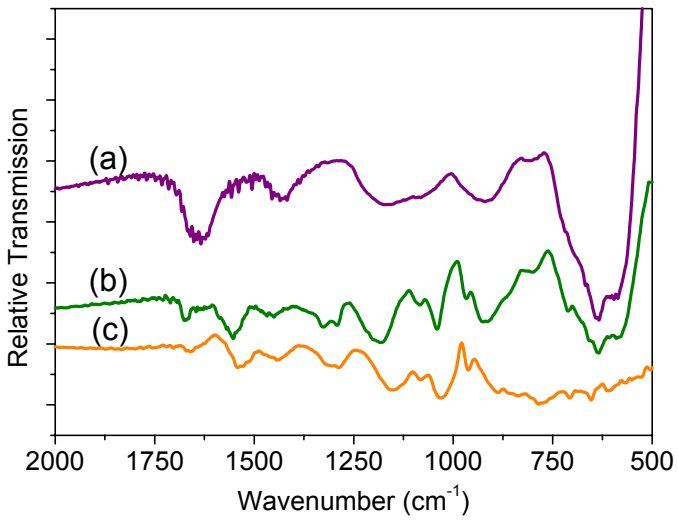

Figure 5-6. FTIR spectra of (a) Fe_3O_4 particles (b) PPy-coated Fe_3O_4 and (c) PPy.

Table 5-3. Characteristic peaks of polypyrrole and Fe_3O_4 particles.

580-600cm^{-1}	Characteristic of Fe_3O_4
*1540** and 1460 cm^{-1}	Pyrrole ring vibrations
1300, *1170**, 1089 cm^{-1}	C-H in plane vibrations
784 and 903 cm^{-1}	C-H out of plane vibrations

**Shifted Peaks*

5.5.2 Mechanical properties

The primary purpose of the polypyrrole coating on magnetite particles was to add electrical conductivity to the composites, but the impact of the coating on mechanical properties must be evaluated. The mechanical properties of composites with 5 μm Fe_3O_4 fillers were compared against the properties of composites with 5 μm PPy-coated Fe_3O_4 fillers. Table 5-4 lists the measured properties of each sample and Figures 5-7 to 5-10 presents them graphically. Samples C1 and C14-C19 were discussed in Chapter 4 and they will be used as control samples again in this chapter.

Table 5-4. Mechanical properties of Fe_3O_4 and PPy-coated Fe_3O_4 composites.

Sample			Mechanical Properties			
Sample ID	**Particle Size and Treatment**	**Vf**	**Flexural Modulus (MPa)**	**Flexural Strength (MPa)**	**K_{IC} ($MPa \cdot m^{1/2}$)**	**G_{IC} (J/m^2)**
C1	--	0	2958.38 ± 58.07	140.72 ± 3.40	0.355 ± 0.027	60.8
C14	5μm	0.025	3084.06 ± 15.61	131.95 ± 10.37	0.539 ± 0.019	134
C15		0.050	3386.60 ± 41.43	108.04 ± 19.37	0.488 ± 0.117	101
C16		0.100	3965.18 ± 138.85	82.40 ± 26.75	0.505 ± 0.190	91.8
C17		0.150	4717.23 ± 73.90	83.35 ± 32.02	0.412 ± 0.144	51.5
C18		0.200	5424.51 ± 98.34	96.43 ± 9.02	0.467 ± n/a	57.5
C19	5μm/PPy	0.025	3226.64 ± 94.94	107.94 ± 9.02	--	--
C20		0.050	3402.41 ± 75.43	94.34 ± 9.02	0.449 ± 0.067	84.5
C21		0.100	4005.09 ± 75.01	96.85 ± 9.02	0.457 ± 0.096	74.6

Flexural modulus measurements of the composites showed that uncoated and polypyrrole-coated Fe_3O_4 particles have similar reinforcing effects on the polymer matrix at $V_f \leq 0.10$. Figure 5-7 is a plot of the flexural modulus with volume fraction and the modulus of both composite sets increased linearly with volume fraction of the fillers. The modulus of composites with polypyrrole-coated fillers was slightly higher than samples with uncoated fillers (see Table 5-4). Measurement of modulus using

quartz fabrics as the reinforcing phase also showed an increase in modulus when the fabrics were coated with polypyrrole [20].

A comparison of the flexural strengths of composites with and without polypyrrole coating on the magnetite fillers showed a greater difference between them. The recovery in strength (as discussed in Chapter 4) was observed in both sets of samples. The strength recovery of composites with plain Fe_3O_4 particles initiated at $V_f > 0.10$, but the strength of composites with polypyrrole-coated fillers began to recover at $V_f > 0.05$. In fact at $V_f = 0.10$, the strength of Sample C21 (with PPy coating) was greater than the strength of Sample C16 (without PPy coating). These data are consistent with preliminary studies that polypyrrole coating on quartz fabrics improved the strength of composites [20]. Based on analysis of the flexural properties, the polypyrrole coating on the magnetite can be advantageous. The coating could provide not only additional functionality to the composites, but it also improved the mechanical properties.

The polypyrrole coating on Fe_3O_4 particles had the characteristics of a coupling agent. Previous sections presented some evidence indicating polypyrrole chemisorbed on the surfaces of Fe_3O_4 particles. Thus, the presence of polypyrrole coating may have improved compatibility between the inorganic filler and the polymer matrix, which is essentially the function of coupling agent [21]. Adhesion studies of epoxy on bare Fe_3O_4 and polypyrrole-coated Fe_3O_4 could give insight on the interfacial role of polypyrrole on mechanical properties, and should be considered as part of future studies.

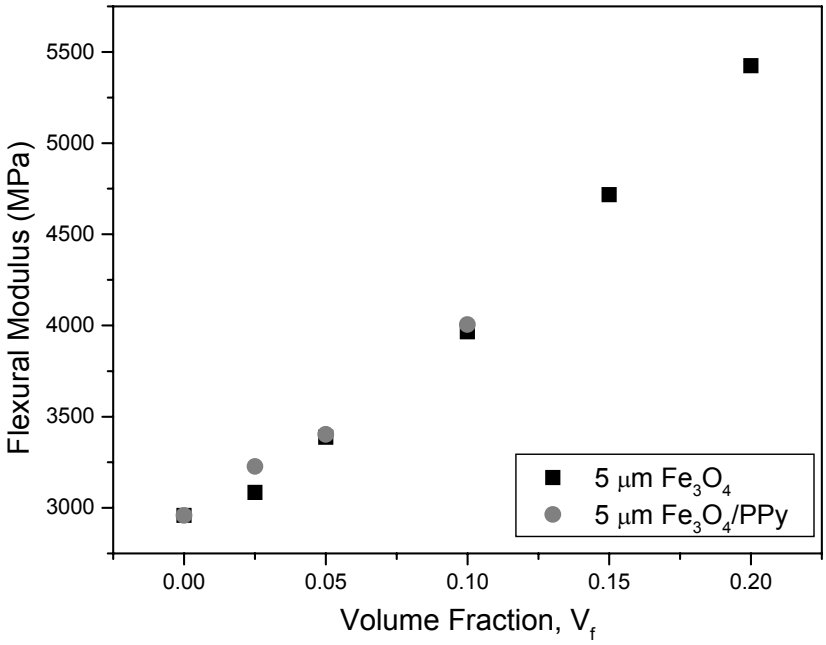

.

Figure 5-7. Flexural modulus of Fe_3O_4 and PPy-coated Fe_3O_4 composites.

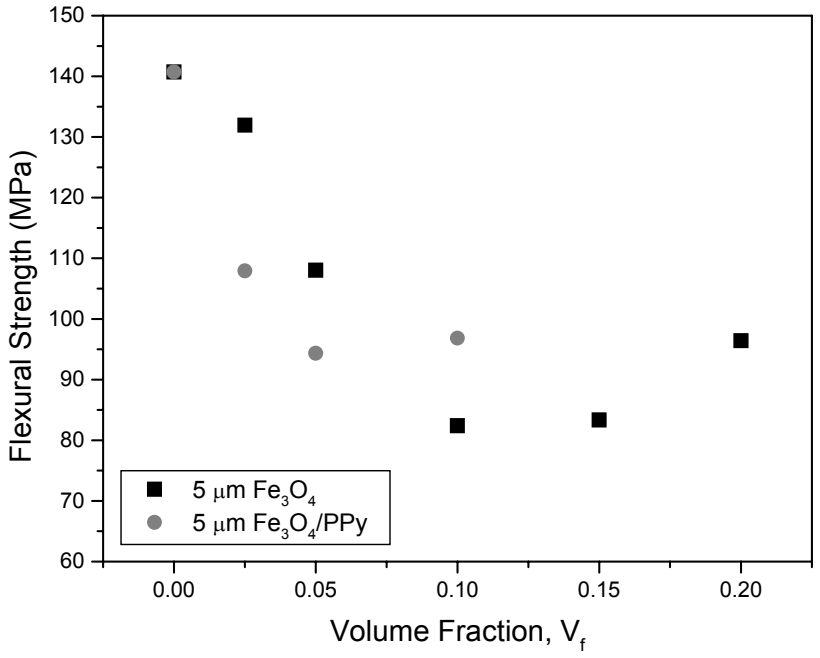

Figure 5-8. Flexural strength of Fe_3O_4 and PPy-coated Fe_3O_4 composites.

Measurements of fracture properties are shown in Figures 5-9 and 5-10. The fracture toughness of composites with coated and uncoated fillers were higher than the neat polymer. Fracture data for Sample C19 (V_f = 0.025, 5μm Fe_3O_4/PPy) was not obtained since all specimens were damaged during the preparation of the sharp crack. The two data points that were available showed the possibility for an optimum filler content where the composite has maximum fracture properties, as observed for the uncoated Fe_3O_4 composites. In contrast to flexural properties, the fracture properties of composites with polypyrrole coating on the fillers were lower than those containing bare Fe_3O_4 fillers. The SEM pictures of coated particles show the possibility of clusters that formed during the coating process. These clusters could be weak points with lower resistance to crack propagation. In addition, fracture properties are not easily predicted based on the flexural properties, but generally rigidity of material is increased at the expense of toughness [22].

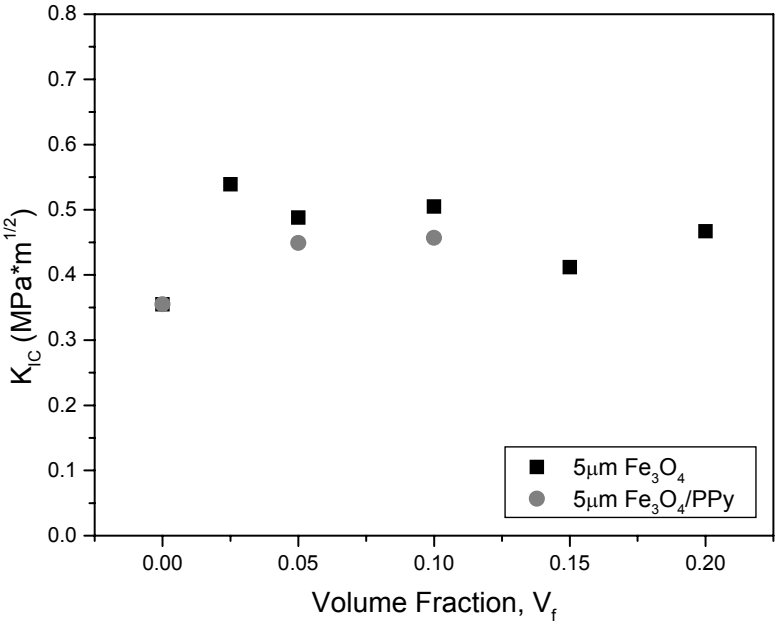

Figure 5-9. Fracture toughness of Fe_3O_4 and PPy-coated Fe_3O_4 composites.

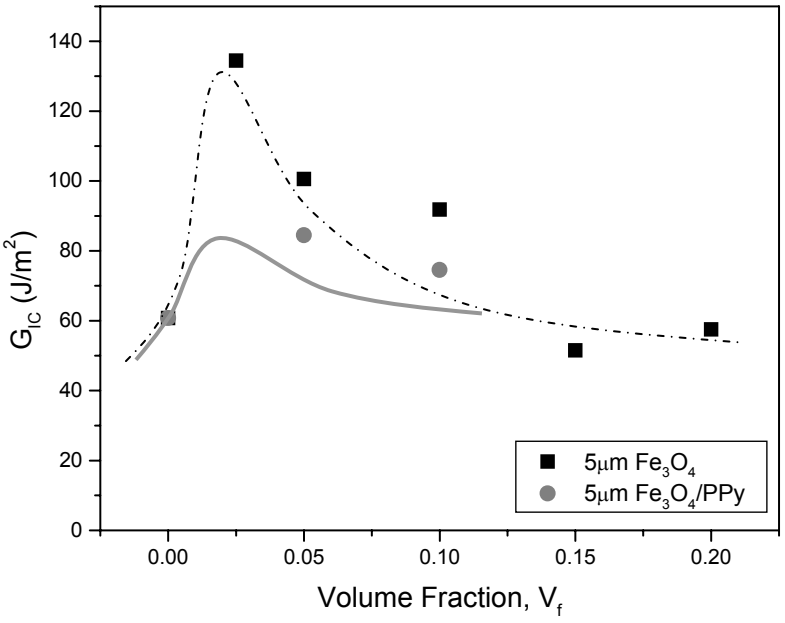

Figure 5-10. Fracture energy of Fe_3O_4 and PPy-coated Fe_3O_4 composites.

5.5.3 Electromagnetic properties

Continuing with the multifunctional characterization, this section presents the measured electromagnetic properties of the fabricated composites. The permeabilities were measured in the frequency range of 100 MHz to 8 GHz. The real and imaginary parts of permeabilities were plotted in Figures 5-11 and 5-12, respectively. Measurements found that both sets of composites (PPy-coated Fe_3O_4 and bare Fe_3O_4) had comparable permeabilities. To insure that the comparisons of electromagnetic properties were consistent, the volume fraction of filler in Samples C19-C21 (composites with PPy-coated Fe_3O_4) accounted for the contribution of only magnetite.

The resonance frequencies of composites with and without polypyrrole coating were also similar. Polypyrrole coating was not expected to affect the resonance frequency because it is not magnetic. The coating was sufficiently thin that diamagnetic response was not introduced and permeability of the composite was maintained. The data in Figures 5-11 and 5-12 supported that observation.

The average real permeabilities of the composites at lower frequency were calculated by averaging them in the frequency range of 100 to 200 MHz. Those averages are plotted in Figure 5-13. The permeabilities of both composite sets increased linearly with volume fraction. This is expected for volume fractions below the percolation [23]. This trend was also observed using fillers of smaller particle size, as discussed in Chapter 4 with 25 nm Fe_3O_4 fillers.

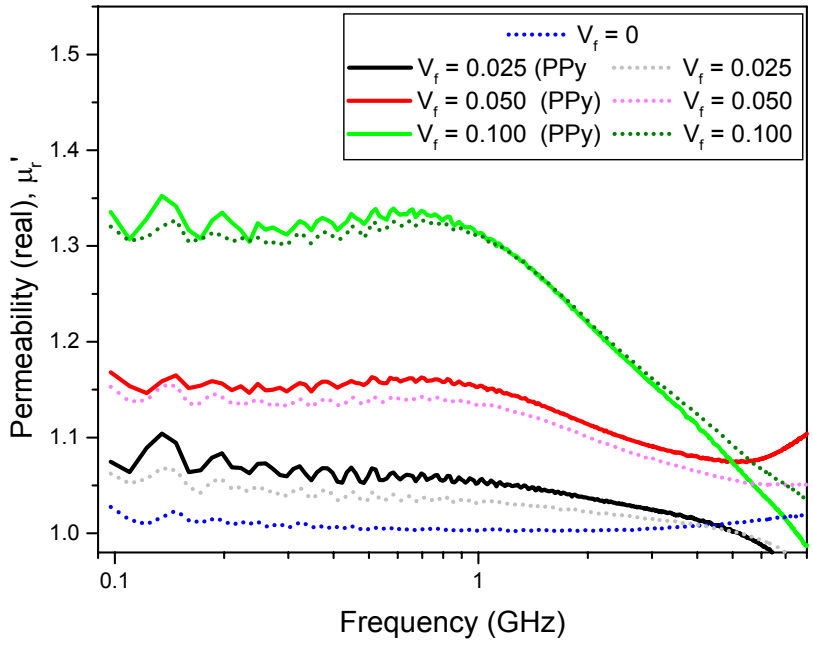

Figure 5-11. Permeability (real) of Fe_3O_4 and PPy-coated Fe_3O_4 composites.

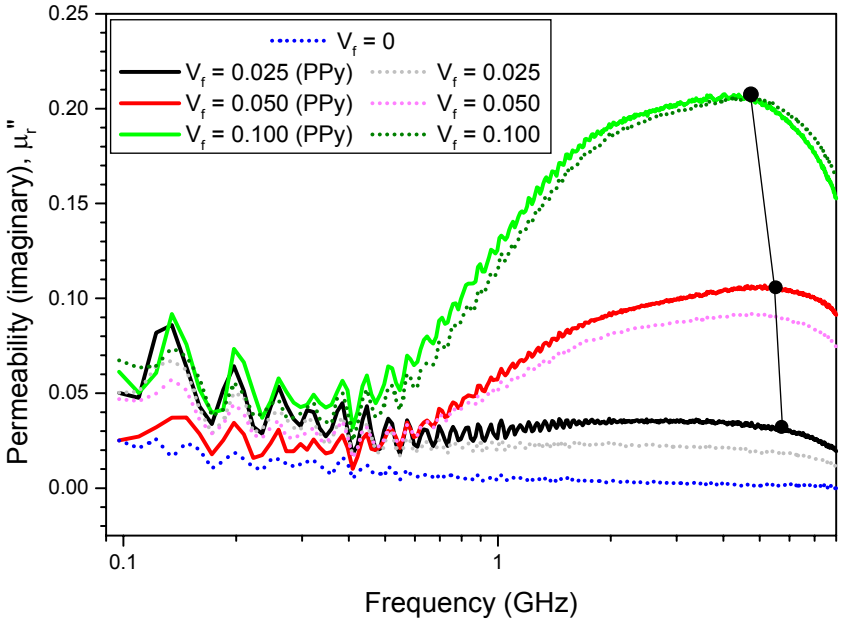

Figure 5-12. Permeability (imaginary) of Fe_3O_4 and PPy-coated Fe_3O_4 composites.

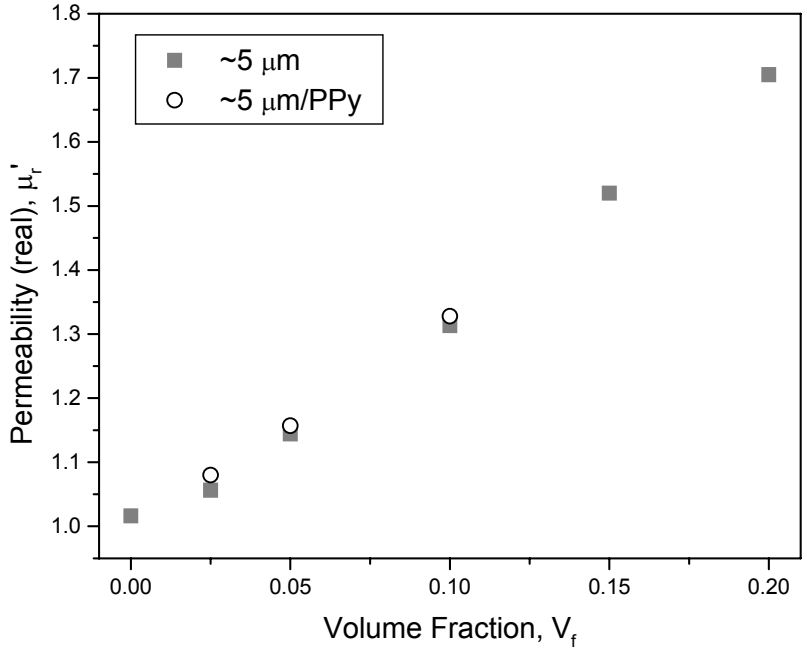

Figure 5-13. Average permeability (real) of Fe_3O_4 and PPy-coated Fe_3O_4 composites from 100 MHz to 200 MHz.

Data in Section 5.5.2 indicated that the surface conductivity of Fe_3O_4 was increased by two orders of magnitude with the polypyrrole coating. A significant increase in electrical conductivity of composites requires that enough fillers are present to establish a network of conductive paths. In other words, the concentration of fillers must be sufficient that the fillers are in contact with one another. For spherical fillers, the critical volume fraction for the conductive paths to be established is 0.33 [23]. In the case of the ~5 μm particles studied here, they are irregular in shape and possess an aspect ratio greater than 1. This is clearly shown in Figure 5-3. The critical volume fraction would be less than 0.33. Nevertheless, the composites fabricated here were still below the percolation threshold. Therefore, the effect the polypyrrole coating on electrical conductivity of composites was minimal.

Table 5-5 summarized the conductivity data of composites. The conductivities of the composites were too low to be measured using the four-point probe with the exception of one, Sample C21 (V_f = 0.10 using polypyrrole-coated particles). The measured bulk conductivity of Sample C21 was 9.37×10^{-7} S/cm, which was higher than Sample C18. Although Sample C21 did not have high conductivity, it demonstrated that polypyrrole coating on Fe_3O_4 particles added electrical conductivity to the final composite. Polypyrrole coating not only has the capability to improve conductivity, it also enhanced the mechanical properties, as discussed in the previous section.

Table 5-5. Bulk conductivity of Fe_3O_4 and PPy-coated Fe_3O_4 composites.

Sample ID	Particle Size and Treatment	V_f	Bulk Conductivity
C1	--	0	$< 1 \times 10^{-9}$
C14	5μm	0.025	$< 1 \times 10^{-9}$
C15		0.050	$< 1 \times 10^{-9}$
C16		0.100	$< 1 \times 10^{-9}$
C17		0.150	$< 1 \times 10^{-9}$
C18		0.200	$< 1 \times 10^{-9}$
C19	5μm/PPy	0.025	$< 1 \times 10^{-9}$
C20		0.050	$< 1 \times 10^{-9}$
C21		0.100	9.37×10^{-7}

5.6 Summary

We demonstrated that polypyrrole coating on Fe_3O_4 particles have the potential to add electrical conductivity to composites thereby producing a multifunctional material that has magnetic, electrical, and mechanical properties. First, a process was developed to coat 5 μm Fe_3O_4 particles with polypyrrole. The process was adapted from coating quartz and polyester fabrics with conductive polymer. A concentration of pyrrole was determined that produced polypyrrole coating between 5 to 10 weight % of the particles. Subsequently, the effects of dopant, oxidizing agent, temperature, and reaction time on conductivity of the coated particles were evaluated. Lowering the temperature from 25°C to 10-15°C doubled the conductivity. By coating the surface of Fe_3O_4 particles with polypyrrole, their surface conductivity was improved from 3.86×10^{-2} S/cm to 2.12 S/cm.

The mechanical and electromagnetic properties of composites with polypyrrole-coated magnetite particles were compared with those of composites containing bare Fe_3O_4 particles. The polypyrrole coating improved the flexural modulus minimally, but flexural strengths were improved signficantly. In composites with polypyrrole coating, the flexural strength recovered at a lower volume fraction and may be attributed to improved bonding between matrix and filler. The fracture properties of the two sets of composites followed similar trends, but the polypyrrole coating had an adverse effect. This can be explained by increased rigidity and strength since improving these properties usually come at the expense of fracture resistance and by the formation of clusters during the coating process.

The permeabilities and resonance frequencies of both sets of composites were very similar since magnetic properties were a contribution of Fe_3O_4 only. The polypyrrole coating on Fe_3O_4 particles improved the conductivity of the composite by at least two orders of magnitude. We expect that electrical conductivity of composites would be enhanced if filler loading were greater than the percolation threshold. This study showed how polypyrrole coating on magnetic fillers added electrical conductivity to the Fe_3O_4 composite system multifunctional without compromising the magnetic properties.

5.7 References

[1] H. Shirakawa, "The Discovery of Polyacetylene Film: The Dawning of an Era of Conducting Polymers (Nobel Lecture)," *Angewandte Chemie International Edition*, vol. 40, pp. 2574-2580, 2001.

[2] A. G. MacDiarmid, ""Synthetic Metals": A Novel Role for Organic Polymers," *Angewandte Chemie International Edition*, vol. 40, pp. 2581-2590, 2001.

[3] A. J. Heeger, "Semiconducting and Metallic Polymers: The Fourth Generation of Polymeric Materials (Nobel Lecture)," *Angewandte Chemie International Edition*, vol. 40, pp. 2591-2611, 2001.

[4] S. Maeda and S. P. Armes, "Polypyrrole-Tin(IV) Oxide Colloidal Nanocomposites," *Synthetic Metals*, vol. 69, pp. 499-500, 1995.

[5] X. Zhang and R. Bai, "Adsorption Behavior of Humic Acid onto Polypyrrole-Coated Nylong 6,6 Granules," *Journal of Materials Chemistry*, vol. 12, pp. 2733-2739, 2002.

[6] Q. L. Yang, J. Zhai, L. Feng, Y. L. Song, M. X. Wan, L. Jiang, W. G. Xu, and Q. S. Li, "Synthesis and Characterization of Conducting Polyaniline/γ-Fe_2O_3 Magnetic Nanocomposite," *Synthetic Metals*, vol. 135-136, pp. 819-820, 2003.

[7] A. Malinauskas, "Chemical Deposition of Conducting Polymers," *Polymer*, vol. 42, pp. 3957-3972, 2001.

[8] H. H. Kuhn, "Anthraquinone-2-Sulfonic Acid Doped Conductive Textiles." U.S.: Milliken Research Corporation, 1992.

[9] H. H. Kuhn, A. D. Child, and W. C. Kimbrell, "Toward Real Applications of Conductive Polymers," *Synthetic Metals*, vol. 71, pp. 2139-2142, 1995.

[10] H. H. Kuhn and W. C. Kimbrell, "Method for Making Electrically Conductive Textile Materials." U.S.: Milliken Research Corporation, 1991.

[11] H. H. Kuhn, W. C. Kimbrell, J. E. Fowler, and C. N. Barry, "Properties and Applications of Conductive Textiles," *Synthetic Metals*, vol. 55-57, pp. 3707-3712, 1993.

[12] R. V. Gregory, W. C. Kimbrell, and H. H. Kuhn, "Conductive Textiles," *Synthetic Metals*, vol. 28, pp. C823-C835, 1989.

[13] F. Ciardelli and G. Ruggeri, "Synthesis of Electroconducting Polymers," in *Structure and Transport Properties in Oganized Polymeric Materials*, E. Chiellini, M. Giordano, and D. Leporini, Eds. Singapore: World Scientific, 1997.

[14] L. Hao, C. Zhu, C. Chen, P. Kang, Y. Hu, W. Fan, and Z. Chen, "Fabrication of Silica Core-Conductive Polymer Polypyrrole Shell Composite Particles and Polypyrrole Capsule On Monodispersed Silica Templates," *Synthetic Metals*, vol. 139, pp. 391-396, 2003.

[15] S. F. Lascelles and S. P. Armes, "Synthesis and Characterization of Micrometre-Sized, Polypyrrole-Coated Polystyrene Latexes," *Journal of Materials Chemistry*, vol. 7, pp. 1339-1347, 1997.

[16] C.-L. Huang and E. Matijevic, "Coating of Uniform Inorganic Particles with Polymers: III. Polypyrrole on Different Metal Oxides," *Journal of Materials Research*, vol. 10, pp. 1327-1336, 1995.

[17] K. Liu, L. Zhao, P. Klavins, F. E. Osterloh, and H. Hiramatsu, "Extrinsic Magnetoresistance in Magnetite Nanoparticles," *Journal of Applied Physics*, vol. 93, pp. 7951-7953, 2003.

[18] W. B. Genetti, W. L. Yuan, B. P. Grady, E. A. O'Rear, C. L. Lai, and D. T. Glatzhofer, "Polymer Matrix Composites: Conductivity Enhancement through Polypyrrole Coating of Nickel Flake," *Journal of Materials Science*, vol. 33, pp. 3085-3093, 1998.

[19] J. Deng, Y. Peng, C. He, X. Long, P. Li, and A. S. Chan, "Magnetic and Conducting Fe_3O_4-Polypyrrole Nanoparticles with Core-Shell Structure," *Polymer International*, vol. 52, pp. 1182-1187, 2003.

[20] S. Liong, W. S. Rees Jr., and R. L. Moore, "Unpublished results," Georgia Institute of Technology, Monthly report 2004.

[21] E. P. Plueddemann, *Silane Coupling Agents*, Second ed. New York: Plenum Press, 1991.

[22] G. V. Jackson and M. L. Orton, "Filled Thermosets," in *Particulate-Filled Polymer Composites*, R. N. Rothon, Ed. Essex: Longman Scientific and Technical, 1995, pp. 317-370.

[23] R. L. McCullough, "Generalized Combining Rules for Predicting Transport Properties of Composite Materials," *Composites Science and Technology*, vol. 22, pp. 3-21, 1985.

CHAPTER 6

CONCLUSIONS AND FUTURE WORK

The main goal of this project was to develop lightweight multifunctional composite materials with magnetic, electrical, and mechanical properties. In this material, the mechanical (structural) properties were evaluated along side their electromagnetic properties.

Particulate polymer composite was used as the basis for the multifunctional composite system, and two composite systems were studied. In the first composite system, magnetite (Fe_3O_4) nanoparticles (average diameters 7 nm, 12 nm, and 25 nm) were used as fillers. In the second composite system, 5 μm Fe_3O_4 fillers were coated with polypyrrole to add electrical conductivity to the system. This approach allowed for both magnetic and conductive properties to be increased concurrently. Mechanical and electromagnetic properties of the two composite systems were characterized and evaluated as functions of particle size and filler content.

Magnetite nanoparticles with diameters less than 20 nm were neither available at a practical cost nor in large quantities. Therefore, to meet the demands of composite fabrication, part of this project was devoted to the synthesis and characterization of Fe_3O_4 nanoparticles. Using chemical coprecipitation, nanoparticles with average diameters of 5 nm to 12 nm were successfully synthesized. Size of synthesized particles can be modified by several process parameters, but the variables that showed the greatest influence were concentration of iron precursors, ratio of ferric to ferrous ions,

and ionic strength of solution. The process to synthesize 7 nm and 12 nm particles were established and these particles were used as fillers in nanocomposites.

The saturation magnetization and coercivities of the nanoparticles were measured at room temperature. The magnetic properties were a function of particle size, and both saturation magnetization and coercivities decreased with particle size. As reported by other groups, magnetite nanoparticles of this size range are superparamagnetic and exhibit reduction in saturation magnetization. It is widely accepted that surface effects, e.g. magnetically dead layer due to spin canting, surface defects, and surface anisotropy, cause the reduction in magnetization of nanoparticles. Using a weighted average, the thickness of this layer was calculated by fitting the magnetization data to particle size using a power law relationship. The thickness of this layer was calculated to be 0.93 nm – very close to the lattice constant of magnetite (0.84 nm). Other groups used an approximated form of the power law relationship and reported lower values (0.4 – 0.6 nm) for the thickness. Direct method of measuring the magnetically dead layer is the necessary next step to improve understanding of magnetic nanoparticles' behavior and the influence of surface effects.

Nanocomposites were fabricated and the goal was to produce samples with well-dispersed fillers. Fe_3O_4 nanoparticles were stabilized by modifying their surfaces with a surfactant, sodium dodecylbenzene sulfonate (NaDBS). The surfaces of 7 nm, 12 nm, and 25 nm particles were treated with surfactant and cross sections of the composites showed that dispersion of particles was improved with the treatment . 25 nm composites were fabricated with filler loading of V_f = 0.0125 to 0.10. The electromagnetic and

mechanical properties of nanocomposites were compared with the properties of micron-sized composites.

Permeability measurements were consistent with decreased magnetization in nanoparticles, since they were lower than permeabilities of micron-sized composites at the same volume fraction. Mechanical properties of the 25 nm composites showed similar behavior to micron-sized composites. Modulus increase with filler loading was almost identical in both sets. The presence of 7 nm and 12 nm particles in epoxy resin affected their curing behavior, i.e. composites with those fillers required longer curing times. The reason for this is unclear, but it is related to increased interfacial area between particle and matrix and the adsorbed surfactant on the surface of particles. It was observed that the effect on curing was more significant in smaller particles and/or at higher filler volume fraction. Clearly more work can be done to elucidate the influence of surfactant-treated nanoparticles on curing kinetics of epoxy resin. The plasticizing effect of adsorbed surfactants on the polymer matrix should be considered in future studies.

The process for particle dispersion in polymer matrix can still be applied in other types of polymer. In fact, the use of a thermoplastic polymer should be considered as a matrix. Curing reaction is omitted altogether in thermoplastics and different results could be obtained.

Fracture data showed that 7 nm and 12 nm nanoparticles could significantly improve the crack resistance of the matrix at low filler loading. A reinforcing effect at low filler loading is important in the development of lightweight materials. However, the improvements in fracture properties were obtained at the expense of decreased

modulus and strength. Fabric-reinforcements could be utilized in conjunction with nanoparticles to compensate for the aforementioned trade-offs. With this hierarchical composite approach, nanoparticles may still be used as fillers and their shortcomings are addressed with a well-established reinforcing method. In the end, a composite system with improved modulus, strength, and fracture properties could be developed.

In the second composite system, a process for polypyrrole coating on micron-sized Fe_3O_4 particles was developed. The surface conductivity of the particles improved by two orders of magnitude with the presence of the coating. Strengths of composites with polypyrrole-coated magnetite fillers were improved over the bare fillers. Moduli of the two sets of composites were similar. The highest filler loading was $V_f = 0.10$ for composites polypyrrole-coated magnetite fillers, but there was early evidence that they could offer improvement in electrical conductivity of composites – by two orders of magnitude. This composite system has great potential, especially if samples with higher filler loading were fabricated. This work demonstrated that conductive and magnetic properties could be enhanced concurrently. Further work should include the fabrication of samples with higher filler loading. Improvement in coating process should also be considered, such as using other dopants to increase conductivity. Polyaniline can also be an alternative to polypyrrole and should be evaluated as a candidate for coating on Fe_3O_4 fillers. The coating process is quite versatile, so it would be an easy transition to try other types of inorganic fillers as candidates for substrates.

A unique approach for multifunctional composites was developed using Fe_3O_4 nanoparticles and polypyrrole-coated Fe_3O_4 particles as fillers. Fe_3O_4 particles are a good candidate for filler in a multifunctional composite system because they can

reinforce mechanical properties of a polymer matrix and impart magnetic properties into a composite. Polypyrrole coating on Fe_3O_4 particles was utilized to incorporate electrical conductivity to the properties of composites. The effects of filler size and filler content were studied on both the mechanical and electromagnetic properties. Fe_3O_4 nanoparticles were a major part of this work – from their synthesis to their application in composites. The surface effect on magnetic properties was analyzed for Fe_3O_4 nanoparticles, resulting in a more accurate calculation of the magnetically dead layer thickness than previously reported. The results from this work contributed to further understanding of synthesis and characterization of magnetic nanoparticles, fabrication and characterization of nanocomposites, and design and development of lightweight multifunctional materials. Although the properties of the fabricated composites require further improvement, the methodology and approach provide a basis for future work in lightweight multifunctional composites.